Journal of Mechanics of Materials and Structures

Volume 7, No. 6 June 2012

mathematical sciences publishers

JOURNAL OF MECHANICS OF MATERIALS AND STRUCTURES

jomms.net

Founded by Charles R. Steele and Marie-Louise Steele

See http://jomms.net for submission guidelines.

JoMMS (ISSN 1559-3959) is published in 10 issues a year. The subscription price for 2012 is US $555/year for the electronic version, and $735/year (+$60 shipping outside the US) for print and electronic. Subscriptions, requests for back issues, and changes of address should be sent to Mathematical Sciences Publishers, Department of Mathematics, University of California, Berkeley, CA 94720–3840.

JoMMS peer-review and production is managed by EditFLOW® from Mathematical Sciences Publishers.

PUBLISHED BY

mathematical sciences publishers

http://msp.org/

A NON-PROFIT CORPORATION

Typeset in LaTeX

JOURNAL OF MECHANICS OF MATERIALS AND STRUCTURES
Vol. 7, No. 6, 2012
dx.doi.org/10.2140/jomms.2012.7.509

msp

THE IMPLICIT COROTATIONAL METHOD AND ITS USE IN THE DERIVATION OF NONLINEAR STRUCTURAL MODELS FOR BEAMS AND PLATES

GIOVANNI GARCEA, ANTONIO MADEO AND RAFFAELE CASCIARO

What we call the *implicit corotational method* is proposed as a tool to obtain geometrically exact nonlinear models for structural elements, such as beams or shells, undergoing finite rotations and small strains, starting from the basic solutions for the three-dimensional Cauchy continuum used in the corresponding linear modelings.

The idea is to use a local corotational description to decompose the deformation gradient in a stretch part followed by a finite rigid rotation. Referring to this corotational frame we can derive, from the linear stress tensor and the deformation gradient provided by linear elasticity, an accurate approximation for the nonlinear stress and strain tensors which implicitly assure frame invariance. The stress and strain fields recovered in this way as functions of generalized stress and strain resultants are then used within a mixed variational formulation allowing us to recover an objective nonlinear modeling directly suitable for FEM implementations through a black-box process which maintains the full details of the linear solutions, such as shear warping and other subtle effects.

The method is applied to the construction of three-dimensional beam and plate nonlinear models starting from the Saint-Venant rod and Kirchhoff and Mindlin–Reissner plate linear theories, respectively.

1. Introduction

Nonlinear analysis of slender elastic structures requires sound nonlinear modeling to achieve reliable and accurate solutions. The use of a frame-invariant (or objective) structural model, where stress and strain fields are unaffected by finite rigid motions of the body, is a necessary requirement for the analysis [Malvern 1969; Ibrahimbegovic and Taylor 2002]. While it is quite easy to satisfy frame-invariance for three-dimensional bodies using the Cauchy continuum, it can be difficult to obtain a coherent, simple enough modeling for slender structural elements, such as beams or shells, which are more conveniently described as one or two-dimensional fibred continua characterized by three-dimensional displacements and rotations.

In the last few years great efforts have been made to develop nonlinear models of beams, plates, and shells and their finite element implementations. The number of papers on this topic is formidable and this is due, in the authors' opinion, to the complexity of the nonlinear modeling process and to the sometimes unsatisfactory results obtained by FEM discretizations.

This paper has been developed within the national joint research project "Performance-based modeling and analysis of nonlinear structures," supported by the Italian Ministry of University Scientific and Technology Research (MIUR). We would like to thank all the participants in the project for their comments and suggestions.
Keywords: geometrically exact beam and shell theories, corotational description, postbuckling analysis.

The great majority of beam and shell models are based on *geometric exact theories* such as those developed in [Cosserat and Cosserat 1909; Reissner 1972; Simo 1986; Wriggers and Gruttmann 1993; Antman 1995; Auricchio et al. 2008]. Models so generated are geometrically exact, that is, exactly frame-independent, but, being based on simplified assumptions in the constitutive laws relating strain and stress resultants, are generally unable to describe important details already present in the corresponding linear models. This is evident, for example, in the classical Antman–Simo nonlinear beam model where the assumed simplified constitutive law lacks the shear/torsional coupling manifested by the three-dimensional Saint-Venant linear solution [de Saint-Venant 1855] and more subtle nonlinear couplings associated with the section warping, such as the axial-torsional second-order coupling recognized in [Wagner 1936].

Models derived as Ritz–Galerkin approximations by introducing a three-dimensional displacement field in a variational principle allow for more detailed modeling, at least in principle. This approach was followed, for instance, in [Pai and Nayfeh 1994; Pai et al. 1998; Petrov and Géradin 1998a; 1998b; Nayfeh and Pai 2004; Pi et al. 2005; Kim et al. 2005; Chen et al. 2006]. However, extending to finite kinematics the three-dimensional displacement provided by the linear theory, like the nonlinear beam model of [Petrov and Géradin 1998a; 1998b], appears somewhat overcomplex and also requires ad hoc simplifications in order to eliminate spurious locking. Models obtained by the use of problem-dependent engineering nonlinear strain measures, like the beam and shell models of Nayfeh and Pai (see [Nayfeh and Pai 2004]), are only aimed at an essential simplified modeling.

On the other hand the availability of linear structural models for fibred continua derived, using a small displacements hypothesis, from three-dimensional Cauchy equations through appropriate assumptions on the statics and kinematics of the body is notable. Its use, as a basis to generate a corresponding nonlinear model, is then attractive due to the possibility of recovering all the effort spent in developing linear theories in a simplified context. The aim of this paper is to exploit this possibility through the use, in the continuum description, of the corotational approach initially proposed in a FEM context in [Wemper 1969; Belytschko and Glaum 1979; Rankin 1986; Nour-Omid and Rankin 1991] and used to construct a nonlinear finite element starting from a linear one.

In this paper we show that, by transferring this idea from the element to the continuum, we can derive a standard methodology to obtain a frame-indifferent nonlinear modeling which maintains all the details of the embedded linear solution. We call the proposed method the *implicit corotational method* (ICM).

The main idea is to associate a corotational frame (observer) to each point of the three-dimensional continuum so allowing the motion in the neighbor of the point to be split in a pure stretch followed by a pure rotation, according to the decomposition theorem [Malvern 1969; Bonet and Wood 1997]. It will be shown that, using the small strain hypothesis and rotation algebra, the linear stress and linear strain solution fields, when viewed in this corotational frame, can provide accurate approximations for the Biot nonlinear stress and strain tensor fields. Once the corotational rotation is appropriately defined, the local statics and kinematics of the model are recovered from the linear solution as a function of the stress/displacement resultants. Stress and strain fields are then introduced within a mixed variational principle in order to obtain the constitutive laws directly in terms of stress/strain resultants. This completes the ICM definition of the nonlinear model.

The thus-obtained nonlinear model retains all the details of the three-dimensional linear solution, including torsion/shear warping, while its objectivity is ensured implicitly. Furthermore, the use of the mixed formulation and the greater accuracy with which ICM recovers the stress field allow an accurate

description of the constitutive laws in terms of resultants. The proposed approach does not require any ad hoc assumptions about the structural model at hand, nor does it depend on any particular parametrization of the rotation tensor, but rather it actually behaves as a black-box tool able to translate known linear models into the corresponding nonlinear ones. Moreover, the direct use of a mixed (stress/strain) description provides an automatic and implicitly coherent methodology for generating models free of nonlinear locking effects [Garcea et al. 1998; 1999; 2002; 2005] in a format directly suitable for use in FEM implementations.

To better illustrate the features of ICM and to show its potential, the method will be implemented here in order to obtain a nonlinear three-dimensional beam model, derived from the general Saint-Venant linear rod theory, and two nonlinear plate models, derived from the Kirchhoff and Mindlin plate theories. We will also show that from these new structural models, through simplifying assumptions, models already available in the literature can be derived.

The paper is organized as follows: Section 2 introduces the variational framing used in our proposal. Section 3 gives a general overview of ICM and provides the main algebra which is involved in the proposed method. Section 4 presents and discusses some tutorial implementations to underline its main features and to show its effectiveness and reliability in recovering known noteworthy results from the literature. Sections 5 and 6 develop a nonlinear three-dimensional beam model and two nonlinear plate models, and also compare these with similar proposals available in the literature. Section 7 contains some comments and further insights. A summary of the results obtained and possible extensions are given in the concluding section.

The FEM implementation of the ICM models presented here, together with the derivation of nonlinear beam and plate finite elements and their validation through numerical testing, will be discussed in detail in our subsequent, related paper [Garcea et al. 2012].

2. Nonlinear analysis

Nonlinear analysis usually refers to a structure subjected to an assigned loading path $p[\lambda]$, λ being a load parameter controlling the loading process. The structural behavior is governed by the stationarity condition of its total potential energy $\Pi[u, \lambda]$, associated with the external load p and with the configuration u of the structure, with respect to all admissible changes in configuration δu. Using compact notation this condition is expressed by

$$\Pi'[u, \lambda]\delta u = 0, \quad u \in \mathcal{U}, \quad \delta u \in \mathcal{T}, \tag{1}$$

where $\mathcal{U}$ is the manifold of the admissible configurations, $\mathcal{T}$ its tangent space, and the prime stands for Frechèt differentiation with respect to u. Usually (and conveniently) the configuration is described making $\mathcal{U}$ a linear manifold, so $\mathcal{T}$ becomes independent from u. This choice, always possible with an opportune definition of the configuration variables, noticeably simplifies the variations algebra and also is well suited for FEM implementation, where it simplifies the interelement continuity conditions (see [Casciaro 2005]). Condition (1) states a relationship between λ and u describing a curve in $\{u, \lambda\}$ space. The goal of the analysis is to determine this curve, the *equilibrium path*, with particular accuracy in the evaluation of the maximum value λ_c of the load multiplier.

The potential energy can be split into two separate terms, the first expressing the internal strain energy and the second the external load work, that, for the sake of simplicity and without loss of generality, can be assumed as linear in u, as usual in FEM formulation:

$$\Pi[u, \lambda] := \Phi[u] - p[\lambda]u. \tag{2}$$

We also know (see [Garcea et al. 1998; 1999; 2002; 2005]) that, with an appropriate choice of configuration variables $u := \{\sigma, d\}$ and the corresponding choice $p := \{\bar{\varepsilon}, q\}$, these terms could be written in mixed form as

$$\Phi[u] := -\Psi[\sigma] + \sigma\varepsilon[d], \qquad p[\lambda]u := q[\lambda]d + \bar{\varepsilon}[\lambda]\sigma, \tag{3}$$

σ and d being the stress and displacement fields, q and $\bar{\varepsilon}$ the external forces and distortions, $\varepsilon[d]$ the compatible strain field associated with d through kinematics, and $\Psi[\sigma]$ the *complementary strain energy* which is usually assumed as quadratic in σ:

$$\Psi[\sigma] := \tfrac{1}{2} C\sigma^2, \tag{4}$$

with C being the positive definite bilinear compliance operator. The $\varepsilon[d]$ function plays an important role in the analysis. Assuming the $\varepsilon[d]$ relationship is linear, we obtain a linear formulation. So we can translate from a linear to a geometrically nonlinear formulation simply by referring to a proper nonlinear expression for the geometrical relation $\varepsilon[d]$, which also implicitly defines the stress σ as work-associated with ε.

The invariance from superposed rigid body motions, that is, objectivity, is an essential prerequisite for the function $\varepsilon[d]$. This requirement is easily satisfied if referring to a three-dimensional Cauchy body, simply by taking d as the displacement field and ε as the Green–Lagrange strain tensor field (by this choice, σ will be the second Piola–Kirchhoff stress tensor field).

In many cases of practical relevance, such as for beams and plates, the three-dimensional behavior can be conveniently described using generalized quantities defined over a one-dimensional (the beam axis) or two-dimensional (the median plane of the plate) domain. In this way, the three-dimensional continuum is converted to a coherently derived one or two-dimensional model, which can more easily be treated. This modeling approach is really convenient and extensively used in linear analysis, but its extension to nonlinear analysis is not so obvious.

Equations (1)–(4) offer a convenient variational framing for the setup of a nonlinear model that only requires as ingredients suitable separate choices for the displacement and stress fields u and σ. When using a material description, stresses are unaffected by a change in observer, so the use of a separate evaluation is extremely convenient in nonlinear modeling. Furthermore we will show that, as usual, we have a better estimate of the stress than that of the displacements.

3. The implicit corotational method

The goal of the implicit corotational method (ICM) is to fully reuse, in a nonlinear context, the results of linear theories in order to obtain objective structural models in a format suitable for FEM implementations. It is shown that, at least in the presence of smooth small strains, an appropriate representation of the strains and stresses (making use of the Biot tensors) together with an appropriate choice of the local frame (through a corotational formulation) is the key to exploiting the linear solution in a nonlinear

setting. This can be achieved by standard methodology, without the need for ad hoc assumptions related to the particular problem at hand, as in [Nayfeh and Pai 2004].

3.1. ***Kinematics preliminaries.*** Material points $\boldsymbol{X} \in \mathbb{E}^3$ of the reference configuration occupy position $\boldsymbol{x}$ in the current configuration. Rigid-body motions (see [Malvern 1969]) can be described in terms of *translations* and *rotations*. We denote by the vector $\boldsymbol{v}$ the translations and by $\boldsymbol{R}$ the rotations, where $\boldsymbol{R}$ belongs to the space of proper-orthogonal tensors, $\boldsymbol{R} \in SO(3)$. A rigid-body motion characterized by a translation $\boldsymbol{v}$ and rotation $\boldsymbol{R}$ can also be viewed as a change of observer which suffers the inverse rotation $\boldsymbol{Q} = \boldsymbol{R}^T$ and the opposite translation $\boldsymbol{c} = -\boldsymbol{v}$ (T indicates the transpose).

If the positions viewed by the original observer and by the moved observer are denoted by $\bar{\boldsymbol{x}}$ and $\boldsymbol{x}$, respectively, the relationships between them are

$$\bar{\boldsymbol{x}} = \boldsymbol{Q}^T(\boldsymbol{x} - \boldsymbol{c}), \quad \boldsymbol{x} = \boldsymbol{Q}\bar{\boldsymbol{x}} + \boldsymbol{c}.$$

The displacements viewed by the two observers are denoted by $\bar{\boldsymbol{u}}$ and $\boldsymbol{u}$, respectively, and will be related by

$$\bar{\boldsymbol{u}} = \boldsymbol{Q}^T(\boldsymbol{X} + \boldsymbol{u} - \boldsymbol{c}) - \boldsymbol{X}, \tag{5a}$$

while the rotations are related by

$$\bar{\boldsymbol{R}} = \boldsymbol{Q}^T\boldsymbol{R}. \tag{5b}$$

By assuming a fixed reference frame with origin O and basis vectors $\{\boldsymbol{e}_1, \boldsymbol{e}_2, \boldsymbol{e}_3\}$ in $\mathbb{E}^3$, both translations and rotations can be defined in terms of three scalar parameters. While the translations are described conveniently by their (covariant) components, the rotations are expressed by the exponential mapping according to

$$\boldsymbol{R} := \boldsymbol{I} + \boldsymbol{\omega}[\boldsymbol{w}], \quad \boldsymbol{\omega}[\boldsymbol{w}] := \sum_{n=1}^{\infty} \frac{1}{n!}\boldsymbol{W}^n, \tag{5c}$$

where $\boldsymbol{W}$ is the following skew-symmetric matrix, whose associated axial vector is $\boldsymbol{w} = w_i\boldsymbol{e}_i$:

$$\boldsymbol{W} := \begin{bmatrix} \cdot & -w_3 & w_2 \\ w_3 & \cdot & -w_1 \\ -w_2 & w_1 & \cdot \end{bmatrix}. \tag{6}$$

3.2. ***Kinematics of a three-dimensional Cauchy body.*** Consider a Cauchy body (see [Malvern 1969]) referred to the fixed Cartesian frame $(O, \{\boldsymbol{e}_1, \boldsymbol{e}_2, \boldsymbol{e}_3\})$ and let the reference configuration be stress-free. The deformation gradient is $\boldsymbol{F} = \boldsymbol{I} + \nabla\boldsymbol{u}$ where $\boldsymbol{I}$ is the identity tensor and $\nabla(\,\cdot\,) := \partial(\,\cdot\,)/\partial\boldsymbol{X}$ is the material gradient.

By the polar decomposition theorem (see [Malvern 1969])

$$\boldsymbol{F} = \boldsymbol{R}\boldsymbol{U}, \tag{7}$$

where $\boldsymbol{R}[\boldsymbol{X}]$ is the rotation tensor and $\boldsymbol{U}[\boldsymbol{X}]$ is the (symmetric, positive-definite) stretching tensor.

Recalling (5b), the rotation can be reduced to the identity ($\bar{\boldsymbol{R}} = \boldsymbol{Q}^T\boldsymbol{R} = \boldsymbol{I}$) simply by a change in the observer, making $\boldsymbol{Q} = \boldsymbol{R}$. An objective description requires that the strain measure be independent from $\boldsymbol{R}$. This requirement is not satisfied, in general, by the so-called infinitesimal strain tensor, denoted

by $\boldsymbol{\varepsilon}_L$, which is obtained by expressing the deformation gradient $\nabla \boldsymbol{u}$ in its symmetric and skew-symmetric parts

$$\boldsymbol{\varepsilon}_L := \boldsymbol{E} = \tfrac{1}{2}(\nabla \boldsymbol{u} + \nabla \boldsymbol{u}^T), \quad \boldsymbol{W} := \tfrac{1}{2}(\nabla \boldsymbol{u} - \nabla \boldsymbol{u}^T). \tag{8}$$

Possible objective strain measures are expressed in the form $\boldsymbol{\varepsilon}^{(n)} := (1/n)(\boldsymbol{U}^n - \mathbf{I})$ which, for $n = 1$ and $n = 2$ respectively, provides the *Biot strain tensor* $\boldsymbol{\varepsilon}_b$ and the *Green–Lagrange strain tensor* $\boldsymbol{\varepsilon}_g$:

$$\boldsymbol{\varepsilon}_b := \boldsymbol{R}^T \boldsymbol{F} - \boldsymbol{I}, \quad \boldsymbol{\varepsilon}_g := \tfrac{1}{2}(\boldsymbol{F}^T \boldsymbol{F} - \boldsymbol{I}). \tag{9}$$

The latter can be easily evaluated from $\nabla \boldsymbol{u}$ through a simple quadratic expression:

$$\boldsymbol{\varepsilon}_g = \boldsymbol{E} + \tfrac{1}{2} \nabla \boldsymbol{u}^T \nabla \boldsymbol{u}. \tag{10}$$

However, its identification in terms of linear strain, that is, $\boldsymbol{\varepsilon}_g \approx \boldsymbol{\varepsilon}_L$, requires $\|\nabla \boldsymbol{u}\| \ll 1$ which implies too restrictive hypotheses about the expected solutions to be used in practice.

The Biot strain $\boldsymbol{\varepsilon}_b$ seems to be a better candidate for that purpose. In fact, expressing $\boldsymbol{R}$ in the form (5c) we obtain the relation

$$\boldsymbol{\varepsilon}_b = \boldsymbol{E} + \tfrac{1}{2}(\boldsymbol{\omega}^T \nabla \boldsymbol{u} + \nabla \boldsymbol{u}^T \boldsymbol{\omega} - \boldsymbol{\omega}^T \boldsymbol{\omega}), \tag{11}$$

which implies that $\boldsymbol{\varepsilon}_b \approx \boldsymbol{\varepsilon}_L$ when $\boldsymbol{\omega} \approx \mathbf{0}$, obtained by an appropriate change of local observer. If we assume that $\boldsymbol{\varepsilon}_b$ and $\boldsymbol{\omega}$ are small enough (so that $\boldsymbol{\omega} \sim \boldsymbol{W}$), $\boldsymbol{\varepsilon}_b$ can be expressed by its second-order approximation

$$\boldsymbol{\varepsilon}_b \approx \tilde{\boldsymbol{\varepsilon}}_b := \boldsymbol{E} + \tfrac{1}{2}(\boldsymbol{E}\boldsymbol{W} - \boldsymbol{W}\boldsymbol{E} - \boldsymbol{W}^2). \tag{12}$$

Note that by (9), it is

$$\boldsymbol{\varepsilon}_b = \boldsymbol{\varepsilon}_g - \tfrac{1}{2}\boldsymbol{\varepsilon}_b^2 = \tilde{\boldsymbol{\varepsilon}}_b - \tfrac{1}{2}(\boldsymbol{\varepsilon}_b^2 - \boldsymbol{E}^2),$$

so the resulting error in using (12) can be evaluated as $(\boldsymbol{\varepsilon}_b^2 - \boldsymbol{E}^2)/2 \approx \mathbb{O}[\|\boldsymbol{\varepsilon}_b^2 \boldsymbol{\omega}\| + \|\boldsymbol{\varepsilon}_b \boldsymbol{\omega}^2\| + \|\boldsymbol{\omega}^4\|]$.

In our treatment, we deal with problems characterized by large displacements but small strains, so that we can assume $\|\boldsymbol{\varepsilon}_b\| \ll 1$. The key of our approach is to use a suitable change of observer so as to make at the same time the *rotation residual* as small as possible ($\boldsymbol{\omega} \approx \mathbf{0}$). That is, we set up the formulation so as to make $\boldsymbol{\omega}$ small enough to allow $\boldsymbol{\varepsilon}_b$ to be evaluated through (12).

From now on $\boldsymbol{R}$ will always denote the polar decomposition rotation in (7) and $\boldsymbol{Q}$ the change of observer rotation in (5a).

3.3. ***Constitutive equation for a three-dimensional Cauchy body.*** Stress and strain are work conjugated, thus the selection of a strain measure among $\boldsymbol{\varepsilon}_L$, $\boldsymbol{\varepsilon}_g$, and $\boldsymbol{\varepsilon}_b$ implies the choice of the work-conjugate stress tensor, that is, $\boldsymbol{\sigma}_L$, $\boldsymbol{\sigma}_g$, and $\boldsymbol{\sigma}_b$. Here $\boldsymbol{\sigma}_L$ is the linear stress tensor, $\boldsymbol{\sigma}_g$ is the *second Piola–Kirchhoff stress tensor*, and the *Biot stress tensor* $\boldsymbol{\sigma}_b$ is defined by $\boldsymbol{\sigma}_b := \frac{1}{2}(\boldsymbol{U}\boldsymbol{\sigma}_g + \boldsymbol{\sigma}_g \boldsymbol{U})$.

As discussed above, by referring to an appropriate corotational frame such that $\boldsymbol{\omega} \approx \mathbf{0}$, we can recover $\boldsymbol{\varepsilon}_b$ using (12) from the displacement gradient $\nabla \boldsymbol{u}$ with great accuracy. To complete the recovery we also need to relate the nonlinear stress and strain tensors, namely $\boldsymbol{\sigma}_b$ and $\boldsymbol{\varepsilon}_b$, through constitutive equations.

Within the mixed formulation followed in Section 2, constitutive equations are obtained by zeroing the variation with respect to the stress field of the mixed form (3) of the strain energy. Denoting by $\boldsymbol{\sigma}$ and $\boldsymbol{\varepsilon}$ any work conjugate strain and stress tensors, we can rewrite (3) as

$$\Phi := \int_{\mathcal{B}} (\boldsymbol{\sigma} \cdot \boldsymbol{\varepsilon} - \psi[\boldsymbol{\sigma}])\, dV, \tag{13}$$

$\mathcal{B}$ being the reference body volume.

The linear solution is characterized by the complementary energy $\psi_L[\boldsymbol{\sigma}_L] := \frac{1}{2}\boldsymbol{\sigma}_L \cdot \boldsymbol{C}_L\boldsymbol{\sigma}_L$, $\boldsymbol{C}_L$ being the *elastic compliance* tensor. Taking the variation with respect to $\boldsymbol{\sigma}_L$, we have

$$\boldsymbol{\varepsilon}_L[\boldsymbol{\sigma}_L] := \boldsymbol{C}_L\boldsymbol{\sigma}_L. \tag{14}$$

So, assuming the same relationship between $\boldsymbol{\sigma}_b$ and $\boldsymbol{\varepsilon}_b$, that is,

$$\boldsymbol{\varepsilon}_b[\boldsymbol{\sigma}_b] := \boldsymbol{C}_b\boldsymbol{\sigma}_b, \quad \boldsymbol{C}_b \approx \boldsymbol{C}_L, \tag{15}$$

the identification $\boldsymbol{\sigma}_b \approx \boldsymbol{\sigma}_L$, with $\boldsymbol{\sigma}_L$ defined by (14) and $\boldsymbol{\varepsilon}_b$ by (12), will imply a local compatibility error

$$\boldsymbol{\varepsilon}_b - \boldsymbol{C}_b\boldsymbol{\sigma}_b \approx \tfrac{1}{2}(\boldsymbol{E}\boldsymbol{W} - \boldsymbol{W}\boldsymbol{E} - \boldsymbol{W}^2) = \mathbb{O}(\|\boldsymbol{\varepsilon}_b\boldsymbol{\omega}\| + \|\boldsymbol{\omega}^2\|), \tag{16}$$

which can be considered negligible for small $\boldsymbol{\omega}$.

This is a key result of our approach since it proves that the choice of the Biot tensors allows us to extend the constitutive laws of linear elasticity to the nonlinear range. On the contrary, if the Green–Lagrange strain tensor is adopted, the assumption

$$\boldsymbol{\varepsilon}_g[\boldsymbol{\sigma}_g] := \boldsymbol{C}_g\boldsymbol{\sigma}_g, \quad \boldsymbol{C}_g \approx \boldsymbol{C}_L,$$

implies

$$\boldsymbol{\varepsilon}_g - \boldsymbol{\varepsilon}_g[\boldsymbol{\sigma}_g] \approx \mathbb{O}(\|\boldsymbol{\varepsilon}_b^2\|),$$

even in the most favorable case of $\boldsymbol{\omega} \approx 0$, which can hardly be accepted.

3.4. ***Use of linear solutions to set up a nonlinear model.*** The previous considerations have shown that, when viewed by a local corotational observer rotating with the material neighborhood ($\boldsymbol{Q} \approx \boldsymbol{R}$), both the kinematic and constitutive equations of linear theory correspond to those of the nonlinear problem expressed in terms of the Biot (corotational) tensors, at least within our assumption of small strains.

We need to obtain sufficient information about the stress and strain fields in order to obtain an accurate Galerkin approximation of the nonlinear solution through the use of the variational formulation (1)–(4). So the possibility of relating the nonlinear solution, written in terms of corotational quantities, to the results of a linear theory is an important point in the setup of a general methodology for deriving nonlinear structural models from the available linear ones. This has great potential because the literature on linear theory is very vast and well consolidated and so the possibility of reusing linear results in a nonlinear context provides a real advantage.

Linear theory, during its long history, has yielded a rich variety of complex and elegant solutions for the Cauchy problem obtained with the assumption that displacements (rotations), besides their gradients, are small enough that the deformed configuration can be taken to coalesce into the undeformed configuration when enforcing balance laws. So their derivation implies the use of an appropriate frame (observer), suitable for filtering out rigid rotations in order to minimize this difference. Therefore, the corotational idea is in some way implicit in linear theories.

To better explain this concept, we consider, as an example, the Saint-Venant theory of elastic cylinders. The solution, expressed in terms of the stress field over the cross section domain and the out-of-plane warping of the section, is naturally referred to a local Cartesian system $\{x, y, z\}$, such that the x-axis

is orthogonal to the (average) section plane and the y and z-axes are aligned with its principal directions, that is, with an observer fixed to the cross section. Actually, besides the disturbance produced by the section warping, which is somewhat small being related only to the distortion of the longitudinal fibers due to torsion and shear, all quantities involved in the Saint-Venant solution can be identified as *corotational*.

The Saint-Venant stress solution $\boldsymbol{\sigma}_L$ can thus be quite naturally identified as a first-order approximation of the nonlinear solution in terms of Biot stresses $\boldsymbol{\sigma}_b[y, z]$. In the same way, the displacement solution $\nabla \boldsymbol{u}_L[y, z]$ can be identified as a first-order approximation of the corresponding nonlinear solution. The identification $\boldsymbol{\varepsilon}_b[y, z] \approx \boldsymbol{\varepsilon}_L[y, z]$ requires $\boldsymbol{\omega}[y, z] \approx \mathbf{0}$ to obtain full geometrical consistency. Actually, this condition cannot be satisfied exactly, because of the pointwise differences in rotation due to the section warping, but we can generally assume a small enough $\boldsymbol{\omega}$ to allow the Biot strains to be obtained from (12), by introducing the expressions for $\boldsymbol{E}$ and $\boldsymbol{W}$ directly provided by $\nabla \boldsymbol{u}_L[y, z]$.

The previous discussion can easily be generalized for the nonlinear modeling of fibred continua such as beams or shells, whose description is obtained by splitting the original three-dimensional material reference $\boldsymbol{X}$ into a two or one-dimensional abscissa z lying on a *fiber* (the cross section, in the case of beams, or the transverse fiber, in the case of shells) and a one or two-dimensional abscissa s lying on its *support* (the line axis or the middle surface, respectively), depending on the model considered. The linear modeling defines both stress and displacement fields in terms of the generalized stress $\boldsymbol{t}[s]$ and displacement (translation/rotation) $\boldsymbol{d}[s]$ parameters:

$$\boldsymbol{\sigma}_L[z, s] := \boldsymbol{\sigma}_L[z, \boldsymbol{t}], \quad \nabla \boldsymbol{u}_L[z, s] := \nabla \boldsymbol{u}_L[z, \boldsymbol{d}]. \tag{17}$$

The nonlinear model is then generated, by identifying the linear solution as the Biot stress field, taking $\boldsymbol{\sigma}_b[z, s] \approx \boldsymbol{\sigma}_L[z, \boldsymbol{t}]$, and by rewriting the second relation, through the use of an appropriate local corotational change from $\boldsymbol{d}[s]$ to $\bar{\boldsymbol{d}}[s]$ such that the Biot strains could also be recovered by introducing $\nabla \bar{\boldsymbol{u}}_L = \nabla \boldsymbol{u}_L[z, \bar{\boldsymbol{d}}]$ into (12). We can introduce these fields into the expression of the potential energy (2)–(4), so completing the modeling.

This process is described in greater detail in the following section. We only note here that, besides the use of the quadratic formula (12), all of the nonlinearity of the formulation reduces to the transformation rules relating the kinematic parameters $\boldsymbol{d}[s]$ and $\bar{\boldsymbol{d}}[s]$, which are governed by purely geometric laws (see Section 3.1). It is straightforward to treat the rotation $\boldsymbol{Q}[s]$ of the observer as a finite rotation, without introducing any further approximations. In this way we can obtain a nonlinear modeling which is able to both exploit the full details of the corresponding three-dimensional linear solution and to satisfy the objectivity requirements with respect to the rigid motion of the fiber exactly.

3.5. ***Basic elements of ICM.*** The basic elements and assumptions of ICM are summarized schematically here:

(1) *Setup of the corotational observer.* By assuming that a linear solution is known in advance, in the form (17), we define for each point of the support an appropriate change in the observer $\boldsymbol{Q}[s]$ suitable to make as small as possible the rotation residual $\boldsymbol{\omega}[z, s]$ on the corresponding fiber $\mathcal{S}[s]$. This change is governed by a relationship between the two sets of kinematical parameters $\boldsymbol{d}[s]$ and $\bar{\boldsymbol{d}}[s]$, as viewed by the fixed and corotational observers. Usually $\boldsymbol{d}[s]$ collects both displacement derivatives $\boldsymbol{u}_{,s}$ and rotation

derivatives $\boldsymbol{R}_{,s}$, and these are transformed according to

$$\bar{\boldsymbol{u}}_{,s} := \boldsymbol{Q}^T(\boldsymbol{X}_{,s} + \boldsymbol{u}_{,s}) - \boldsymbol{X}_{,s}, \qquad \bar{\boldsymbol{R}}_{,s} := \boldsymbol{Q}^T \boldsymbol{R}_{,s}. \tag{18a}$$

From now on we denote the derivative with a comma.

(2) *Recovering the stress and displacement fields by the linear solution.* When referring the linear solution to the corotational frame, we obtain an explicit expression for the linear tensors $\nabla\bar{\boldsymbol{u}}_L$ and $\boldsymbol{\sigma}_L$ in $\mathcal{S}[s]$:

$$\nabla\bar{\boldsymbol{u}}_L := \nabla\bar{\boldsymbol{u}}_L[\bar{\boldsymbol{d}}[s]], \qquad \boldsymbol{\sigma}_L := \boldsymbol{\sigma}_L[\boldsymbol{t}[s]]. \tag{18b}$$

The corotational (Biot) stress and strain tensors are then identified as

$$\boldsymbol{\sigma}_b := \boldsymbol{\sigma}_L, \qquad \boldsymbol{\varepsilon}_b := \boldsymbol{E} + \tfrac{1}{2}(\boldsymbol{E}\boldsymbol{W} - \boldsymbol{W}\boldsymbol{E} - \boldsymbol{W}^2). \tag{18c}$$

The latter can reduce to $\boldsymbol{\varepsilon}_b := \boldsymbol{E}$, if we can assume $\boldsymbol{W}$ to be sufficiently small.

(3) *Constitutive equations.* The constitutive equations, in terms of the fiber generalized parameters $\boldsymbol{t}[s]$ and $\bar{\boldsymbol{d}}[s]$, are recovered by entering the corotational tensors into the mixed form of the strain energy (3). When writing the strain work $\sigma\varepsilon$ and the complementary energy Ψ in the form

$$\sigma\varepsilon := \int \mathcal{W}[s]\, ds, \qquad \Psi := \int \psi[s]\, ds, \tag{18d}$$

the local strain work $\mathcal{W}[s]$ and the local complementary energy $\psi[s]$ will be defined as

$$\mathcal{W}[s] := \int_{\mathcal{S}[s]} \boldsymbol{\sigma}_b[\boldsymbol{t}] \cdot \boldsymbol{\varepsilon}_b[\boldsymbol{d}]\, d\mathcal{S}, \tag{18e}$$

$$\psi[s] := \frac{1}{2}\int_{\mathcal{S}[s]} \boldsymbol{\sigma}_b[\boldsymbol{t}] \cdot \boldsymbol{C}_b\boldsymbol{\sigma}_b[\boldsymbol{t}]\, d\mathcal{S}, \tag{18f}$$

where $\boldsymbol{C}_b$ is the compliance tensor that ICM assumes as defined by linear theory as $\boldsymbol{C}_b \approx \boldsymbol{C}_L$. Performing the integration, the previous equations can be rewritten in terms of generalized parameters $\boldsymbol{t}$ and $\bar{\boldsymbol{d}}$ as:

$$\mathcal{W}[s] = \boldsymbol{t}^T \boldsymbol{\varrho}[\bar{\boldsymbol{d}}], \qquad \psi[s] = \tfrac{1}{2}\boldsymbol{t}^T \boldsymbol{H}\boldsymbol{t}, \tag{18g}$$

$\boldsymbol{\varrho}[\bar{\boldsymbol{d}}]$ being the generalized strain, work-conjugate with $\boldsymbol{t}$, and $\boldsymbol{H}$ a generalized compliance operator. The local constitutive law is then obtained directly from (1) and (18g), by differentiating with respect to $\boldsymbol{t}$:

$$\boldsymbol{\varrho}[\bar{\boldsymbol{d}}] = \boldsymbol{H}\boldsymbol{t}. \tag{18h}$$

(4) *Change of observer.* To complete the nonlinear modeling we only need to express the generalized strain $\boldsymbol{\varrho}[s]$, obtained in Step (3) as a function of the corotational displacement parameters $\bar{\boldsymbol{d}}[s]$, in terms of $\boldsymbol{d}[s]$. As these are related by the change of observer relationships (18a), the frame independence is assured by definition.

The nonlinear model so obtained will satisfy the objectivity requirements with respect to rigid rotations of the fiber exactly, while exploiting the full details of the linear solution, including the nonlinear effects due to the fiber warping which are kept by (12) within second-order accuracy.

Note also that, being based on the mixed variational condition (1) through a separate description for the stress and displacement fields, the model provides in general a mixed approximate solution. Apart from

the simplified assumptions already contained in the linear theory, the error is, however, only produced by the pointwise differences (16) in the strain as evaluated from the displacement field or from the stress field, which is only related to the rotation residual $\boldsymbol{\omega}[s]$ due to warping. Moreover, its effect is further zeroed on average by the use of the integral formulation (18e)–(18h), so it can be considered as negligible.

Obviously, accepting less accuracy, a series of variants of the method are possible, such as the use of a linear approximation for $\boldsymbol{\varepsilon}_b$ ($\boldsymbol{\varepsilon}_b := \boldsymbol{E}$), by making $\boldsymbol{\omega} \approx \mathbf{0}$. Some of these variants will be discussed in the following section.

4. Some tutorial implementations of ICM

To better illustrate our proposal, it is convenient to consider the implementation of ICM in some simple tutorial contexts. This gives us the opportunity to clarify the details of the method, check its accuracy in practical cases, and also examine the effects of different approximations.

4.1. ***Planar beam with rectangular cross section.*** Consider the planar beam in Figure 1, with a rectangular cross section of dimensions h and $b \ll h$. Assuming as reference its straight undeformed configuration, the beam is referred through a Cartesian material system $\boldsymbol{X} := \{s, y\}$, s being aligned with the barycentric axis and y with the cross section.

Obtaining a linear solution. A linear solution is provided in this case by Saint-Venant–Jourasky theory [Timoshenko 1955]. By referring to an appropriate (corotational) spatial system $\bar{\boldsymbol{x}} := \{\bar{x}_1, \bar{x}_2\}$, aligned with the current section $\mathcal{S} := \mathcal{S}[s]$ as shown in Figure 1, and denoting with $\sigma_L[s, y]$ and $\tau_L[s, y]$ the normal and tangential components of the stress field, these are locally (that is, on $\mathcal{S}$) given by:

$$\sigma_L := \frac{1}{A} N[s] - \frac{y}{J} M[s], \quad \tau_L := \frac{\zeta_{,y}[y]}{A} T[s], \tag{19a}$$

where, according to the usual notation, $A = bh$ and $J = bh^3/12$ are the area and inertia of the section, respectively, $\zeta[y]$ is the so-called stress function expressed in our case by

$$\zeta := \frac{3h^2 y - 4y^3}{2h^2}, \quad \int_S \zeta \, dA = 0, \quad \int_S \zeta_{,y} \, dA = A, \tag{19b}$$

and $N[s]$, $T[s]$, and $M[s]$ are the axial, shear and flexural strengths, respectively, defined, as usual, by

$$N := \int_S \sigma_L[s, y] \, dA, \quad T := \int_S \tau_L[s, y] \, dA, \quad M := \int_S y \sigma_L[s, y] \, dA. \tag{19c}$$

Furthermore, denoting with $\bar{u}_1[s, y]$ and $\bar{u}_2[s, y]$ the components of the displacement field in the spatial system $\{\bar{x}_1, \bar{x}_2\}$, these are locally (that is, in a neighborhood of $\mathcal{S}$) given by

$$\begin{aligned} \bar{u}_1[s + ds, y] &= \bar{u}[s + ds] - \bar{\varphi}[s + ds] y + \gamma_L[s] w[y], \\ \bar{u}_2[s + ds, y] &= \bar{v}[s + ds], \end{aligned} \tag{20a}$$

where

$$\bar{u}[s + ds] := \varepsilon_L[s] \, ds \quad \text{and} \quad \bar{v}[s + ds] := (\theta[s] + \gamma_L[s]) \, ds + \mathbb{O}(ds^2), \tag{20b}$$

are the *average translations* of the section in the $\bar{x}_1$ and $\bar{x}_2$ directions,

$$\bar{\varphi}[s + ds] := \theta[s] + \chi_L[s] \, ds + \mathbb{O}(ds^2) \tag{20c}$$

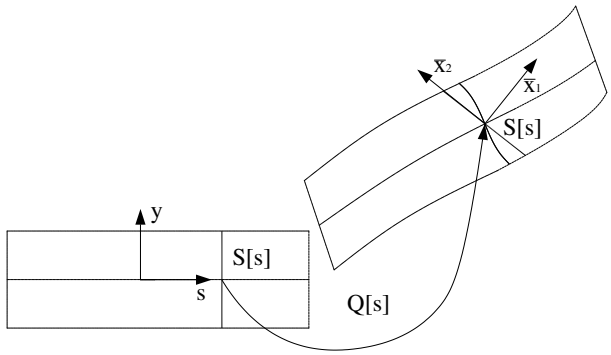

Figure 1. Planar beam with thin rectangular cross section.

is its *average rotation*, and $w[y]$ is the so-called warping function defined by

$$w := \zeta/k - y, \quad k := \frac{1}{A}\int_S \zeta,_y^2 \, dA = 6/5, \tag{20d}$$

k being the so-called shear factor and θ a rotation parameter which defines the orientation of the local frame chosen in order to maximize accuracy: for $\theta = 0$ (that is, $\bar{\varphi}[s] = 0$) the frame is locally aligned with the section and for $\theta = -\gamma_L$ (that is, $\bar{v},_s[s] = 0$) it is aligned with the axis line.

The previous expressions allow the recovery of the displacement gradient field $\nabla \boldsymbol{u}[y] = \boldsymbol{E}[y] + \boldsymbol{W}[y]$ on the current section $\mathcal{S}$. We obtain

$$\boldsymbol{E} = \begin{bmatrix} \varepsilon_L - \chi_L y & \gamma_L \zeta,_y /2k \\ \text{sym.} & 0 \end{bmatrix}, \quad \boldsymbol{W} = \begin{bmatrix} 0 & \gamma_L(\zeta,_y /2k - 1) - \theta \\ \text{skew} & 0 \end{bmatrix}. \tag{20e}$$

From the previous equations, we have

$$\varepsilon_L := \bar{u},_s[s], \quad \gamma_L := \bar{v},_s[s] - \bar{\varphi}[s], \quad \chi_L := \bar{\varphi},_s[s], \tag{20f}$$

so, apart from the alignment parameter θ, the local kinematics $\boldsymbol{E}[\bar{\mathcal{S}}]$ and $\boldsymbol{W}[\bar{\mathcal{S}}]$ are completely defined by the local derivatives $\bar{u},_s$, $\bar{v},_s$, and $\bar{\varphi},_s$ of the translations $\bar{u}[s]$ and $\bar{v}[s]$ and the rotation $\bar{\varphi}[s]$ associated with the section. It is also convenient to introduce the quantities

$$\bar{\alpha}[s + ds] := \bar{\varphi}[s + ds] - \theta[s]. \tag{20g}$$

Obviously we have $\bar{\alpha}[s] = 0$ and $\bar{\alpha},_s = \bar{\varphi},_s$. These conditions implicitly define the alignment of the local corotational observer associated with the section s. In fact assuming $\alpha[s]$ to be a finite rotation angle associated with the fiber $\mathcal{S}$, as viewed by a fixed observer, and $\bar{\alpha}$ its value viewed by a local observer, this implies a relative alignment angle $\bar{\alpha}[s] - \alpha[s] = -\alpha[s]$ between the two observers and defines the rotation matrix

$$\boldsymbol{Q}[s] := \begin{bmatrix} \cos\alpha & -\sin\alpha \\ \sin\alpha & \cos\alpha \end{bmatrix}, \tag{20h}$$

relating the two observers.

Recovering nonlinear stresses, strains, and constitutive equations. As stated in the previous section, we assume that the Biot stress field $\boldsymbol{\sigma}_b$ is directly described by (19a), its relevant components being defined by $\sigma_{11} = \sigma_L$ and $\sigma_{12} = \tau_L$. By substitution into (18f), we obtain

$$\psi[s] := \frac{1}{2}\int_{\bar{\mathcal{F}}}\left(\frac{\sigma_{11}^2}{E} + \frac{\sigma_{12}^2}{G}\right) dA = \frac{1}{2}\left(\frac{N^2}{EA} + \frac{kT^2}{GA} + \frac{M^2}{EJ}\right), \tag{21a}$$

E and G being the normal and shear elastic moduli of the material. Conversely, the Biot strain field will be obtained by substituting (20e) into (12). The evaluation of internal work (18e) provides

$$\mathcal{W}[s] := \int_S (\sigma_{11}\varepsilon_{11} + 2\sigma_{12}\varepsilon_{12})\, dA = N\varepsilon + T\gamma + M\chi, \tag{21b}$$

where the strain parameters ε, γ, and χ are defined by:

$$\varepsilon := \varepsilon_L + \tfrac{19}{48}\gamma_L^2 + \theta\gamma_L + \tfrac{1}{2}\theta^2, \quad \gamma := \gamma_L - \varepsilon_L(\theta + \tfrac{1}{2}\gamma_L), \quad \chi := \chi_L,$$

that is, recalling (20f) and (20g),

$$\varepsilon := \bar{u}_{,s} + \tfrac{19}{48}\bar{v}_{,s}^{\,2} + \tfrac{10}{48}\theta\bar{v}_{,s} - \tfrac{5}{48}\theta^2, \quad \gamma := \bar{v}_{,s} - \theta - \tfrac{1}{2}\bar{u}_{,s}\,(\bar{v}_{,s} + \theta), \quad \chi := \bar{\alpha}_{,s}\,. \tag{21c}$$

By relating (21a) and (21b) through the Clapeyron equivalence $2\Phi_c = \mathcal{W}$, we also obtain

$$N = EA\varepsilon, \quad T = kGA\gamma, \quad M = EJ\chi, \tag{21d}$$

which provides the elastic laws for the nonlinear model.

Applying corotational kinematics. Equations (21a)–(21d) provide the explicit expressions for the local energy terms needed for the use of the variational condition (1)–(3). In order to complete the ICM nonlinear modeling, we need to relate the displacements $\bar{u}[s]$ and $\bar{v}[s]$ and the rotation $\bar{\varphi}[s]$ associated with the section $\mathcal{S}[s]$, defined by reference to the local corotational frame $\{\bar{x}_1, \bar{x}_2\}$, with the corresponding $u[s]$, $v[s]$, and $\varphi[s]$ referred to a global fixed frame x_1, x_2. The relationship is governed by (18a). The two systems are related by the rotation matrix (20h), so we have

$$\bar{u}_{,s}\,[s] = (u_{,s} + 1)\cos\alpha + v_{,s}\sin\alpha - 1, \quad \bar{v}_{,s}\,[s] = v_{,s}\cos\alpha - (u_{,s} + 1)\sin\alpha, \quad \bar{\alpha}_{,s}\,[s] = \alpha_{,s}\,. \tag{22}$$

This relationship, when coupled with (21c), provides the nonlinear relationships between the generalized strain $\boldsymbol{\varrho}[\boldsymbol{d}] = \{\varepsilon, \gamma, \chi\}$ and the generalized displacement $\boldsymbol{d} = \{u_{,s}\,, v_{,s}\,, \varphi_{,s}\,\}$, which completes the definition of the nonlinear model. Note that, in order to obtain an explicit expression for ε and γ, we need to set the alignment parameter θ in (21c). The ICM accuracy being related to the smallness of the rotation residual $\boldsymbol{\omega}$, an appropriate choice could be that of the zeroing tensor $\boldsymbol{W}$ in weighted average, that is,

$$\int_{\bar{S}} \zeta_{,y}\,(\theta - (1 - \psi_{,y}\,/2k))\, dA = 0,$$

which provides $\theta = -\gamma_L/2$, and corresponds to an average alignment between the section and the axis line. By this choice we obtain

$$\varepsilon := \bar{u}_{,s} + \tfrac{1}{12}\bar{v}_{,s}^{\,2}\,, \quad \gamma := 2\bar{v}_{,s}\,, \quad \chi := \bar{\alpha}_{,s}\,. \tag{23}$$

However, other choices are also possible, for example, the choice $\theta = 0$ (aligned with the section) or $\theta = -\gamma_L$ (aligned with the line axis). Different choices only reflect how the alignment of the corotational frame treats the average rotation $\frac{1}{2}\gamma_L$ due to warping; it is accounted for exactly through (22) by the choice $\theta = -\gamma_L/2$ and only to second-order accuracy by the other choices, while the use of corotational algebra (22) always assures, by definition, frame independence with respect to a rigid rotation of the section. Different choices only produce a small $\mathbb{O}^3(\varepsilon_L, \gamma_L)$ difference in the final expression of $\boldsymbol{\varrho}[\boldsymbol{d}]$, so they can be considered as equivalent, within our assumption of small strains, and the actual choice could be suggested by practical convenience.

Further insights. Some further comments and remarks are useful.

(1) With regard to slender structures, we can expect $T[s]$ will be much smaller than $N[s]$ in practical contexts and then assume $\gamma \ll \varepsilon$. So, the quadratic term $\bar{v}_{,s}^{\,2}/12 = \gamma_L^2/48$ in (23) will be really very small and can be considered as irrelevant. If obliged we obtain, through (22),

$$\varepsilon = (1+u_{,s})\cos\alpha + v_{,s}\sin\alpha - 1, \quad \gamma = 2(v_{,s}\cos\alpha - (1+u_{,s})\sin\alpha), \quad \chi = \alpha_{,s}\,. \tag{24a}$$

Note that this approximation corresponds to making $\zeta_{,y}/k \approx 0$ in (20e), that is, because of (20d), assuming a linear warping $\bar{\gamma}\, w[y] \approx -\bar{\gamma}\, y$ in the evaluation $\boldsymbol{W}[s]$.

(2) The effect of warping, being related to the shear strain $\gamma[s]$, can be considered so small as to be neglected in most practical cases. Making $w[y] \approx 0$, $\boldsymbol{W}[s]$ will be zeroed by the choice $\theta = 0$ and consequently $\boldsymbol{\varepsilon}_b \approx \boldsymbol{E}$. We also have $\bar{\alpha}[s] = \bar{\varphi}[s]$, so the ICM kinematics reduce to the well known Antman beam kinematics [Antman 1995]:

$$\varepsilon = (1+u_{,s})\cos\varphi + v_{,s}\sin\varphi - 1, \quad \gamma = v_{,s}\cos\varphi - (1+u_{,s})\sin\varphi, \quad \chi = \varphi_{,s}\,. \tag{24b}$$

(3) By neglecting the shear strain everywhere, that is, assuming $\bar{\gamma} \approx 0$, we can use the condition $\gamma = 0$ in the second part of (24b) for relating φ to $u_{,s}$ and $v_{,s}$. With some algebra, (24b) becomes

$$\varepsilon = \sqrt{(1+u_{,s})^2 + v_{,s}^2} - 1, \quad \chi = \frac{v_{,ss} + v_{,ss}\,u_{,s} - v_{,s}\,u_{,ss}}{\sqrt{(1+u_{,s})^2 + v_{,s}^2}}, \tag{24c}$$

which coincide with the kinematic relationships developed in [Nayfeh and Pai 2004]. When assuming $\varepsilon \ll 1$, the previous equations can be simplified into

$$\varepsilon \approx \varepsilon + \tfrac{1}{2}\varepsilon^2 = u_{,s} + \tfrac{1}{2}(u_{,s}^2 + v_{,s}^2), \quad \chi \approx (1+\varepsilon)\chi = v_{,ss} + v_{,ss}\,u_{,s} - u_{,ss}\,v_{,s}\,. \tag{24d}$$

(4) All previous variants only differ in the treatment of shear and axial strains in the expression of $\boldsymbol{W}[s]$. When, as generally happens for slender beams, $\gamma \ll 1$ and $\varepsilon \ll 1$, their differences become negligible. To give an example, we can refer to a simply supported Euler beam of length L, subjected to a compressive axial force $F[\lambda] := \lambda\pi^2 EJ/L^2$. The analytical solution for the postbuckling path coming from the use of (24b) can be found in [Salerno and Lanzo 1997] in the form

$$\lambda = \lambda_b + \tfrac{1}{2}\ddot{\lambda}_b\xi^2 + \cdots,$$

where ξ is the end-section rotation angle and, introducing stiffness ratios $\beta_s := EJ/GAL^2$, $\beta_a := EJ/EAL^2$, and $\beta := \beta_s - \beta_a$, the buckling load λ_b and postbuckling curvature $\ddot{\lambda}_b$ are defined by

$$\lambda_b + \lambda_b^2 \beta = 1, \quad \ddot{\lambda}_b = \frac{\lambda_b}{4}\left(\frac{1+4\lambda_b\beta}{1+2\lambda_b\beta}\right).$$

The same expressions can also be obtained from (24a), if $\beta := 2\beta_s - \beta_a$, and from (24c) and (24d), assuming $\beta_s \approx 0$ and $\beta_s \approx \beta_a$, respectively (the solutions can be recovered using algebraic manipulators, so their details are omitted here). We generally have $\beta_s \ll 1$ and $\beta_a \ll 1$, so all possible choices give essentially the same result ($\lambda_b \approx 1$, $\ddot{\lambda}_b \approx 1/4$) and can be considered as equivalent for practical purposes. We can also mention that usually $\beta_a < \beta_s$, so the simpler expressions (24d) could be considered better than (24c).

(5) Finally, for a better understanding of the role of (12) in our proposal, it is convenient to refer to the limit case where the local and fixed frames coincide, that is, $\bar{u}_{,s} = u_{,s}$, $\bar{v}_{,s} = v_{,s}$. Making $\gamma_L \approx 0$ and $\bar{\varepsilon} \ll 1$ into (21c), we obtain

$$\varepsilon = u_{,s} + \tfrac{1}{2} v_{,s}^2, \quad \chi = v_{,ss}, \tag{25}$$

which correspond to the standard second-order kinematics used in simplified (technical) modelings. Obviously, this equation satisfies objectivity only to a second-order accuracy, and then requires some external tool in FEM management to obtain frame invariance at the element level (see [Garcea et al. 2009]).

4.2. ***Thin walled beam under axial force and torsion.*** Consider a spatial beam with a thin-walled cross-shaped section and subjected to axial force and torsion, as shown in Figure 2, the section thickness t being small when compared with its size h. Assuming as reference its straight undeformed configuration the beam will be referred to through a Cartesian material system $\boldsymbol{X} := \{s, y, z\}$, s being aligned with the barycentric axis and y and z lying in the cross section.

Obtaining a linear solution. A linear solution is provided in this case by the simplified Saint-Venant torsion theory for thin-walled beams [de Saint-Venant 1855]. By referring to an appropriate spatial

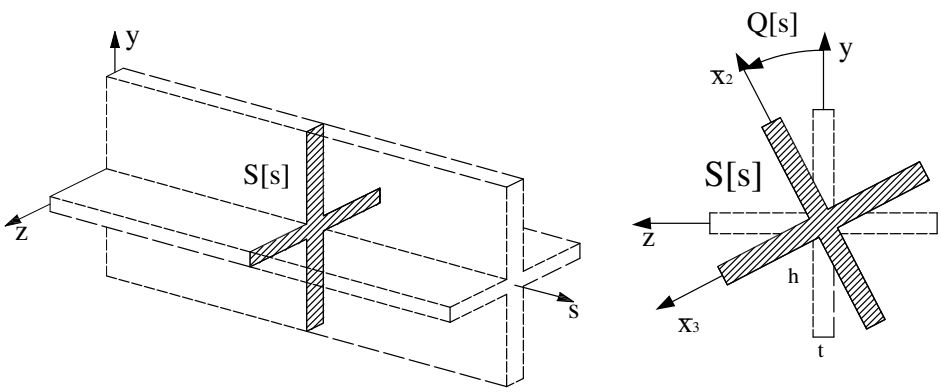

Figure 2. Cross-shaped beam under axial force and torsion.

system $\bar{\boldsymbol{x}} := \{\bar{x}_1, \bar{x}_2, \bar{x}_3\}$, aligned with the current section $\mathcal{S} := \mathcal{S}[s]$ as shown in Figure 1, and denoting with $\sigma_{xx}[s, y, z]$, $\tau_{xy}[s, y, z]$, and $\tau_{xz}[s, y, z]$ the normal and tangential components of the stress field, these are locally (that is, on $\mathcal{S}$) given by:

$$\sigma_{xx} = N[s]/A, \quad \tau_{xy} = (w[y, z],_y - z)M_t[s]/J_t, \quad \tau_{xz} = (w[y, z],_z + y)M_t[s]/J_t, \tag{26a}$$

where $w[y, z]$ is an auxiliary warping which, in the case considered, can be evaluated as

$$w[y, z] \approx \begin{cases} yz & \text{if } -t/2 \le y \le t/2, \\ -yz & \text{if } -t/2 \le z \le t/2. \end{cases} \tag{26b}$$

$A \approx 2bt$ is the area of the section, J_t is its torsional inertia, defined by

$$J_t := \int_{\bar{S}} \{(w[y, z],_y - z)^2 + (w[y, z],_z + y)^2\}\, dA \approx \tfrac{2}{3}t^3 h, \tag{26c}$$

and N and M are the strength resultants

$$N := \int_{\bar{S}} \sigma_{xx}\, dA, \quad M := \int_{\bar{S}} (\tau_{xz} y - \tau_{xy} z)\, dA. \tag{26d}$$

Furthermore, denoting with $\bar{u}_1[s, y, z]$, $\bar{u}_2[s, y, z]$, and $\bar{u}_3[s, y, z]$ the components of the displacement field in the corotational frame, these are locally given by:

$$\begin{aligned} \bar{u}_1[s + ds, y, z] &= \bar{u}[s + ds] + \chi_L[s] w[y, z], \\ \bar{u}_2[s + ds, y, z] &= -z\bar{\varphi}[s + ds], \\ \bar{u}_3[s + ds, y, z] &= y\bar{\varphi}[s + ds], \end{aligned} \tag{27a}$$

where $\bar{u}$ and $\bar{\varphi}$ are the *average axial displacement* and the *torsional rotation* of the section:

$$\bar{u}[s + ds] := \varepsilon_L[s]\, ds, \quad \bar{\varphi}[s + ds] := \chi_L[s]\, ds, \tag{27b}$$

The previous expressions allow the recovery of the displacement gradient $\nabla \boldsymbol{u}[y, z] = \boldsymbol{E}[y, z] + \boldsymbol{W}[y, z]$ field on the current section $S[s]$. We obtain

$$\boldsymbol{E} = \begin{bmatrix} \varepsilon_L & \frac{1}{2}(w,_y - z)\chi_L & \frac{1}{2}(w,_z + y)\chi_L \\ \frac{1}{2}(w,_y - z)\chi_L & 0 & 0 \\ \frac{1}{2}(w,_z - y)\chi_L & 0 & 0 \end{bmatrix},$$

$$\boldsymbol{W} = \begin{bmatrix} 0 & \frac{1}{2}(w,_y + z)\chi_L & \frac{1}{2}(w,_z - y)\chi_L \\ -\frac{1}{2}(w,_y + z)\chi_L & 0 & 0 \\ -\frac{1}{2}(w,_z - y)\chi_L & 0 & 0 \end{bmatrix}.$$

From previous equations, we have

$$\varepsilon_L[s] = \bar{u},_s[s], \quad \chi_L[s] := \bar{\varphi},_s[s], \tag{27c}$$

so the local kinematic $\boldsymbol{E}[y, z] + \boldsymbol{W}[y, z]$ is completely defined by the local derivatives of the displacement $\bar{u}[s]$ and the rotation $\bar{\varphi}[s]$ associated with the section.

Recovering nonlinear stresses, strains, and constitutive equations. Assuming that the Biot stress field $\boldsymbol{\sigma}_b$ is defined by the linear solution (26a), its relevant components being defined by $\sigma_{11} := \sigma_{xx}$, $\sigma_{12} := \tau_{xy}$, and $\sigma_{13} := \tau_{xz}$, the complementary energy (18f) and the strain work (18e) become

$$\psi[s] := \frac{1}{2}\int_A \left\{ \frac{\sigma_{11}^2}{E} + \frac{\sigma_{12}^2+\sigma_{13}^2}{G} \right\} dA = \frac{1}{2}\Big(\frac{N}{EA} + \frac{M_t}{GJ_t}\Big), \tag{28a}$$

$$\mathcal{W} = \int_A \{\sigma_{11}\varepsilon_{11} + 2\tau_{12}\varepsilon_{12} + 2\tau_{13}\varepsilon_{13}\}\, dA = N\varepsilon[s] + M\chi[s], \tag{28b}$$

where, introducing the *polar inertia*

$$J_1 := \int_{\mathcal{S}} (y^2+z^2)\, dA \approx \tfrac{1}{6} t b^3, \tag{28c}$$

the strain generalized parameters ε and χ are expressed by

$$\varepsilon[s] = \bar{u}_{,s} + \frac{(4J_1 - J_t)}{8A}\bar{\varphi}_{,s}^{\,2}, \quad \chi[s] = \bar{\varphi}_{,s} - \tfrac{1}{2}\bar{u}_{,s}\,\bar{\varphi}_{,s}\,, \tag{28d}$$

where use is made of (27c).

By relating (28a) and (28b) through Clapeyron's equivalence, we also obtain the elastic laws

$$N = EA\varepsilon, \quad M = GJ\chi, \tag{28e}$$

so completing the modeling, in the corotational reference frame.

Applying corotational kinematics. To complete the ICM modeling, we need to relate the generalized displacement derivatives $\bar{u}_s$ and $\bar{\varphi}_{,s}$, referring the corotational frame to the corresponding one referring to the fixed frame. As the relative rotation $\boldsymbol{Q}$ between the two systems is, in our case, described by a rotation vector aligned with the x_1 axis, we simply have $\bar{u}_{,s} = u_{,s}$, $\bar{\varphi}_{,s} = \varphi_{,s}$, and so we finally obtain

$$\varepsilon[s] = u_{,s} + \frac{(4J_1 - J_t)}{8A}\varphi_{,s}^{\,2}, \quad \chi[s] = \big(1 - \tfrac{1}{2}u_{,s}\big)\varphi_{,s}\,, \tag{29a}$$

which defines the nonlinear beam kinematics and, together with (28a) and (28b) completes the definition of the ICM modeling.

Note that terms J_1 and J_t appearing in the first section of (28d) take into account the rotations due to the helicoid distortion of longitudinal fibers and those due to shear strains, respectively. So we have $J_t \ll J_1$ in general (actually we have $J_t = \frac{2}{3} b t^3$ and $J_1 = \frac{1}{6} t b^3$). So, neglecting the small term $\frac{1}{2}u_{,s}$, (29a) can be simplified into

$$\varepsilon[s] := \bar{u}_{,s} + \frac{1}{2}\frac{J_1}{A}\varphi_{,s}^{\,2}, \quad \chi[s] := \varphi_{,s}\,, \tag{30}$$

which coincides with that derived by Wagner [1936] in his study of beams in torsion.

It is also worth mentioning that the term $\frac{1}{2}\varphi_{,s}^{\,2}\, J_1/A$ in the expression of ε implies a nonlinear coupling between axial elongation and torsional curvature which comes from warping and is generally neglected in approaches based on rigid motion kinematics of the section. This coupling, which we call the Wagner effect, can however play an important role in activating flexural/torsional buckling of slender thin-walled beams, as we will show in our subsequent, related paper [Garcea et al. 2012], so generally it cannot be ignored.

5. Nonlinear beam model based on Saint-Venant general rod theory

ICM is now applied to recover a nonlinear three-dimensional beam model based on the Saint-Venant (SV) general rod theory [de Saint-Venant 1855]. For full details of the SV problem we refer readers to classic works such as [Timoshenko 1955; Fichera 1977] while a numerical solution of the problem can be found in [Petrolo and Casciaro 2004]. Interesting, also for comparison with the model presented here, is [Petrov and Géradin 1998a; 1998b].

We use the same notation introduced in the tutorial section and also assume the beam is straight in its reference configuration and is referred to by a Cartesian material system $\boldsymbol{X} := \{s, y, z\}$, s being aligned with the barycentric axis and y and z with the principal direction of the cross section. We will denote with A the area and with

$$J_1 := \int_{\mathcal{S}} (y^2 + z^2)\, dA, \quad J_2 := \int_{\mathcal{S}} z^2\, dA, \quad J_3 := \int_{\mathcal{S}} y^2\, dA,$$

the polar and flexural inertia of the section. The linear solution is referred to a corotational spatial system $\bar{\boldsymbol{x}} := \{\bar{x}_1, \bar{x}_2, \bar{x}_3\}$, aligned with the current section $\mathcal{S} := \mathcal{S}[s]$, as shown in Figure 3, $\boldsymbol{Q}[s]$ being the rotation matrix relating the two systems.

5.1. ***Obtaining the SV linear solution: statics.*** ICM assumes that the Biot stress tensor components in the material frame are coincident with the stress components recovered by the linear SV solution in the corotational frame. From now on, we express the Biot stress directly as obtained by the Saint-Venant solution obtaining

$$\boldsymbol{\sigma}_b = \begin{bmatrix} \sigma & \boldsymbol{\tau}^T \\ \boldsymbol{\tau} & \mathbf{0} \end{bmatrix},$$

where $\sigma := \sigma_{11}$ is the normal stress and $\boldsymbol{\tau} := [\sigma_{12}, \sigma_{13}]^T$ collects in a single vector the tangential stresses.

Introducing the force and moment resultants $\boldsymbol{N} = \{N_1, N_2, N_3\}$ and $\boldsymbol{M} = \{M_1, M_2, M_3\}$ over the section, as usual defined by

$$\begin{aligned} N_1 &= \int_{\mathcal{S}} \sigma_{11}\, dA, & N_2 &= \int_{\mathcal{S}} \sigma_{12}\, dA, & N_3 &= \int_{\mathcal{S}} \sigma_{13}\, dA, \\ M_1 &= \int_{\mathcal{S}} (y\sigma_{13} - z\sigma_{12})\, dA, & M_2 &= \int_{\mathcal{S}} z\sigma_{11}\, dA, & M_3 &= -\int_{\mathcal{S}} y\sigma_{11}\, dA, \end{aligned} \tag{31a}$$

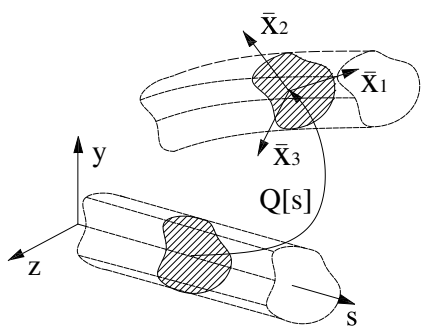

Figure 3. SV three-dimensional beam, material, and corotational frames.

and collecting them into the strength vectors

$$\boldsymbol{t}_\sigma := \begin{bmatrix} N_1 \\ M_2 \\ M_3 \end{bmatrix}, \quad \boldsymbol{t}_\tau := \begin{bmatrix} M_1 \\ N_2 \\ N_3 \end{bmatrix}, \tag{31b}$$

the stress solution can be expressed as:

$$\sigma = \boldsymbol{D}_\sigma[y,z]\boldsymbol{t}_\sigma, \quad \boldsymbol{\tau} = \boldsymbol{D}_\tau[y,z]\boldsymbol{t}_\tau, \tag{31c}$$

where

$$\boldsymbol{D}_\sigma[y,z] := \left[\frac{1}{A}, \frac{z}{J_2}, -\frac{y}{J_3}\right], \quad \boldsymbol{D}_\tau[y,z] := \begin{bmatrix} \boldsymbol{d}_2^T[y,z] \\ \boldsymbol{d}_3^T[y,z] \end{bmatrix}, \tag{31d}$$

and vectorial stress functions $\boldsymbol{d}_2[y,z]$ and $\boldsymbol{d}_3[y,z]$ are defined by a Laplace/Neumann differential problem whose numerical solution can be easily obtained through a finite element discretization of the section as, for instance, performed in [Petrolo and Casciaro 2004]. Also as in that reference, the interpolation (31c) allows us to obtain the expression of the complementary energy $\psi[s]$ associated with the current section $\mathcal{S}[s]$ in terms of the strength vectors $\boldsymbol{t}_\sigma$ and $\boldsymbol{t}_\tau$:

$$\psi[s] := \frac{1}{2}\left(\frac{1}{E}\boldsymbol{t}_\sigma^T \boldsymbol{H}_\sigma \boldsymbol{t}_\sigma + \frac{1}{G}\boldsymbol{t}_\tau^T \boldsymbol{H}_\tau \boldsymbol{t}_\tau\right), \tag{32a}$$

where

$$\boldsymbol{H}_\sigma := \int_{\mathcal{S}} \boldsymbol{D}_\sigma^T \boldsymbol{D}_\sigma \, dA, \quad \boldsymbol{H}_\tau := \int_{\mathcal{S}} \boldsymbol{D}_\tau^T \boldsymbol{D}_\tau \, dA. \tag{32b}$$

Matrix $\boldsymbol{H}_\sigma$, gives the contribution of normal stresses over the section and, being the corotational local frame aligned with the principal frame of the section, it is simply obtained as a diagonal matrix

$$\boldsymbol{H}_\sigma = \operatorname{diag}\left[\frac{1}{A} \quad \frac{1}{J_2} \quad \frac{1}{J_3}\right].$$

Matrix $\boldsymbol{H}_\tau$ gives the contribution of tangential stresses and generally results in a full symmetric matrix which can however be obtained as a by-product of the FEM solution process which provides the stress functions $\boldsymbol{d}_2[y,z]$ and $\boldsymbol{d}_3[y,z]$ (see [Petrolo and Casciaro 2004] for details). It is convenient to introduce the vector quantities

$$\boldsymbol{t} = \begin{bmatrix} \boldsymbol{N} \\ \boldsymbol{M} \end{bmatrix} \tag{32c}$$

in order to arrange (32a) in the more compact form

$$\psi[s] := \tfrac{1}{2}\boldsymbol{t}^T \boldsymbol{H}\boldsymbol{t}. \tag{32d}$$

5.2. ***Obtaining the SV linear solution: kinematics.*** As the in-plane deformation of the section must be inessential coming from the Poisson effect, the SV displacement solution, in a neighbor of $\mathcal{S}[s]$, can be expressed as

$$\begin{aligned} \bar{u}_1[s+ds, y, z] &= ds(\varepsilon_{L1} - y\chi_{L3} + z\chi_{L2}) + w[y,z], \\ \bar{u}_2[s+ds, y, z] &= ds(\varepsilon_{L2} - z\chi_{L1}) + \mathcal{O}(ds^2), \\ \bar{u}_3[s+ds, y, z] &= ds(\varepsilon_{L3} + y\chi_{L1}) + \mathcal{O}(ds^2), \end{aligned} \tag{33}$$

where the out-of-plane warping function $w[y,z]$, which can be assumed without loss of generality to satisfy the conditions

$$\int_A w[y,z]\,dA = \int_A yw[y,z]\,dA = \int_A zw[y,z]\,dA = 0, \tag{34}$$

is related to stress functions $\boldsymbol{d}_2[y,z]$ and $\boldsymbol{d}_3[y,z]$, as we will show in the sequel, and ε_{Lk} and χ_{Lk} are strain parameters to be related to the stress parameters N_k and M_k through the section constitutive law. Therefore, the displacement gradient $\nabla\bar{\boldsymbol{u}}$ assumes in $\mathcal{S}$ the following expression:

$$\nabla\bar{\boldsymbol{u}} = \begin{bmatrix} \varepsilon_L & \nabla w^T \\ \boldsymbol{\theta} & \mathbf{0} \end{bmatrix}, \tag{35a}$$

where

$$\varepsilon_L := \varepsilon_{L1} - y\chi_{L3} + z\chi_{L2}, \quad \boldsymbol{\theta} := \begin{bmatrix} \varepsilon_{L2} - z\chi_{L1} \\ \varepsilon_{L3} + y\chi_{L1} \end{bmatrix}, \quad \nabla\boldsymbol{w} := \begin{bmatrix} w_{,y} \\ w_{,z} \end{bmatrix}, \tag{35b}$$

and its symmetric and skew-symmetric parts become

$$\bar{\boldsymbol{E}} := \begin{bmatrix} \varepsilon_L & \frac{1}{2}(\boldsymbol{\theta} + \nabla w)^T \\ \frac{1}{2}(\boldsymbol{\theta} + \nabla w) & \mathbf{0} \end{bmatrix}, \quad \bar{\boldsymbol{W}} := \begin{bmatrix} 0 & -\frac{1}{2}(\boldsymbol{\theta} - \nabla w)^T \\ \frac{1}{2}(\boldsymbol{\theta} - \nabla w) & \mathbf{0} \end{bmatrix}. \tag{35c}$$

By collecting the six strain constants ε_{L1}, ε_{L2}, ε_{L3}, χ_{L1}, χ_{L2}, and χ_{L3} into the vectors

$$\bar{\boldsymbol{d}}_\sigma := \begin{bmatrix} \varepsilon_{L1} \\ \chi_{L2} \\ \chi_{L3} \end{bmatrix}, \quad \bar{\boldsymbol{d}}_\tau := \begin{bmatrix} \chi_{L1} \\ \varepsilon_{L2} \\ \varepsilon_{L3} \end{bmatrix}, \tag{35d}$$

we can express all the strain quantities in (35b) using the following interpolation defined as a solution of the linear SV problem:

$$\varepsilon_L := \boldsymbol{D}_\varepsilon[y,z]\bar{\boldsymbol{d}}_\sigma, \quad \boldsymbol{\theta} := \boldsymbol{D}_\theta[y,z]\bar{\boldsymbol{d}}_\tau, \quad \nabla w := \boldsymbol{D}_w[y,z]\bar{\boldsymbol{d}}_\tau, \tag{35e}$$

$\boldsymbol{D}_\epsilon$ and $\boldsymbol{D}_\theta$ being the interpolation matrices directly defined by

$$\boldsymbol{D}_\varepsilon := \begin{bmatrix} 1 & z & -y \end{bmatrix}, \quad \boldsymbol{D}_\theta := \begin{bmatrix} -z & 1 & 0 \\ y & 0 & 1 \end{bmatrix}, \tag{35f}$$

while $\boldsymbol{D}_w[y,z]$ is related to the stress interpolation (31c) through the elastic laws $\sigma_{12} = G\varepsilon_{12}$ and $\sigma_{13} = G\varepsilon_{13}$. Using (31c) and (32b), we obtain

$$\boldsymbol{\gamma}_L := \boldsymbol{\theta} + \nabla\boldsymbol{w} = \boldsymbol{D}_\gamma[y,z]\boldsymbol{d}_\tau, \quad \boldsymbol{D}_\gamma := \boldsymbol{D}_\tau\boldsymbol{H}_\tau^{-1}, \tag{35g}$$

and therefore

$$\boldsymbol{D}_w := \boldsymbol{D}_\gamma[y,z] - \boldsymbol{D}_\theta. \tag{35h}$$

Linear evaluation for Biot strains. We have already shown that in some cases (for example, for compact sections), the effects of warping can be ignored. That is, we can assume $\overline{\boldsymbol{W}} \approx \boldsymbol{0}$ in the Biot strain expression (12), without introducing appreciable errors. From this assumption we obtain $\boldsymbol{\varepsilon}_b = \bar{\boldsymbol{E}}$ and the internal work becomes the same as in the linear elastic case

$$\mathcal{W} := \boldsymbol{t}_\sigma^T \boldsymbol{\varrho}_\sigma + \boldsymbol{t}_\tau^T \boldsymbol{\varrho}_\tau, \quad \boldsymbol{\varrho}_\sigma := \bar{\boldsymbol{d}}_\sigma, \quad \boldsymbol{\varrho}_\tau := \bar{\boldsymbol{d}}_\tau. \tag{36a}$$

So, by rearranging the strain parameters in a single vector

$$\boldsymbol{\varrho} := \boldsymbol{d}_L = \begin{bmatrix} \boldsymbol{\varepsilon}_L \\ \boldsymbol{\chi}_L \end{bmatrix}, \quad \boldsymbol{\varepsilon}_L := \begin{bmatrix} \epsilon_{L1} \\ \epsilon_{L2} \\ \epsilon_{L3} \end{bmatrix}, \quad \boldsymbol{\chi}_L := \begin{bmatrix} \chi_{L1} \\ \chi_{L2} \\ \chi_{L3} \end{bmatrix}, \tag{36b}$$

and recalling (32d), the stationarity of the section strain energy $\psi[\boldsymbol{t}] - \mathcal{W}[\boldsymbol{t}, \boldsymbol{\omega}_L]$ with respect to stress vector $\boldsymbol{t}$ directly provides the constitutive law

$$\boldsymbol{t} = \boldsymbol{H}^{-1} \boldsymbol{\varrho}. \tag{36c}$$

Quadratic evaluation for Biot strains. More generally, the effect of warping cannot be ignored, even if we can assume $\overline{\boldsymbol{W}}[y, z]$ is small enough to allow $\boldsymbol{\varepsilon}_b$ to be evaluated by the quadratic formula (12). Using (35c) we obtain $\boldsymbol{\varepsilon}_b[y, z]$ in the form

$$\boldsymbol{\varepsilon}_b = \begin{bmatrix} \varepsilon & \boldsymbol{\gamma}^T/2 \\ \boldsymbol{\gamma}/2 & \boldsymbol{\Gamma} \end{bmatrix}, \tag{37a}$$

where its relevant components $\varepsilon[y, z]$ and $\boldsymbol{\gamma}[y, z]$ are defined by

$$\varepsilon = \varepsilon_L + \tfrac{1}{2} \boldsymbol{\theta}^T \boldsymbol{\theta} - \tfrac{1}{8} \boldsymbol{\gamma}_L^T \boldsymbol{\gamma}_L, \quad \boldsymbol{\gamma} = \boldsymbol{\gamma}_L + \tfrac{1}{2} \varepsilon_L \boldsymbol{\gamma}_L - \varepsilon_L \boldsymbol{\theta}, \tag{37b}$$

and 2×2 matrix $\boldsymbol{\Gamma}$ is inessential in our treatment, being multiplied by zero stresses when evaluating the strain work $\mathcal{W}$.

Using (31c) and (37b) and introducing the strain parameter vectors

$$\boldsymbol{\varrho}_\sigma := \begin{bmatrix} \varepsilon_{b1} \\ \chi_{b2} \\ \chi_{b3} \end{bmatrix}, \quad \boldsymbol{\varrho}_\tau := \begin{bmatrix} \chi_{b1} \\ \varepsilon_{b2} \\ \varepsilon_{b3} \end{bmatrix}, \tag{37c}$$

we have

$$\mathcal{W} := \int_{\mathcal{S}} (\sigma \varepsilon + \boldsymbol{\tau}^T \boldsymbol{\gamma}) \, dA = \boldsymbol{t}_\sigma^T \boldsymbol{\varrho}_\sigma + \boldsymbol{t}_\tau^T \boldsymbol{\varrho}_\tau, \tag{37d}$$

where

$$\boldsymbol{\varrho}_\sigma = \begin{bmatrix} \varepsilon_{L1} + \dfrac{1}{2}\left(\dfrac{J_1}{A} \chi_{L1}^2 + \epsilon_{L2}^2 + \epsilon_{L3}^2 \right) - \dfrac{1}{8} \bar{\boldsymbol{d}}_\tau^T \boldsymbol{H}_\tau^{-1} \bar{\boldsymbol{d}}_\tau \\ \chi_{L2} - \chi_{L1} \epsilon_{L2} + \dfrac{1}{2J_2} \chi_{L1}^2 J_{2r} - \dfrac{1}{8J_2} \bar{\boldsymbol{d}}_\tau^T \boldsymbol{A}_3 \bar{\boldsymbol{d}}_\tau \\ \chi_{L3} - \chi_{L1} \epsilon_{L3} - \dfrac{1}{2J_3} \chi_{L1}^2 J_{3r} + \dfrac{1}{8J_3} \bar{\boldsymbol{d}}_\tau^T \boldsymbol{A}_2 \bar{\boldsymbol{d}}_\tau \end{bmatrix}, \tag{37e}$$

$$\boldsymbol{\varrho}_\tau = \left(1 - \tfrac{1}{2} \varepsilon_{L1}\right) \bar{\boldsymbol{d}}_\tau + \tfrac{1}{2} (\chi_{L2} \boldsymbol{B}_3 - \chi_{L3} \boldsymbol{B}_2) \bar{\boldsymbol{d}}_\tau, \tag{37f}$$

hte matrices $\boldsymbol{A}_2$, $\boldsymbol{A}_3$, $\boldsymbol{B}_2$, and $\boldsymbol{B}_3$ being defined by

$$\begin{aligned} \boldsymbol{A}_2 &:= \int_A y\boldsymbol{D}_\gamma^T\boldsymbol{D}_\gamma\,dA, & \boldsymbol{A}_3 &:= \int_A z\boldsymbol{D}_\gamma^T\boldsymbol{D}_\gamma\,dA \\ \boldsymbol{B}_2 &:= \int_A y\boldsymbol{D}_\tau^T(\boldsymbol{D}_\gamma - 2\boldsymbol{D}_\theta)\,dA, & \boldsymbol{B}_3 &:= \int_A z\boldsymbol{D}_\tau^T(\boldsymbol{D}_\gamma - 2\boldsymbol{D}_\theta)\,dA, \end{aligned} \tag{37g}$$

and

$$J_{2r} := \int_{\mathcal{S}} z(y^2+z^2)\,dA, \quad J_{3r} := \int_{\mathcal{S}} y(y^2+z^2)\,dA. \tag{37h}$$

Rearranging the strain parameters in a single vector

$$\boldsymbol{\varrho}[\bar{\boldsymbol{d}}_L] := \begin{bmatrix}\boldsymbol{\varepsilon}\\ \boldsymbol{\chi}\end{bmatrix}, \quad \boldsymbol{\varepsilon} = \begin{bmatrix}\varepsilon_{b1}\\ \varepsilon_{b2}\\ \varepsilon_{b3}\end{bmatrix}, \quad \boldsymbol{\chi} = \begin{bmatrix}\chi_{b1}\\ \chi_{b2}\\ \chi_{b3}\end{bmatrix}, \tag{38}$$

and combining (37c) and (32c) we finally obtain the constitutive law in the form

$$\boldsymbol{t} = \boldsymbol{H}^{-1}\boldsymbol{\varrho}[\bar{\boldsymbol{d}}_L]. \tag{39}$$

Simplified quadratic evaluation for Biot strains. The previous equations simplify if the contribution of shear strain $\nabla w + \boldsymbol{\theta}$ is ignored in the expression of $\boldsymbol{W}$. As shown in the tutorial section its effect is generally very small and can be neglected without introducing appreciable errors. With this assumption we obtain

$$\varepsilon_b[y,z] \approx \varepsilon_L + \tfrac{1}{2}\boldsymbol{\theta}^T\boldsymbol{\theta}, \quad \boldsymbol{\gamma}_b[y,z] \approx \boldsymbol{\gamma}_L - \varepsilon_L\boldsymbol{\theta}, \tag{40a}$$

which provides

$$\boldsymbol{\varrho}_\sigma \approx \begin{bmatrix}\varepsilon_{L1}\\ \chi_{L2}\\ \chi_{L3}\end{bmatrix} + \frac{1}{2}\begin{bmatrix}\dfrac{J_1}{A}\chi_{L1}^2 + \epsilon_{L2}^2 + \epsilon_{L3}^2\\ -2\chi_{L1}\varepsilon_{L2} + \dfrac{1}{J_2}\chi_{L1}^2 J_{2r}\\ -2\chi_{L1}\varepsilon_{L3} - \dfrac{1}{J_3}\chi_{L1}^2 J_{3r}\end{bmatrix}, \tag{40b}$$

$$\boldsymbol{\varrho}_\tau \approx (1-\epsilon_{L1})\bar{\boldsymbol{d}}_\tau - (\chi_{L2}\boldsymbol{C}_3 - \chi_{L3}\boldsymbol{C}_2)\bar{\boldsymbol{d}}_\tau, \tag{40c}$$

where

$$\boldsymbol{C}_2 := \int_A y\boldsymbol{D}_\tau^T\boldsymbol{D}_\theta\,dA, \quad \boldsymbol{C}_3 := \int_A z\boldsymbol{D}_\tau^T\boldsymbol{D}_\theta\,dA, \tag{40d}$$

These expressions can be further simplified if neglecting nonlinear terms related to the shear strain in the case of a symmetric section. We obtain

$$\boldsymbol{\varrho}_\sigma \approx \begin{bmatrix}\varepsilon_{L1} + \dfrac{1}{2}\dfrac{J_1}{A}\chi_{L1}^2\\ \chi_{L2}\\ \chi_{L3}\end{bmatrix}, \quad \boldsymbol{\varrho}_\tau \approx \begin{bmatrix}\chi_{L1}\\ \varepsilon_{L2}\\ \varepsilon_{L3}\end{bmatrix}. \tag{41}$$

Note that the remaining nonlinear term $\frac{1}{2}\chi_{L1}^2 J_1/A$ takes into account the so-called Wagner axial/torsional coupling.

5.3. ***Applying corotational kinematics.*** Note that the strain parameters ε_k in (33) correspond to the derivatives, with respect to s, of the components $\bar{u}_k[s, 0, 0]$ of the average displacement $\bar{\boldsymbol{u}}[s]$ of the section. Analogously, χ_k correspond to the derivatives, with respect to s, of the components $\bar{\varphi}_k$ of the average rotation vector $\bar{\boldsymbol{\varphi}}[s]$ associated with the section $\mathcal{S}$. So the SV kinematical solution is completely defined by the generalized strain parameters

$$\bar{\boldsymbol{u}}_{,s}[s] = \boldsymbol{\varepsilon}_L, \quad \bar{\boldsymbol{\varphi}}_{,s}[s] = \boldsymbol{\chi}_L, \tag{42a}$$

the first $\bar{\boldsymbol{u}}_{,s}$ being a derivative of a displacement and the second a derivative of a rotation vector. Recalling that $\bar{\boldsymbol{\varphi}}[s] = \boldsymbol{0}$, the latter can be related to a derivative of a rotation matrix $\bar{\boldsymbol{R}}[s]$ through (6) and (5c):

$$\bar{\boldsymbol{R}}_{,s}[s] := \operatorname{spin}(\bar{\boldsymbol{\varphi}}_{,s}) = \begin{bmatrix} \cdot & -\bar{\varphi}_{3,s} & \bar{\varphi}_{2,s} \\ \bar{\varphi}_{3,s} & \cdot & -\bar{\varphi}_{1,s} \\ -\bar{\varphi}_{2,s} & \bar{\varphi}_{1,s} & \cdot \end{bmatrix}. \tag{42b}$$

Displacements $\bar{\boldsymbol{u}}[s]$ and rotations $\bar{\boldsymbol{R}}[s]$, defined by reference to the local corotational frame $\{\bar{x}_1, \bar{x}_2, \bar{x}_3\}$, are related to the corresponding ones $\boldsymbol{u}[s]$ and $\boldsymbol{R}[s]$, referring to a global fixed frame through a change in the observer characterized by a relative rotation $\boldsymbol{Q}[s] = \boldsymbol{R}[s]\bar{\boldsymbol{R}}[s]^T$. As $\bar{\boldsymbol{R}} = \boldsymbol{I}$, we have $\boldsymbol{Q} = \boldsymbol{R}$, and therefore from (18a) we obtain

$$\bar{\boldsymbol{u}}_{,s}[s] = \boldsymbol{R}[s]^T(\boldsymbol{u}_{,s} + \boldsymbol{e}_1) - \boldsymbol{e}_1, \quad \bar{\boldsymbol{R}}_{,s}[s] = \boldsymbol{R}^T\boldsymbol{R}_{,s}. \tag{42c}$$

Note that, if using a linear evaluation for the Biot strain, that is, if referring to (36), we recover the Antman–Simo nonlinear beam model kinematics (see [Simo 1986; Antman 1995]). We also recover appropriate constitutive laws directly derived from the Saint-Venant theory without the need for ad hoc assumptions. With the use of the complete quadratic evaluation (37) for Biot strains, we also recover the full subtle effects due to the section warping. When using the simplified quadratic evaluation (40) we obtain a quite simple expression which still however takes into account the nonlinear Wagner coupling due to torsional distortion. A FEM implementation of this model is given in our subsequent, related paper [Garcea et al. 2012], and its results also show the strong influence of Wagner coupling in cases of flexural/torsional buckling.

6. Nonlinear plate model based on Mindlin–Reissner plate theory

ICM is further applied in this section for recovering nonlinear plate models based on the Mindlin–Reissner and Kirchhoff plate theories. The aim is to obtain objective models suitable for the nonlinear analysis of thin walled structures, such as those already analyzed in [Lanzo et al. 1995; Lanzo and Garcea 1996; Casciaro et al. 1998; Garcea 2001].

We assume the plate to be planar in its reference configuration and refer to a material system $\boldsymbol{X} = \{x_1, x_2, x_3\}$ where x_1 and x_2 lie in the middle plane, as shown in Figure 4, and $-h/2 \le x_3 \le h/2$, h being the plate thickness, moves along the transverse fiber $\mathcal{S} = \mathcal{S}(\boldsymbol{s})$, $\boldsymbol{s} := \{x_1, x_2\}$ being a two-dimensional abscissa moving in the middle plane. The linear solution applies to a neighbor of $\mathcal{S}$ and will be referred

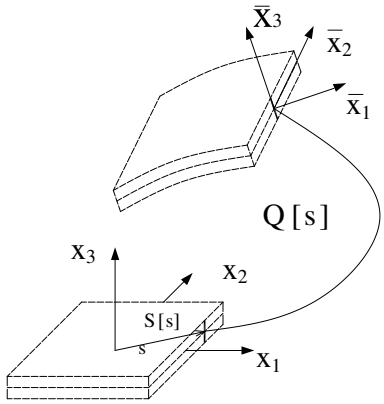

Figure 4. Plate model: kinematics.

to a corotational spatial frame $\bar{\boldsymbol{x}} = \{\bar{x}_1, \bar{x}_2, \bar{x}_3\}$ aligned with the fiber, $\boldsymbol{Q}[\boldsymbol{s}]$ being the rotation matrix relating the fixed and corotational frames.

6.1. ***Obtaining a linear solution: Statics.*** The stress solution in linear Mindlin–Reissner plate theory corresponding to fiber $\mathcal{S}[x_1, x_2]$, identified as Biot strains, can be described by

$$\boldsymbol{\sigma} := \frac{1}{h}\begin{bmatrix} N_{11} & N_{12} & \zeta_{,3}\, T_1 \\ \cdot & N_{22} & \zeta_{,3}\, T_2 \\ \text{sym.} & \cdot & 0 \end{bmatrix} + \frac{z}{J}\begin{bmatrix} M_{11} & M_{12} & 0 \\ \cdot & M_{22} & 0 \\ \text{sym.} & \cdot & 0 \end{bmatrix}, \tag{43a}$$

where $J := h^3/12$ is the flexural inertia of the plate, $\zeta[x_3]$ is the stress function defined by (see also (19b))

$$\zeta := \frac{3h^2 x_3 - 4x_3^3}{2h^2}, \quad \int_{-h/2}^{h/2} \zeta \, dx_3 = 0, \quad \int_{-h/2}^{h/2} \zeta_{,3} \, dx_3 = h, \tag{43b}$$

and, making $i, j = 1, 2$,

$$N_{ij}[\boldsymbol{s}] := \int_{-h/2}^{h/2} \sigma_{ij} \, dx_3, \quad T_i[\boldsymbol{s}] := \int_{-h/2}^{h/2} \sigma_{i3} \, dx_3, \quad M_{ij}[\boldsymbol{s}] := \int_{-h/2}^{h/2} z\sigma_{ij} \, dx_3, \tag{43c}$$

are the plate strengths we collect into the in-plane strength $\boldsymbol{N} := \{N_{11}, N_{12}, N_{22}\}$, the shear strength $\boldsymbol{T} := \{T_1, T_2\}$, and the bending moment $\boldsymbol{M} := [M_{11}, M_{22}, M_{12}]$.

Obtaining a linear solution: kinematics. The displacement field is provided by Mindlin–Reissner theory and can be expressed, in a neighbor of $\mathcal{S}[\boldsymbol{s}]$, in the form

$$\begin{aligned} \bar{u}_1[\boldsymbol{s} + d\boldsymbol{s}, x_3] &:= \bar{u}_{01}[\boldsymbol{s} + d\boldsymbol{s}] + x_3 \bar{\varphi}_2[\boldsymbol{s} + d\boldsymbol{s}] + w[x_3] \bar{u}_{03,1}[\boldsymbol{s}], \\ \bar{u}_2[\boldsymbol{s} + d\boldsymbol{s}, x_3] &:= \bar{u}_{02}[\boldsymbol{s} + d\boldsymbol{s}] - x_3 \bar{\varphi}_1[\boldsymbol{s} + d\boldsymbol{s}] + w[x_3] \bar{u}_{03,2}[\boldsymbol{s}], \\ \bar{u}_3[\boldsymbol{s} + d\boldsymbol{s}, x_3] &:= \bar{u}_{03}[\boldsymbol{s} + d\boldsymbol{s}], \end{aligned} \tag{44a}$$

where

$$\begin{aligned} \bar{u}_{0i}[\boldsymbol{s} + d\boldsymbol{s}] &:= \bar{u}_{0i,1}[\boldsymbol{s}]\, dx_1 + \bar{u}_{0i,2}[\boldsymbol{s}]\, dx_2, \qquad i = 1, 2, 3, \\ \bar{\varphi}_i[\boldsymbol{s} + d\boldsymbol{s}] &:= \bar{\varphi}_{i,1}[\boldsymbol{s}]\, dx_1 + \bar{\varphi}_{i,2}[\boldsymbol{s}]\, dx_2, \qquad i = 1, 2, \end{aligned} \tag{44b}$$

are the components of mean displacement and rotation vectors of the fiber $\mathcal{S}[s]$, and $w[x_3]$ the warping function defined by

$$w := \zeta/k - x_3, \quad k := \frac{1}{A}\int_S \zeta_{,3}^2 \, dA = 6/5. \tag{44c}$$

Note that assumption (44b) provides $\bar{\varphi}_1[s] = \bar{\varphi}_2[s] = 0$, where the alignment of the $\bar{x}_1$ and $\bar{x}_2$ axes is implicitly set to be orthogonal to the fiber. To complete the alignment we need to fix their in-plane drilling orientation by correspondence to $\bar{\varphi}_3[s] = 0$. We assume that it is set such that

$$\bar{u}_{01,2} = \bar{u}_{02,1}\,. \tag{44d}$$

The expression for the displacement gradient consequently becomes

$$\nabla\bar{\boldsymbol{u}} := \begin{bmatrix} \bar{u}_{01,1} + \bar{\varphi}_{2,1}\, x_3 & \bar{u}_{02,1} + \bar{\varphi}_{2,2}\, x_3 & \bar{u}_{03,1}\, w_{,3} \\ \bar{u}_{02,1} - \bar{\varphi}_{1,1}\, x_3 & \bar{u}_{02,2} - \bar{\varphi}_{1,2}\, x_3 & \bar{u}_{03,2}\, w_{,3} \\ \bar{u}_{03,1} & \bar{u}_{03,2} & 0 \end{bmatrix}. \tag{44e}$$

6.2. ***Recovering nonlinear strains and constitutive equations.*** Starting from the stress interpolation (43a), the complementary energy is obtained in the standard form

$$\psi[s] := \tfrac{1}{2}\{\boldsymbol{N}^T\boldsymbol{C}_n\boldsymbol{N} + \boldsymbol{T}^T\boldsymbol{C}_t\boldsymbol{T} + \boldsymbol{M}^T\boldsymbol{C}_m\boldsymbol{M}\}, \tag{45a}$$

where $\boldsymbol{C}_n$, $\boldsymbol{C}_t$, and $\boldsymbol{C}_m$ are the standard matrices of elastic moduli

$$\boldsymbol{C}_n := \frac{hE}{1-\nu^2}\begin{bmatrix} 1 & \nu & 0 \\ \nu & 1 & 0 \\ 0 & 0 & (1-\nu)/2 \end{bmatrix}, \quad \boldsymbol{C}_t := \frac{5Gh}{6}\begin{bmatrix} 1 & 0 \\ 0 & 1 \end{bmatrix}, \quad \boldsymbol{C}_m := \frac{J}{h}\boldsymbol{C}_n. \tag{45b}$$

Collecting the stress parameters in a single vector $\boldsymbol{t} := \{\boldsymbol{N}, \boldsymbol{T}, \boldsymbol{M}\}$, (45a) can be written in compact form as

$$\psi[s] = \tfrac{1}{2}\boldsymbol{t}^T\boldsymbol{H}\boldsymbol{t}. \tag{45c}$$

The generalized strain parameters can be obtained by comparing the previous equation with the expression of strain work

$$\mathcal{W}[s] = \int_{x_3=-h/2}^{h/2} \boldsymbol{\sigma}_b \cdot \boldsymbol{\varepsilon}_b \, dx_3,$$

where the Biot stress $\boldsymbol{\sigma}_b$ is directly identified with the linear solution (43a) and the corresponding strain $\boldsymbol{\varepsilon}_b$ with the displacement solution (44e) given by the quadratic approximation (12). Performing integration, we obtain

$$\mathcal{W}[s] = \boldsymbol{t}^T\boldsymbol{\varrho} \quad \Rightarrow \quad \boldsymbol{\varrho} = \boldsymbol{H}\boldsymbol{t}, \tag{46}$$

the generalized strain parameter vector $\boldsymbol{\varrho}$ being defined by

$$\boldsymbol{\varrho} := \begin{bmatrix} \boldsymbol{\varepsilon} \\ \boldsymbol{\gamma} \\ \boldsymbol{\chi} \end{bmatrix} = \boldsymbol{\varrho}_L + \boldsymbol{\varrho}_Q, \quad \boldsymbol{\varrho}_L = \begin{bmatrix} \boldsymbol{\varepsilon}_L \\ \boldsymbol{\gamma}_L \\ \boldsymbol{\chi}_L \end{bmatrix}, \quad \boldsymbol{\varrho}_Q = \begin{bmatrix} \boldsymbol{\varepsilon}_Q \\ \boldsymbol{\gamma}_Q \\ \boldsymbol{\chi}_Q \end{bmatrix}, \tag{47a}$$

where

$$\boldsymbol{\varepsilon}_L := \begin{bmatrix} \bar{u}_{01,1} \\ \bar{u}_{02,2} \\ \bar{u}_{01,2} + \bar{u}_{02,1} \end{bmatrix}, \quad \boldsymbol{\gamma}_L := \begin{bmatrix} \bar{u}_{03,1} \\ \bar{u}_{03,2} \end{bmatrix}, \quad \boldsymbol{\chi}_L := \begin{bmatrix} \bar{\varphi}_{2,1} \\ -\bar{\varphi}_{1,2} \\ \bar{\varphi}_{2,2} - \bar{\varphi}_{1,1} \end{bmatrix}, \tag{47b}$$

and

$$\begin{aligned} \boldsymbol{\varepsilon}_Q &:= \begin{bmatrix} \frac{19}{48}\bar{u}_{03,1}^2 + \frac{J}{8h}(2\bar{\varphi}_{2,2}\,\bar{\varphi}_{1,1} - \bar{\varphi}_{2,2}^2 + 3\bar{\varphi}_{1,1}^2) \\ \frac{19}{48}\bar{u}_{03,2}^2 + \frac{J}{8h}(2\bar{\varphi}_{2,2}\,\bar{\varphi}_{1,1} - \bar{\varphi}_{1,1}^2 + 3\bar{\varphi}_{2,2}^2) \\ \frac{19}{24}\bar{u}_{03,1}\,\bar{u}_{03,2} + \frac{J}{2h}(\bar{\varphi}_{1,1} + \bar{\varphi}_{2,2})(\bar{\varphi}_{1,2} + \bar{\varphi}_{2,1}) \end{bmatrix}, \\ \boldsymbol{\gamma}_Q &:= -\frac{1}{2}\begin{bmatrix} \bar{u}_{03,2}\,\bar{u}_{02,1} + \bar{u}_{03,1}\,\bar{u}_{01,1} \\ \bar{u}_{03,1}\,\bar{u}_{02,1} + \bar{u}_{03,2}\,\bar{u}_{02,2} \end{bmatrix}, \\ \boldsymbol{\chi}_Q &:= \frac{1}{2}\begin{bmatrix} -\bar{u}_{02,1}\,\bar{\varphi}_{1,1} - \bar{u}_{02,1}\,\bar{\varphi}_{2,2} \\ \bar{u}_{02,1}\,\bar{\varphi}_{1,1} + \bar{u}_{02,1}\,\bar{\varphi}_{2,2} \\ (\bar{u}_{01,1} + \bar{u}_{02,2})\bar{\varphi}_{2,2} - (\bar{u}_{02,2} - \bar{u}_{01,1})\bar{\varphi}_{1,1} \end{bmatrix}. \end{aligned} \tag{47c}$$

6.3. ***Applying corotational kinematics.*** The plate kinematics are completely defined by the generalized displacements $\bar{\boldsymbol{u}}_{0,1}[s]$, $\bar{\boldsymbol{u}}_{0,2}[s]$, $\bar{\boldsymbol{\varphi}}_{,1}[s]$, and $\bar{\boldsymbol{\varphi}}_{,2}[s]$, which correspond to the derivatives of the average displacement and rotation vectors associated with the fiber $\mathcal{S}[s]$ and referred to the corotational system $\boldsymbol{x}$. We have $\bar{\boldsymbol{\varphi}}[s] = \boldsymbol{0}$, so the latter can be related to a derivative of a rotation matrix $\bar{\boldsymbol{R}}[s]$ through (6) and (5c). We obtain

$$\bar{\boldsymbol{R}}[s] = \boldsymbol{I}, \quad \bar{\boldsymbol{R}}_{,1}[s] = \operatorname{spin}(\bar{\boldsymbol{\varphi}}_{,1}[s]), \quad \bar{\boldsymbol{R}}_{,2}[s] = \operatorname{spin}(\bar{\boldsymbol{\varphi}}_{,2}[s]). \tag{48a}$$

In order to complete the nonlinear modeling we only need to relate this local description, in the corotational frame, to the corresponding description in a fixed global frame through changing the observer algebra (18a). Condition $\boldsymbol{Q}[s]^T\boldsymbol{R}[s] = \boldsymbol{I}$ furnishes $\boldsymbol{Q}[s] = \boldsymbol{R}[s]$ and so, from (18a), with $i = 1, 2$,

$$\bar{\boldsymbol{u}}_{0,i}[s] = \boldsymbol{R}^T(\boldsymbol{u}_{0,i} + \boldsymbol{e}_i) - \boldsymbol{e}_i, \quad \bar{\boldsymbol{R}}_{,i}[s] = \boldsymbol{R}^T\boldsymbol{R}_{,i}. \tag{48b}$$

6.4. ***Relation with nonlinear plate modeling by Simo.*** By denoting with $\{\boldsymbol{i}_1, \boldsymbol{i}_2, \boldsymbol{i}_3\}$ and $\{\boldsymbol{e}_1, \boldsymbol{e}_2, \boldsymbol{e}_3\}$ the versors of the local frame $\bar{\boldsymbol{x}}$ and the global frame $\boldsymbol{x}$, we can express $\boldsymbol{R}[s]$ in the form

$$\boldsymbol{R} = [\boldsymbol{i}_1, \boldsymbol{i}_2, \boldsymbol{i}_3]. \tag{49a}$$

Moreover, by introducing the *plate directors* $\boldsymbol{a}_i$ defined by

$$\boldsymbol{a}_i := \boldsymbol{e}_i + \boldsymbol{u}_{0,i}, \quad i = 1, 2, \tag{49b}$$

(48b) can be rewritten as

$$\bar{\boldsymbol{u}}_{0,i} = \begin{bmatrix} \boldsymbol{i}_1 \cdot \boldsymbol{a}_i \\ \boldsymbol{i}_2 \cdot \boldsymbol{a}_i \\ \boldsymbol{i}_3 \cdot \boldsymbol{a}_i \end{bmatrix} - \boldsymbol{e}_i, \quad \bar{\boldsymbol{\varphi}}_{,i} = \begin{bmatrix} \boldsymbol{i}_3 \cdot \boldsymbol{i}_{2,i} \\ -\boldsymbol{i}_3 \cdot \boldsymbol{i}_{1,i} \\ -\boldsymbol{i}_1 \cdot \boldsymbol{i}_{2,i} \end{bmatrix}, \tag{49c}$$

and, consequently, obliging the quadratic contribution $\boldsymbol{\varrho}_Q$ in (47), that is, accepting a linear approximation for the strain parameters, we obtain

$$\boldsymbol{\varepsilon}_L \approx \begin{bmatrix} \boldsymbol{i}_1 \cdot \boldsymbol{a}_1 - 1 \\ \boldsymbol{i}_2 \cdot \boldsymbol{a}_2 - 1 \\ \boldsymbol{i}_1 \cdot \boldsymbol{a}_2 + \boldsymbol{i}_2 \cdot \boldsymbol{a}_1 \end{bmatrix}, \quad \boldsymbol{\gamma}_L \approx \begin{bmatrix} \boldsymbol{i}_3 \cdot \boldsymbol{a}_1 \\ \boldsymbol{i}_3 \cdot \boldsymbol{a}_2 \end{bmatrix}, \quad \boldsymbol{\chi}_L \approx \begin{bmatrix} \boldsymbol{i}_3 \cdot \boldsymbol{i}_{1,1} \\ \boldsymbol{i}_3 \cdot \boldsymbol{i}_{2,2} \\ \boldsymbol{i}_3 \cdot (\boldsymbol{i}_{1,2} + \boldsymbol{i}_{2,1}) \end{bmatrix}, \tag{49d}$$

which coincides with what is derived in [Simo et al. 1990].

6.5. ***Rotation-free modeling for Kirchhoff thin plate.*** In some cases, for very thin plates, the effect of out-of-plane shear strain will become irrelevant, so we can assume the Kirchhoff hypotheses $\boldsymbol{\gamma}_L \approx \boldsymbol{0}$, $\boldsymbol{T}^T \boldsymbol{C}_t \boldsymbol{T} \approx 0$, that is

$$\begin{aligned} \boldsymbol{i}_3 \cdot \boldsymbol{a}_1 &= 0 \\ \boldsymbol{i}_3 \cdot \boldsymbol{a}_2 &= 0 \end{aligned} \quad \Rightarrow \quad \boldsymbol{i}_3 = \frac{\boldsymbol{a}_1 \wedge \boldsymbol{a}_2}{|\boldsymbol{a}_1 \wedge \boldsymbol{a}_2|}. \tag{50a}$$

We can also assume the in-plane strain $\boldsymbol{\varepsilon}$ is sufficiently small to be neglected in comparison with unity. Under this assumption, we obtain

$$\boldsymbol{a}_i \cdot \boldsymbol{a}_j \approx \boldsymbol{i}_i \cdot \boldsymbol{a}_j + \boldsymbol{i}_j \cdot \boldsymbol{a}_i, \quad (\boldsymbol{a}_1 \wedge \boldsymbol{a}_2) \cdot \boldsymbol{a}_{i,j} \approx \boldsymbol{i}_3 \cdot \boldsymbol{i}_{i,j}, \quad i, j = 1, 2, \tag{50b}$$

so (49c) simplifies into

$$\boldsymbol{\varepsilon}_L = \frac{1}{2} \begin{bmatrix} \boldsymbol{a}_1 \cdot \boldsymbol{a}_1 - 1 \\ \boldsymbol{a}_2 \cdot \boldsymbol{a}_2 - 1 \\ 2\boldsymbol{a}_1 \cdot \boldsymbol{a}_2 \end{bmatrix}, \quad \boldsymbol{\chi}_L = \begin{bmatrix} (\boldsymbol{a}_1 \wedge \boldsymbol{a}_2) \cdot \boldsymbol{a}_{1,1} \\ (\boldsymbol{a}_1 \wedge \boldsymbol{a}_2) \cdot \boldsymbol{a}_{2,2} \\ (\boldsymbol{a}_1 \wedge \boldsymbol{a}_2) \cdot (\boldsymbol{a}_{1,2} + \boldsymbol{a}_{2,1}) \end{bmatrix}. \tag{50c}$$

This formulation does not make explicit reference to rotation matrices and could be convenient in FEM discretizations which do not make use of nodal rotations, such as those based on spline interpolations (for example, see [Garcea 2001]). A FEM implementation of this modeling will be discussed in our subsequent, related paper [Garcea et al. 2012].

7. Further comments and remarks

Some further comments are useful for a better understanding of the proposed method and of its possible extensions.

7.1. ***Linear or quadratic recovery of Biot strains.*** The quadratic terms in the local expression of the strain (12), due to warping, are usually very small and, at least some of them, can be ignored without introducing appreciable errors. In many cases a direct identification of the linear strain, such as the Biot strain, could be sufficient for practical purposes.

This is actually true in the two implementation examples previously discussed. Warping has a negligible effect on the plate modeling discussed in Section 6, generally allowing the linearized formula (47) for the strain evaluation. In the absence of torsional distortions, the warping could also be neglected in the beam model discussed in Section 5, the only relevant contribution of warping being the Wagner coupling. Note however that warping can have a noticeable effect in other possible implementations such as, for instance, cases of laminated plates and beams.

7.2. ***Errors inherited from linear theory.*** In the implementation examples described before, the parent linear solutions have been derived from standard theories for beams and plates. The nonlinear ICM models obtained will obviously inherit all the approximations contained in these theories. More refined models can be obtained, by the same procedure, using more sophisticated theories, such as the thin-walled beam theory of Vlasov, the so-called generalized beam theories [Goncalves et al. 2009], and the anisotropic theories for plates [Nayfeh and Pai 2004].

7.3. ***Linear assumptions in nonlinear analysis.*** The initial assumption in ICM is that the nonlinear solution could be locally described by the linear one, at least qualitatively. However we must consider that, in some cases, a nonlinear solution can differ noticeably from the linear one, because of the activation of local buckling phenomena characterized by deformation patterns which play a negligible role in the linear solution and so are taken out in the linear modeling. Thin-walled beams or stiffened panels, for example, can be modeled as one-dimensional fibred continua or as equivalent orthotropic plates through homogenization criteria; this can be sufficient in linear analysis but is unable to deal with complex coupled buckling behaviors which can be better described by more detailed modeling like plates assemblage (for example, see [Lanzo and Garcea 1996; Casciaro et al. 1998]). A certain care is then always needed in selecting the appropriate parent linear theory in order to obtain a reliable and accurate nonlinear modeling.

7.4. ***Mixed versus compatible formulation.*** The mixed format, used for recovering constitutive laws in terms of generalized stress and strain parameters, plays an important role in the ICM approach. It corresponds to a better use of the first-order information achieved from linear theory. In fact, it allows the use of information on both the displacement field $\boldsymbol{u}_L$ and the stress field $\boldsymbol{\sigma}_L$, which define the linear solution.

We can derive the constitutive laws in an alternative way, that is, by using a compatible formulation where the strain energy is defined only in terms of $\boldsymbol{\varepsilon}_b[\boldsymbol{u}]$:

$$\Phi_c := \frac{1}{2}\int \boldsymbol{\varepsilon}_b \cdot \boldsymbol{C}^{-1}\boldsymbol{\varepsilon}_b \, dV. \tag{51a}$$

This expression can also be rewritten in the form

$$\Phi_c := \int \left(\boldsymbol{\varepsilon}_b \cdot \boldsymbol{\sigma} - \tfrac{1}{2}\boldsymbol{\sigma} \cdot \boldsymbol{C}\boldsymbol{\sigma}\right) dV, \quad \boldsymbol{\sigma} := \boldsymbol{C}^{-1}\boldsymbol{\varepsilon}_b, \tag{51b}$$

which looks very similar to the mixed expression

$$\Phi_m := \int \left(\boldsymbol{\varepsilon}_b \cdot \boldsymbol{\sigma}_b - \tfrac{1}{2}\boldsymbol{\sigma}_b \cdot \boldsymbol{C}\boldsymbol{\sigma}_b\right) dV. \tag{51c}$$

Note however that the two expressions differ in the definition of the stress field which is obtained from $\boldsymbol{\varepsilon}_b$, through the constitutive relation $\boldsymbol{\sigma} = \boldsymbol{C}^{-1}\boldsymbol{\varepsilon}_b$ in (51b), or directly recovered as $\boldsymbol{\sigma}_b \approx \boldsymbol{\sigma}_L$ from the linear solution in (51c). These two evaluations do not coincide as already discussed in Section 3.3.

The stresses are an important part of the linear solution, whose main goal is their accurate recovery. To assume that $\boldsymbol{\sigma}_b$ is directly recovered as $\boldsymbol{\sigma}_L$ can then be generally considered a more reliable evaluation than that obtained from the displacements in a more elaborate way, which also includes differentiations. Actually, compatible formulations tend to generate spurious third and fourth-order terms in (51a) which can produce some locking in the resulting nonlinear modeling. Generally they need some ad hoc treatment to avoid this problem.

7.5. ***Obtaining more than quadratic local accuracy.*** Note that the possibility of obtaining an accurate recovery of nonlinear kinematics is strictly related to the occurrence of two circumstances: the fact that the strain can be considered small enough that the local motion is governed by its rigid part, and the fact that a rigid rotation $\boldsymbol{R}$ can be completely defined, through expansion (5c), by its first-order estimate $\boldsymbol{W}$. We actually made use of these properties when deriving the second-order recovery relation (12).

We can obtain more accurate expressions by setting further terms in the expansion (5c) of the rotation. This could allow, at least in principle, full kinematical coherence in the recovery of rotations. However great care has to be taken in the appropriate definition of the kinematical quantities involved and a more precise evaluation of the stretch part of the motion could be required, such as, for instance, that obtained by extending the linear solution by perturbation procedures [Nayfeh 1981]. Even if the use of (12) is generally sufficient for practical applications, research in this direction could be interesting.

8. Conclusion

In the current state of the art in structural mechanics there is a lack of a suitable nonlinear models for use in nonlinear FEM analysis, in comparison with the amounts of those available for linear analysis. The purpose of this paper was reducing this gap by developing a general tool able to exploit information from existing linear models for fibered continua, such as beams or plate, to set up corresponding nonlinear models.

We proposed a general procedure, called the implicit corotational method (ICM), which consists of two logical steps. In the first, we exploit the stress and displacement fields provided by the linear theory to derive appropriate expressions for the nonlinear fields as viewed by a moving local corotational observer; in the second we transfer this description to a fixed global frame directly exploiting the change in observer algebra, so completing the nonlinear modeling and assuring frame invariance, by definition.

The former step only needs a linear solution be available. The recovery of the nonlinear fields is straightforward through a standard procedure: the stress field is directly taken from the linear field and the strain field is obtained from the linear displacements by the quadratic formula (12). The latter step introduces the geometrical nonlinearities due to the finite motion of the fiber in the modeling, simply by exploiting the objectivity requirements in a constructive way. Only the simple standard algebra defined by (18a) is involved in this step and its implementation is straightforward and does not require any ad hoc adaptation to fit the particular problem at hand.

ICM was implemented in two special, but still technically relevant, contexts: that of three-dimensional beams, according to Saint-Venant general rod theory, and plates, according to Mindlin–Reissner and Kirchhoff plate theories, a homogeneous isotropic material being assumed in both cases. We discussed these cases in detail and have shown that the resulting models can actually recover all the richness of the underlying linear solutions. We also indicated the effect of different simplification choices and have shown that, by appropriate simplifying assumptions, we can recover existing nonlinear models (for example, the beam and plate models of [Simo 1986; Antman 1995]). The method could however easily be generalized to anisotropic materials and also applied in different contexts, such as, for instance, Vlasov thin-walled beam theory, generalized beam theories [Goncalves et al. 2009], or laminated plate theory [Nayfeh and Pai 2004]. In all cases the advantage is that it provides fully objective nonlinear models by a black-box procedure which only needs the corresponding linear model to be already available.

In the our subsequent, related paper [Garcea et al. 2012] we also show that nonlinear models derived through ICM are directly suitable for numerical implementations through the use of a standard FEM technology. Numerical results will also show their accuracy and robustness in different technically relevant contexts.

References

[Antman 1995] S. S. Antman, *Nonlinear problems of elasticity*, Applied Mathematical Sciences **107**, Springer, New York, 1995.

[Auricchio et al. 2008] F. Auricchio, P. Carotenuto, and A. Reali, "On the geometrically exact beam model: a consistent, effective and simple derivation from three-dimensional finite-elasticity", *Int. J. Solids Struct.* **45**:17 (2008), 4766–4781.

[Belytschko and Glaum 1979] T. Belytschko and L. Glaum, "Application of high order corotational stretch theory to nonlinear finite elements analysis", *Comp. Struct.* **10**:1-2 (1979), 175–182.

[Bonet and Wood 1997] J. Bonet and R. D. Wood, *Nonlinear continuum mechanics for finite element analysis*, Cambridge University Press, Cambridge, 1997.

[Casciaro 2005] R. Casciaro, *Computational asymptotic post-buckling analysis of slender elastic structures*, CISM Courses and Lectures **470**, Springer, Wien, 2005.

[Casciaro et al. 1998] R. Casciaro, G. Garcea, G. Attanasio, and F. Giordano, "Pertubation approach to elastic post-buckling analysis", *Comp. Struct.* **66**:5 (1998), 585–595.

[Chen et al. 2006] H. H. Chen, W. Y. Lin, and K. M. Hsiao, "Co-rotational finite element formulation for thin-walled beams with generic open section", *Comput. Methods Appl. Mech. Eng.* **195**:19–22 (2006), 2334–2370.

[Cosserat and Cosserat 1909] E. Cosserat and F. Cosserat, *Théorie des corps déformables*, Hermann et fils, Paris, 1909.

[Fichera 1977] G. Fichera, "Remarks on Saint Venánt principle", in *I. N. Vekua 70th anniversary volume*, Moscow, 1977.

[Garcea 2001] G. Garcea, "Mixed formulation in Koiter analysis of thin-walled beam", *Comput. Methods Appl. Mech. Eng.* **190**:26-27 (2001), 3369–3399.

[Garcea et al. 1998] G. Garcea, G. A. Trunfio, and R. Casciaro, "Mixed formulation and locking in path-following nonlinear analysis", *Comput. Methods Appl. Mech. Eng.* **165**:1-4 (1998), 247–272.

[Garcea et al. 1999] G. Garcea, G. Salerno, and R. Casciaro, "Extrapolation locking and its sanitization in Koiter asymptotic analysis", *Comput. Methods Appl. Mech. Eng.* **180**:1-2 (1999), 137–167.

[Garcea et al. 2002] G. Garcea, G. A. Trunfio, and R. Casciaro, "Path-following analysis of thin-walled structures and comparison with asymptotic post-critical solutions", *Int. J. Numer. Methods Eng.* **55**:1 (2002), 73–100.

[Garcea et al. 2005] G. Garcea, G. Formica, and R. Casciaro, "A numerical analysis of infinitesimal mechanisms", *Int. J. Numer. Methods Eng.* **62**:8 (2005), 979–1012.

[Garcea et al. 2009] G. Garcea, A. Madeo, G. Zagari, and R. Casciaro, "Asymptotic post-buckling FEM analysis using a corotational formulation", *Int. J. Solids Struct.* **46**:2 (2009), 523–532.

[Garcea et al. 2012] G. Garcea, A. Madeo, and R. Casciaro, "Nonlinear FEM analysis for beams and plate assemblages based on the implicit corotational method", *J. Mech. Mater. Struct.* **7**:6 (2012), 539–574.

[Goncalves et al. 2009] R. Goncalves, P. B. Dinis, and D. Camotim, "GBT formulation to analyse the first-order and buckling behaviour of thin-walled members with arbitrary cross-sections", *Thin-Walled Struct.* **47**:5 (2009), 583–600.

[Ibrahimbegovic and Taylor 2002] A. Ibrahimbegovic and R. L. Taylor, "On the role of frame-invariance in structural mechanics models at finite rotations", *Comput. Methods Appl. Mech. Eng.* **191**:45 (2002), 5159–5176.

[Kim et al. 2005] M. Y. Kim, S. Kim, and N. Kim, "Spatial stability of shear deformable curved beams with non-symmetric thin-walled sections, I: stability formulation and closed-form solutions", *Comp. Struct.* **83**:31-32 (2005), 2525–2541.

[Lanzo and Garcea 1996] A. D. Lanzo and G. Garcea, "Koiter analysis of thin-walled structures by a finite element approach", *Int. J. Numer. Methods Eng.* **39**:17 (1996), 3007–3031.

[Lanzo et al. 1995] A. D. Lanzo, G. Garcea, and R. Casciaro, "Koiter post-buckling analysis of elastic plates", *Int. J. Numer. Methods Eng.* **38**:14 (1995), 2325–2345.

[Malvern 1969] L. Malvern, *Introduction to the mechanics of a continuous medium*, Prentice Hall, New York, 1969.

[Nayfeh 1981] A. H. Nayfeh, *Introduction to perturbation techniques*, Wiley, New York, 1981.

[Nayfeh and Pai 2004] A. H. Nayfeh and P. F. Pai, *Linear and nonlinear structural mechanics*, Wiley, Hoboken, NJ, 2004.

[Nour-Omid and Rankin 1991] B. Nour-Omid and C. C. Rankin, "Finite rotation analysis and consistent linearization using projectors", *Comput. Methods Appl. Mech. Eng.* **93**:3 (1991), 353–384.

[Pai and Nayfeh 1994] P. F. Pai and A. H. Nayfeh, "A new method for the modeling of geometric nonlinearities in structures", *Comp. Struct.* **53**:4 (1994), 877–895.

[Pai et al. 1998] P. F. Pai, A. N. Palazotto, and J. M. Greer, "Polar decomposition and appropriate strains and stresses for nonlinear structural analyses", *Comp. Struct.* **66**:6 (1998), 823–840.

[Petrolo and Casciaro 2004] A. S. Petrolo and R. Casciaro, "3D beam element based on Saint Venánt's rod theory", *Comp. Struct.* **82**:29-30 (2004), 2471–2481.

[Petrov and Géradin 1998a] E. Petrov and M. Géradin, "Finite element theory for curved and twisted beams based on exact solutions for three-dimensional solids, I: beam concept and geometrically exact nonlinear formulation", *Comput. Methods Appl. Mech. Eng.* **165**:1-4 (1998), 43–92.

[Petrov and Géradin 1998b] E. Petrov and M. Géradin, "Finite element theory for curved and twisted beams based on exact solutions for three-dimensional solids, II: anisotropic and advanced beam models", *Comput. Methods Appl. Mech. Eng.* **165**:1-4 (1998), 93–127.

[Pi et al. 2005] Y. L. Pi, M. A. Bradford, and B. Uy, "Nonlinear analysis of members curved in space with warping and Wagner effects", *Int. J. Solids Struct.* **42**:11-12 (2005), 3147–3169.

[Rankin 1986] C. C. Rankin, "An element indipendent corotational procedure for the treatment of large rotations", *J. Pressure Vessel Technol. (ASME)* **108**:2 (1986), 165–174.

[Reissner 1972] E. Reissner, "On one-dimensional finite strain beam theory: the plane problem", *J. Appl. Math. Phys.* **23**:5 (1972), 795–804.

[de Saint-Venant 1855] B. de Saint-Venant, "Mémoire sur la torsion des prismes, avec des considérations sur la flexion", *Mémoires des savants étrangers* **14** (1855), 233–560.

[Salerno and Lanzo 1997] G. Salerno and A. D. Lanzo, "A nonlinear beam finite element for the post-buckling analysis of plane frame by Koiter's perturbation approach", *Comput. Methods Appl. Mech. Eng.* **146**:3-4 (1997), 325–349.

[Simo 1986] J. C. Simo, "A three dimensional finite-strain rod model, II: computational aspect", *Comput. Methods Appl. Mech. Eng.* **58**:1 (1986), 79–116.

[Simo et al. 1990] J. C. Simo, D. D. Fox, and M. S. Rifai, "On a stress resultant geometrically exact shell model, III: computational aspects of the nonlinear theory", *Comput. Methods Appl. Mech. Eng.* **79**:1 (1990), 21–70.

[Timoshenko 1955] Timoshenko, *Strength of materials, Part I and II*, 3rd ed., Van Nostrand, 1955.

[Wagner 1936] H. Wagner, *Torsion and buckling of open section*, 1936.

[Wemper 1969] G. A. Wemper, "Finite elements, finite rotations and small strains of flexible shells", *Int. J. Solids Struct.* **10** (1969), 117–153.

[Wriggers and Gruttmann 1993] P. Wriggers and F. Gruttmann, "Thin shells with finite rotations formulated in Biot stresses, theory and finite element formulation", *Int. J. Numer. Methods Eng.* **36**:12 (1993), 2049–2071.

Received 30 May 2012. Revised 30 Aug 2012. Accepted 14 Sep 2012.

GIOVANNI GARCEA: giovanni.garcea@unical.it
Dipartimento di Modellistica per l'ingegneria, Università della Calabria, Via P. Bucci Cubo 39/C 87036 Rende (CS), Italy

ANTONIO MADEO: antonio.madeo81@unical.it
Dipartimento di Modellistica per l'ingegneria, Università della Calabria, Via P. Bucci Cubo 39/C 87036 Rende (CS), Italy

RAFFAELE CASCIARO: raffaele.casciaro@unical.it
Dipartimento di Modellistica per l'ingegneria, Università della Calabria, Via P. Bucci Cubo 39/C 87036 Rende (CS), Italy

JOURNAL OF MECHANICS OF MATERIALS AND STRUCTURES
Vol. 7, No. 6, 2012
dx.doi.org/10.2140/jomms.2012.7.539

NONLINEAR FEM ANALYSIS FOR BEAMS AND PLATE ASSEMBLAGES BASED ON THE IMPLICIT COROTATIONAL METHOD

GIOVANNI GARCEA, ANTONIO MADEO AND RAFFAELE CASCIARO

In our previous paper the implicit corotational method (ICM) was presented as a general procedure for recovering objective nonlinear models fully reusing the information obtained by the corresponding linear theories.

The present work deals with the implementation of the ICM as a numerical tool for the finite element analysis of nonlinear structures using either a path-following or an asymptotic approach. Different aspects of the FEM modeling are discussed in detail, including the numerical handling of finite rotations, interpolation strategies, and equation formats.

Two mixed finite elements are presented, suitable for nonlinear analysis: a three-dimensional beam element, based on interpolation of both the kinematic and static fields, and a rotation-free thin-plate element, based on a biquadratic spline interpolation of the displacement and piece-wise constant interpolation of stress. Both are frame invariant and free from nonlinear locking.

A numerical investigation has been performed, comparing beam and plate solutions in the case of thin-walled beams. The good agreement between the recovered results and the available theoretical solutions and/or numerical benchmarks clearly shows the correctness and robustness of the proposed approach as a general strategy for numerical implementations.

1. Introduction

In our previous paper [Garcea et al. 2012] we described a general methodology, called the implicit corotational method (ICM), able to build geometrically exact nonlinear structural models by exploiting the information gained from linear theories. It is essentially based on two main steps: the general solution provided by the linear theory is exploited to recover a description of the nonlinear stress and strain fields, as viewed by a corotational local observer moving with the material neighbor; then this description is transferred to a fixed global frame directly by using standard change-in-the-observer algebra. In this way a general procedure which can be implemented in a simple and automatic way in different contexts is derived. The recovered nonlinear models implicitly satisfy objectivity requirements (they are geometrically exact) and maintain all the details of the three-dimensional linear solutions, without any deterioration.

This paper has been developed within the national joint research project "Performance-based modeling and analysis of nonlinear structures," supported by the Italian Ministry of University Scientific and Technology Research (MIUR). We would like to thank all the participants in the project for their comments and suggestions. Special thanks are addressed to Giuseppe Zagari, for his help in setting up the computer codes and performing the numerical tests.

Keywords: geometrically exact beam and shell theories, corotational description, postbuckling analysis.

Since linear structural theories are widely available in the literature, it is easy to obtain a large number of possible nonlinear models suitable for use in FEM analysis. Three ICM models have been derived in [Garcea et al. 2012]: a three-dimensional beam nonlinear model based on Saint-Venant general rod theory and two plate/shell nonlinear models based on Mindlin–Reissner and Kirchhoff plate theories.

In this paper we deal with the FEM implementation and numerical validation of these models within different analysis strategies. We start by discussing, in Section 2, the two analysis contexts which have been investigated, a *path-following analysis*, according to Riks' incremental iterative strategy [Riks 1979], and an *asymptotic analysis*, according to the Koiter-like approach described in [Casciaro 2005]. The latter, because of its exacting requirements in terms of the geometrical coherence of the modeling, provides a rigorous check on the accuracy obtained with the ICM approach.

The general aspects of ICM implementation in FEM analysis will be examined in Section 2.1. We will also consider different choices in the element description (that is, Lagrangian or corotational description) and in the interpolation of its internal fields. Frame-independence plays an important role in element setup and the lack of it can result in spurious locking, which we called nonlinear interpolation locking in [Casciaro 2005] (also see [Salerno and Lanzo 1997]), which can significantly affect the numerical solution. The equation format (that is, mixed or compatible) also plays an important role in the convergence of the iterative solution processes and in the accuracy of the extrapolation results (see [Garcea et al. 1998; 1999]). These topics will be discussed and the use of mixed FEM interpolations and a mixed format is suggested.

Sections 4 and 5 will present and describe in detail two finite elements derived by the beam and Kirchhoff plate ICM models recovered in [Garcea et al. 2012], which appear suitable for the analysis of general three-dimensional assemblages. Both use a mixed format and a separate interpolation of the displacement and stress fields and are free from interpolation nonlinear locking. The beam element represents a three-dimensional extension of the interpolation described in [Salerno and Lanzo 1997]; the plate element is based on the biquadratic spline interpolation already used in [Lanzo et al. 1995; Lanzo and Garcea 1996; Casciaro et al. 1998; Garcea 2001]

The availability of analytical results or known reference benchmarks and the possibility of comparing, in the case of thin-walled beams, the results obtained by two different models (such as a one-dimensional beam or an assemblage of two-dimensional plates) allow, in Section 6, a detailed discussion about the performance of the proposed elements and their effectiveness in test cases of technical interest. Final comments and remarks are made in the concluding section.

2. Numerical strategies in nonlinear FEM analysis

In reviews of the numerical strategies used in nonlinear FEM analysis, Riks [1987; 2004] identified two main approaches: the *path-following* and *asymptotic* analyses. Both apply to a structure subjected to an assigned loading path $p[\lambda]$, usually in the form of a proportional loading $p := \lambda \hat{p}$, which is described by defining its potential energy in terms of a discrete set of parameters, all collected into a *configuration vector* $\boldsymbol{u}$, which controls both displacement and stress fields, d and σ, through the assumed FEM interpolation. According to [Garcea et al. 2012, Equations (1)–(4)], equilibrium implies the condition

$$\Pi' \delta u := \Phi'[u]\delta u - \lambda \hat{p}\, \delta u = 0, \quad u \in \mathcal{U}, \quad \delta u \in \mathcal{T}, \tag{1}$$

where $u := \{d, \sigma\}$, $\Phi[u]$ is the strain energy, $\lambda \hat{p} u$ the external work, and we denote by a prime Frechèt's differentiation. Applying FEM interpolation $u := \mathcal{L}\boldsymbol{u}$, $\mathcal{L}$ being the *interpolation operator*, (1) can be rewritten in the vectorial form

$$\boldsymbol{r}[\boldsymbol{u}, \lambda] := \boldsymbol{s}[\boldsymbol{u}] - \lambda \hat{\boldsymbol{p}} = \boldsymbol{0}, \tag{2}$$

with the *response vector* $\boldsymbol{s}[\boldsymbol{u}]$ and the *unitary load vector* $\hat{\boldsymbol{p}}$ being defined by the energy equivalencies

$$\boldsymbol{s}^T \delta \boldsymbol{u} = \Phi'[u]\delta u, \quad \hat{\boldsymbol{p}}^T \delta \boldsymbol{u} = \hat{p}\delta u, \quad \forall\, \delta \boldsymbol{u}. \tag{3}$$

We obtain a relationship between the configuration vector $\boldsymbol{u}$ and the load multiplier λ defining a curve (maybe composed of several separate branches) in $\{\boldsymbol{u}, \lambda\}$ space, usually called the *equilibrium path*. The aim of the analysis will be to obtain an accurate evaluation of its natural branch, that is, the branch coming from a known initial configuration $\boldsymbol{u}_0$, usually assumed as the one corresponding to $\lambda = 0$.

For reading convenience, we briefly summarize both the cited approaches here and refer interested readers to the specific literature for further details (for example, see [Riks 2004; Casciaro 2005] and references therein).

2.1. ***Path-following analysis.*** The basic idea in this approach is to recover the equilibrium path by determining a sequence of equilibrium points $\{\boldsymbol{u}^{(k)}, \lambda^{(k)}\}$ sufficiently near to allow the equilibrium curve to be obtained by interpolation. The analysis develops into a step-by-step process. In each step, a new point $\{\boldsymbol{u}^{(k+1)}, \lambda^{(k+1)}\}$ is determined, starting from a first evaluation $\{\boldsymbol{u}_1, \lambda_1\}$ generally obtained by an extrapolation of the previous step, by an iterative Newton-like scheme which provides a convergent sequence of estimates $\{\boldsymbol{u}_j, \lambda_j\}$, $j = 2, 3, \ldots$, so allowing us to reduce the equilibrium error $\boldsymbol{r}_j := \boldsymbol{r}[\boldsymbol{u}_j, \lambda_j]$ to within an acceptable tolerance.

Different schemes have been proposed in the literature to perform the iteration, but all of them appear as minor variations of the *arc-length scheme* originally proposed in [Riks 1979]. The main idea is that of coupling the equilibrium equation (2) with the further constraint

$$g[\boldsymbol{u}, \lambda] - \xi^{(k+1)} = 0, \tag{4a}$$

which defines a surface in $\{\boldsymbol{u}, \lambda\}$ space, so the required solution will correspond to the intersection of this surface with the equilibrium curve (2). Different variants of the method are obtained by different choices for the function $g[\boldsymbol{u}, \lambda]$.

The conditions for achieving a proper intersection between (2) and (4a) are extensively described in Riks' papers. The simplest choice, originally suggested by Riks, of using the orthogonal hyperplane

$$\boldsymbol{n}_u^T(\boldsymbol{u} - \boldsymbol{u}_1) + n_\lambda(\lambda - \lambda_1) = 0, \tag{4b}$$

where

$$\boldsymbol{n}_u := \boldsymbol{M}\big(\boldsymbol{u}_1 - \boldsymbol{u}^{(k)}\big), \quad \boldsymbol{n}_\lambda := \mu\big(\lambda_1 - \lambda^{(k)}\big), \tag{4c}$$

$\boldsymbol{M}$ and μ being some suitable metric factors, will be effective (see [Garcea et al. 2002] for a discussion of this topic).

Solution of the extended system (2)–(4b) can be obtained by a modified Newton–Raphson scheme:

$$\boldsymbol{u}_{j+1} = \boldsymbol{u}_j + \dot{\boldsymbol{u}}, \quad \lambda_{j+1} = \lambda_j + \dot{\lambda}, \tag{5a}$$

where by introducing matrix $\tilde{\boldsymbol{K}}$ as a suitable approximation for the Hessian of the strain energy $\Phi[\boldsymbol{u}]$:

$$\tilde{\boldsymbol{K}} \approx \boldsymbol{K}[\boldsymbol{u}_j] := \left[\frac{\partial \boldsymbol{s}[\boldsymbol{u}]}{\partial \boldsymbol{u}}\right]_{\boldsymbol{u}_j}, \tag{5b}$$

the iterative corrections $\dot{\boldsymbol{u}}$ and $\dot{\lambda}$ are defined by the linear system

$$\begin{bmatrix} \tilde{\boldsymbol{K}} & \hat{\boldsymbol{p}} \\ \boldsymbol{n}_u^T & n_\lambda \end{bmatrix} \begin{bmatrix} \dot{\boldsymbol{u}} \\ \dot{\lambda} \end{bmatrix} = - \begin{bmatrix} \boldsymbol{r}_j \\ 0 \end{bmatrix}, \tag{5c}$$

which is easily solved in partitioned form allowing us to exploit the symmetry and banded structure of matrix $\tilde{\boldsymbol{K}}$.

The arc-length scheme provides a simple way to overcome limit points because the extended system (5c) remains not singular even if the Hessian $\boldsymbol{K}$ becomes singular, which was a real difficulty before the paper [Riks 1979]. Its behavior is, however, strongly affected by the choice for the iteration matrix $\tilde{\boldsymbol{K}}$ which is usually assumed as the Hessian evaluated in correspondence to $\boldsymbol{u}^{(k)}$ (that is, at the beginning of the step) or to $\boldsymbol{u}_1$ (in the first extrapolation point). The convergence of the iterative process (5) has been widely discussed in [Garcea et al. 1998; Casciaro and Garcea 2002]. It is highly sensitive to the format of the equations, that is to the actual manner in which the equations are split and organized (also see [Garcea and Leonetti 2011; Bilotta et al. 2012]). Different formats behave very differently and, in particular, compatible formats expressed in displacement unknowns and equilibrium equations can lead to convergence failures as a consequence of locking (which we call *extrapolation locking* in [Garcea et al. 1998]) due to the interaction of large axial/flexural stiffness ratios with even small element rotations.

As regards the aim of the present paper, it is important to consider that path-following analysis only needs the response vector $\boldsymbol{s}[\boldsymbol{u}]$, that is, the first variation of the strain energy, to be evaluated accurately, being directly related to (2). Conversely, the same accuracy is not actually needed for the second variation of the energy which provides the Hessian matrix $\boldsymbol{K}[\boldsymbol{u}]$, because it is only used as a part of the iteration process and its accuracy only influences the convergence of the process. A fairly rough approximation is generally sufficient for that purpose.

2.2. ***The asymptotic analysis.*** Asymptotic analysis essentially corresponds to the implementation of Koiter's approach to nonlinear elastic stability [Koiter 1945; Budiansky 1974] into a FEM numerical context. While being less diffuse than path-following approaches within computational mechanics (maybe because of its high demands in terms of modeling accuracy) it has been described in detail in many papers (for example, [Casciaro et al. 1992; 1998; Flores and Godoy 1992; Lanzo et al. 1995; Pacoste and Eriksson 1995; Lanzo and Garcea 1996; Wu and Wang 1997; Poulsen and Damkilde 1998; Garcea et al. 1999; 2002; 2005; Garcea 2001; Boutyour et al. 2004; Casciaro 2005; Silvestre and Camoti 2005; Chen and Virgin 2006; Schafer and Graham-Brady 2006; Rahman and Jansen 2010] and references therein), so it only needs to be briefly summarized here.

The solution process is based on an expansion of the potential energy, in terms of load factor λ and modal amplitudes ξ_i, which is characterized by fourth-order accuracy. Following [Casciaro 2005], it can be summarized in this way:

(1) The *fundamental path* is obtained as a linear extrapolation

$$\boldsymbol{u}^f[\lambda] := \boldsymbol{u}_0 + \lambda \hat{\boldsymbol{u}}, \tag{6a}$$

where $\hat{\boldsymbol{u}}$ is the initial path tangent, obtained as the solution of the linear vectorial equation

$$\boldsymbol{K}_0\hat{\boldsymbol{u}} = \hat{\boldsymbol{p}}, \quad \boldsymbol{K}_0 := \boldsymbol{K}[\boldsymbol{u}_0]. \tag{6b}$$

(2) A cluster of *buckling loads* λ_i, $i = 1, \dots, m$, and associated *buckling modes* $\dot{\boldsymbol{v}}_i$ are obtained along $\boldsymbol{u}^f[\lambda]$, defined by the critical condition

$$\boldsymbol{K}[\lambda_i]\dot{\boldsymbol{v}}_i = \boldsymbol{0}, \quad \boldsymbol{K}[\lambda] := \boldsymbol{K}[\boldsymbol{u}_0 + \lambda\hat{\boldsymbol{u}}]. \tag{6c}$$

We will denote with $\mathcal{V} := \{\dot{\boldsymbol{v}} = \sum_{i=1}^{m} \xi_i \dot{\boldsymbol{v}}_i\}$ the subspace spanned by the buckling modes $\dot{\boldsymbol{v}}_i$ and with $\mathcal{W} := \{\boldsymbol{w} : \boldsymbol{w} \perp \dot{\boldsymbol{v}}_i, i = 1, \dots, m\}$ its orthogonal complement according the orthogonality condition

$$\boldsymbol{w} \perp \dot{\boldsymbol{v}}_i \;\Leftrightarrow\; \Phi_b'''\hat{u}\dot{v}_i w = 0, \tag{6d}$$

where $\hat{u} := \mathcal{L}\hat{\boldsymbol{u}}$, $\dot{v}_i := \mathcal{L}\dot{\boldsymbol{v}}_i$, and $w := \mathcal{L}\boldsymbol{w}$. We will also denote with λ_b an appropriate reference value for the cluster, for example, the smallest of λ_i or their mean value, and with a suffix "b" quantities evaluated in correspondence to $\boldsymbol{u}_b := \boldsymbol{u}^f[\lambda_b]$.

(3) Making $\xi_0 := (\lambda - \lambda_b)$ and $\dot{\boldsymbol{v}}_0 := \hat{\boldsymbol{u}}$, for more compact notation, the asymptotic approximation for the required path is defined by the expansion

$$\boldsymbol{u}[\lambda, \xi_k] := \boldsymbol{u}_b + \sum_{i=0}^{m} \xi_i \dot{\boldsymbol{v}}_i + \frac{1}{2}\sum_{i,j=0}^{m} \xi_i\xi_j \boldsymbol{w}_{ij}, \tag{6e}$$

where $\boldsymbol{w}_{ij} \in \mathcal{W}$ are quadratic corrections introduced to satisfy the projection of equilibrium equation (1) into $\mathcal{W}$ and obtained by the linear *orthogonal equations*

$$\delta\boldsymbol{w}^T(\boldsymbol{K}_b\boldsymbol{w}_{ij} + \boldsymbol{p}_{ij}) = 0, \quad \forall \boldsymbol{w} \in \mathcal{W}, \tag{6f}$$

where $\boldsymbol{K}_b := \boldsymbol{K}[\boldsymbol{u}^f[\lambda_b]]$ and vectors $\boldsymbol{p}_{ij}$ are defined as a function of modes $\dot{\boldsymbol{v}}_i$ and $i = 0, \dots, m$ by the energy equivalence

$$\delta\boldsymbol{w}^T\boldsymbol{p}_{ij} = \Phi_b'''\delta w \dot{v}_j \dot{v}_j.$$

(4) The following energy terms are computed for $i, j = 0, \dots, m$ and $k = 1, \dots, m$:

$$\begin{aligned} \mathcal{A}_{ijk} &= \Phi_b'''\dot{v}_i\dot{v}_j\dot{v}_k, & \mathcal{B}_{ijhk} &= \Phi_b''''\dot{v}_i\dot{v}_j\dot{v}_h\dot{v}_k - \Phi_b''(w_{ij}w_{hk} + w_{ih}w_{jk} + w_{ik}w_{jh}), \\ \mathcal{C}_{ik} &= \Phi_b''w_{00}w_{ik}, & \mu_k[\lambda] &= \tfrac{1}{2}\lambda_b\big(\lambda - \tfrac{1}{2}\lambda_b\big)\Phi_b'''\hat{u}^2\dot{v}_k + \tfrac{1}{6}\lambda_b^2(\lambda_b - 3\lambda)\Phi_b''''\hat{u}^3\dot{v}_k, \end{aligned} \tag{6g}$$

where the *implicit imperfection factors* μ_k are defined by the fourth-order expansion of the unbalanced work on the fundamental path (that is, $\mu_k[\lambda] := (\lambda\hat{p} - \Phi'[\lambda\hat{u}])\dot{v}_k$).

(5) The equilibrium path is obtained by projecting equilibrium equation (1) into $\mathcal{V}$. According to (6a)–(6g), we have

$$\frac{1}{2}\sum_{i,j=0}^{m} \xi_i\xi_j\mathcal{A}_{ijk} + \frac{1}{6}\sum_{i,j,h=0}^{m} \xi_i\xi_j\xi_h\mathcal{B}_{ijhk} + \mu_k[\lambda] - \lambda_b\Big(\lambda - \frac{1}{2}\lambda_b\Big)\sum_{i=0}^{m} \xi_i\mathcal{C}_{ik} = 0, \quad k = 1, \dots, m. \tag{6h}$$

The equation corresponds to an algebraic nonlinear system of m equations in the $m + 1$ variables $\xi_0, \xi_1, \dots, \xi_m$, with known coefficients.

Note that, from a computational point of view, the analysis develops into:

(i) Solve linear system (6a); this can easily be obtained by standard factorization of matrix $\boldsymbol{K}_0$.

(ii) Perform the buckling search (6b); this corresponds to a nonlinear eigenvalue problem which can be, however, easily solved, as described in [Casciaro et al. 1998], by an iterative scheme only requiring matrix $\boldsymbol{K}_0^{-1}$ be available in factorized form, as it already is from the previous step.

(iii) Solve orthogonal equations (6f); they correspond to a linear system where the right-hand vectors $\boldsymbol{p}_{ij}$ are obtained as a function of $\boldsymbol{v}_i$ by an element-by-element assembling process similar to that used for obtaining $\boldsymbol{s}[\boldsymbol{u}]$; as $\boldsymbol{K}_b \approx \boldsymbol{K}_0$ within the orthogonal space $\mathcal{W}$, its solution can be conveniently obtained, as described in [Casciaro et al. 1998], through a modified Newton-like iteration scheme exploiting $\boldsymbol{K}_0$ as an iteration matrix (see [Casciaro 2004] for further insights).

(iv) Compute factors $\mathcal{A}_{ijk}, \ldots, \mu_k[\lambda]$ through (6g); all of them are scalar quantities which can be easily obtained as integrals of known functions.

(v) Perform a path-following solution of (6h); because of the small dimensions of the system (of the order of tenths), this can be obtained very quickly using standard or even specialized variants of the arc-length scheme.

The actual implementation of the asymptotic approach as a computational tool is therefore quite easy and its total computational burden, which is mainly involved in the factorization of matrix $\boldsymbol{K}_0$, remains of the order of that required by a standard linearized stability analysis. It provides the initial postbuckling behavior of the structure, including *modal interactions* and *jumping-after-bifurcation* phenomena. Moreover, once the preprocessor phase of the analysis has been performed (Steps (1)–(4)), the presence of small loading imperfections or geometrical defects can be taken into account in the postprocessing phase (Step (5)), by adding some additional imperfection terms in the expression of $\mu_k[\lambda]$, with a negligible computational extra cost, so allowing an inexpensive imperfection sensitivity analysis (for example, see [Lanzo and Garcea 1996; Casciaro et al. 1998]). From (6h) we can also extract information about the worst imperfection shapes [Salerno and Casciaro 1997; Salerno and Uva 2006] we can use to improve the imperfection sensitivity analysis or for driving more detailed investigations through specialized path-following analysis (see [Casciaro 2005; Casciaro and Mancusi 2006] and references therein).

Note that asymptotic analysis can provide a very accurate recovery of the equilibrium path, as it derives from both numerical testing and theoretical investigation [Brezzi et al. 1986]. Conversely, it makes great use of information attained from a fourth-order expansion of the strain energy and then requires that a fourth-order accuracy be guaranteed in the structural modeling. Even small inaccuracies in this evaluation, deriving from geometrical incoherencies in the higher-order terms of the expansion of the $\varepsilon[d]$ law or in its finite element representation, significantly affect the accuracy of the solution and can make it unreliable. It is also very sensitive to the format used in the extrapolation, to avoid *extrapolation locking* (see [Garcea et al. 1999]), and the use of a mixed equation format is generally needed to obtain a robust implementation.

This high sensitivity of the asymptotic analysis to the accuracy in the nonlinear modeling actually represents an advantage for the purposes of the present paper because it provides a very sensitive context and appropriate benchmarks suitable for an in-depth testing of the accuracy of ICM models.

3. FEM implementation of nonlinear models

The ICM method [Garcea et al. 2012] allows the recovery of nonlinear models from information attained by the corresponding linear ones. It is particularly suitable for modeling fibred continua, such as beams and shells, and directly provides an objective expression for the mixed form of the potential energy:

$$\Pi := \int_\Omega \left\{ \boldsymbol{t}[s]^T \boldsymbol{\varrho}[\boldsymbol{d}[s]] - \tfrac{1}{2} \boldsymbol{t}[s]^T \boldsymbol{H}[s] \boldsymbol{t}[s] \right\} ds - \int_\Omega \boldsymbol{p}[s]^T \boldsymbol{d}[s] ds - \int_{\partial\Omega} \boldsymbol{f}[s]^T \boldsymbol{d}[s] ds, \tag{7}$$

where Ω is the fiber support domain; $\boldsymbol{t}$ are generalized strengths, $\boldsymbol{d}$ displacements, $\boldsymbol{p}$ interior loads, and $\boldsymbol{f}$ boundary loads, all associated with the fiber $\mathcal{S}[s]$; $\boldsymbol{H}$ is a compliance operator such that $\frac{1}{2}\boldsymbol{t}^T \boldsymbol{H} \boldsymbol{t}$ is the local contribution to the complementary energy; and s is a material abscissa varying in Ω. The ICM actually provides appropriate objective definitions for $\boldsymbol{t}[s]$, $\boldsymbol{d}[s]$, and $\boldsymbol{H}[s]$, as a generalization of quantities used in the corresponding linear modeling, and an explicit expression for the nonlinear displacement-to-strain relationship $\boldsymbol{\varrho}[\boldsymbol{d}[s]]$.

By partitioning the structure in finite elements and assuming in each of them both the internal fields $\boldsymbol{t}[s]$ and $\boldsymbol{d}[s]$ defined as functions of a discrete set of tensions and displacement element parameters $\boldsymbol{t}_e$ and $\boldsymbol{d}_e$,

$$\boldsymbol{t}[s] := \boldsymbol{t}[s, \boldsymbol{t}_e], \quad \boldsymbol{d}[s] := \boldsymbol{d}[s, \boldsymbol{d}_e], \tag{8}$$

expression (7) can be reduced to an algebraic form suitable for use in a numerical solution procedure.

3.1. ***Element interpolation in linear analysis.*** In linear analysis we usually assume a linear relationship

$$\boldsymbol{t}[s] := \boldsymbol{B}_t[s] \boldsymbol{t}_e, \quad \boldsymbol{d}[s] := \boldsymbol{B}_d[s] \boldsymbol{d}_e, \tag{9a}$$

with $\boldsymbol{B}_t[s]$ and $\boldsymbol{B}_d[s]$ collecting the interpolation shape functions. Due to the linear relationship between $\boldsymbol{d}[s]$ and $\boldsymbol{\varrho}[s]$, we also obtain a linear interpolation for the strain

$$\boldsymbol{\varrho}[s] = \boldsymbol{B}_\varepsilon[s] \boldsymbol{d}_e. \tag{9b}$$

As a consequence, performing integration, virtual works equation (1) can be rewritten in FEM format:

$$\sum_e \mathcal{A}_e \left(\begin{bmatrix} -\boldsymbol{H}_e & \boldsymbol{D}_e \\ \boldsymbol{D}_e^T & \cdot \end{bmatrix} \begin{bmatrix} \boldsymbol{t}_e \\ \boldsymbol{d}_e \end{bmatrix} - \begin{bmatrix} \cdot \\ \boldsymbol{p}_e \end{bmatrix} \right) = \boldsymbol{0}, \tag{10a}$$

where $\mathcal{A}_e$ is the standard FEM assemblage operator, summation is extended to all elements in the partition, and the element matrices $\boldsymbol{H}_e$ and $\boldsymbol{D}_e$ and vector $\boldsymbol{p}_e$ are defined by

$$\boldsymbol{H}_e := \int_e \boldsymbol{B}_t[s]^T \boldsymbol{H}[s] \boldsymbol{B}_t[s] ds, \quad \boldsymbol{D}_e := \int_e \boldsymbol{B}_t[s]^T \boldsymbol{B}_\varepsilon ds, \quad \boldsymbol{p}_e := \int_e \boldsymbol{B}_d[s]^T \boldsymbol{p}[s] ds. \tag{10b}$$

Stress and displacement interpolations can be set independently (we only need to satisfy the well-known Brezzi–Babuska condition [Babuška 1971; Brezzi 1974]); in this case we call this a *mixed interpolation*. Frequently they are related to each other by assuming

$$\boldsymbol{t}[s] = \boldsymbol{H}[s]^{-1} \boldsymbol{B}_\varepsilon[s] \boldsymbol{d}_e. \tag{11}$$

This choice, called *compatible interpolation*, implicitly satisfies the elastic laws $\boldsymbol{t}[s] = \boldsymbol{H}[s]^{-1}\boldsymbol{\rho}[s]$, so allowing (10a) to be further simplified into

$$\sum_e \mathscr{A}_e(\boldsymbol{K}_e\boldsymbol{d}_e - \boldsymbol{p}_e) = \boldsymbol{0}, \tag{12a}$$

where

$$\boldsymbol{K}_e := \int_e \boldsymbol{B}_\varepsilon[s]^T \boldsymbol{H}[s]^{-1}\boldsymbol{B}_\varepsilon[s]\,ds. \tag{12b}$$

Accuracy provided by this discretization process, in both its mixed and compatible versions, depends on an appropriate choice for the interpolation matrices $\boldsymbol{B}_t[s]$ and $\boldsymbol{B}_d[s]$ which have to reproduce as well as possible the expected solution, a locking being produced by inappropriate choices. However there is great experience in this field and a large number of interpolation functions are available in the literature, based on known properties of the expected solutions.

3.2. ***Element interpolation in nonlinear analysis.*** To transfer this experience from linear to nonlinear analysis is not straightforward. Even taking a linear relationship between the internal fields $\boldsymbol{t}[s]$ and $\boldsymbol{d}[s]$ and the external element parameters, as expressed by (9a), the expression for $\boldsymbol{\varrho}[\boldsymbol{s}]$ will become nonlinear:

$$\boldsymbol{\varrho}[\boldsymbol{s}] := \boldsymbol{\varrho}[s, \boldsymbol{d}_e], \tag{13}$$

because of the nonlinearity between $\boldsymbol{d}[\boldsymbol{s}]$ and $\boldsymbol{\varrho}[\boldsymbol{s}]$. This also implies (10a) will become nonlinear, that is,

$$\boldsymbol{r} := \sum_e \mathscr{A}_e\left(\begin{bmatrix} -\boldsymbol{H}_e\boldsymbol{t}_e + \boldsymbol{\varrho}_e[\boldsymbol{d}_e] \\ \boldsymbol{D}_e[\boldsymbol{d}_e]^T\boldsymbol{t}_e - \boldsymbol{p}_e \end{bmatrix}\right) = \boldsymbol{0}, \tag{14}$$

$\boldsymbol{\varrho}_e[\boldsymbol{d}_e]$ and $\boldsymbol{D}_e[\boldsymbol{d}_e]$ being defined by

$$\boldsymbol{\varrho}_e[\boldsymbol{d}_e] := \int_e \boldsymbol{B}_t[s]^T\boldsymbol{\varrho}[s, \boldsymbol{d}_e]\,ds, \quad \boldsymbol{D}_e[\boldsymbol{d}_e] := \int_e \boldsymbol{B}_t[s]^T\left[\frac{\partial\boldsymbol{\varrho}[s, \boldsymbol{d}_e]}{\partial\boldsymbol{d}_e}\right]ds, \tag{15}$$

and its solution requires the numerical strategies described in Section 2. Difficulties arise from the fact that slender elements, such as beams (or shells), generally have different behavior in the axial (or in-plane) direction than in transversal directions, the former being governed by the elongation of the element, the latter by its bending. As a consequence, the expected solution will be characterized by different shapes for the axial (in-plane) and transversal components of the displacements, which involves different requirements for the corresponding interpolation functions.

We can easily satisfy these requirements in linear analysis. For instance, by referring to the simple case of a planar beam element subjected to nodal loads, the standard interpolation, linear for the axial displacement, cubic for the transversal displacements, and quadratic for the rotations, could be appropriate in linear analysis. The same interpolation could hardly be applied in nonlinear analysis because of local changes in the orientation of the beam axis produced by the beam motion. In fact, due to finite element rotations, the two interpolations become coupled and, as a consequence of the high axial-to-transversal stiffness ratio, which is generally of some orders of magnitude, can produce a strong locking in the discretization. Moreover, in nonlinear analysis we have to be careful in using an appropriate representation for the rotations in order to assure full geometrical coherence in both the

internal description of the element and in the interelement continuity conditions. This can prove to be a difficult task when three-dimensional rotations are involved (see [Ritto-Corrêa and Camotim 2002] and references therein). As recalled in [Garcea et al. 2012, §3.1], rotations are characterized by a second-order orthogonal tensor $\boldsymbol{R} \in \mathcal{SO}(3)$ and combine with a product rule, so this is not easy to manage. To refer to its axial vector $\boldsymbol{\varphi} := \text{spin}(\boldsymbol{R})$, nonlinearly related to $\boldsymbol{R}$ through Rodrigues' formula (see (17)), could be a convenient choice, but this introduces a nonlinearity in the interpolation of translation components of the displacement when they are expressed in terms of rotational parameters and prevents its definition by a simple linear expression.

To avoid these inconveniences the interpolation law should assure frame invariance in the displacement representation and, moreover, interpolations for the translational and rotational components of the displacement should be separately defined. The use of a mixed interpolation could help in this because the components of $\boldsymbol{t}$ are aligned to the material and so they are frame-independent by definition. This makes it possible to express $\boldsymbol{t}[s]$ as a linear function of the discrete vector $\boldsymbol{t}_e$ when using a mixed interpolation. By appropriate choices for $\boldsymbol{B}_t[s]$ we can also filter out, in the virtual works expression $\int \boldsymbol{t}[s]^T \boldsymbol{\varrho}[s] ds$, undesirable aspects of the strain interpolation $\boldsymbol{B}_\varepsilon[s]$. All these possible advantages are lost when using compatible interpolations.

Several techniques can be used in the displacement interpolation to avoid locking, for instance: assuming the same shape functions for the three components of the translation (and/or the rotation) vector, as in the plate element used in [Lanzo et al. 1995; Lanzo and Garcea 1996]; assuming separate interpolations for rotations and translations, as in the beam element used in [Salerno and Lanzo 1997], and assuming a stress interpolation which renders matrix $\boldsymbol{D}_e$ independent of translation interpolation, as in [Garcea et al. 1998; 1999]; and filtering the rigid rotations of the element through an appropriate setting of the element reference frame.

All these devices will be implemented in the element formulations proposed in Sections 4 and 5.

3.3. ***Updated Lagrangian or corotational interpolation.*** A general way to obtain a frame-independent interpolation is to refer to an appropriate reference frame able to filter rigid rotations of the element. Two different strategies can be followed to achieve this objective: first, assuming a Lagrangian description but using an appropriate updating scheme to redefine the reference framing according to the current element alignment; second, using a corotational description, that is, assuming a reference frame which follows the element motion maintaining its alignment.

While being essentially different, the two descriptions use the same scheme, based on a standard change in the observer rule:

$$\bar{\boldsymbol{d}}_e := \boldsymbol{g}_e[\boldsymbol{d}_e], \tag{16a}$$

to translate the element displacement vector $\boldsymbol{d}_e$, referring to a global frame defined once and for all in the analysis, to its representation $\bar{\boldsymbol{d}}_e$ in the current element frame. They also use the same displacement interpolation in locally aligned components:

$$\bar{\boldsymbol{d}}[s] := \boldsymbol{B}_d[s] \bar{\boldsymbol{d}}_e. \tag{16b}$$

However, in the (updated) Lagrangian description, the element frame is assumed as fixed (while frequently updated), so (16a) states a linear relationship between $\boldsymbol{d}_e$ and $\bar{\boldsymbol{d}}_e$, that is,

$$\boldsymbol{g}_e[\boldsymbol{d}_e] := \boldsymbol{Q}_e[\boldsymbol{d}_e^R] \boldsymbol{d}_e, \tag{16c}$$

where $\boldsymbol{d}_e^R$ defines the reference configuration and matrix $\boldsymbol{Q}_e[\,\cdot\,]$ expresses the difference in alignment between the global and local frames. Conversely, in the corotational description, the element frame is assumed to move with the element and then the vectorial function $\boldsymbol{g}_e[\boldsymbol{d}_e] := \boldsymbol{Q}_e[\boldsymbol{d}_e]\boldsymbol{d}_e$ states a nonlinear relation between $\boldsymbol{d}_e$ and $\bar{\boldsymbol{d}}_e$.

Note that, while in the former case all nonlinearities of the problem are contained in the internal element description through functions $\boldsymbol{\varrho}_e[\bar{\boldsymbol{d}}_e]$ and $\boldsymbol{D}_e[\bar{\boldsymbol{d}}_e]$, in the latter case the internal description is decoupled from the external nonlinearities due to the finite rigid rotation of the element, which is taken into account by $\boldsymbol{g}_e[\boldsymbol{d}_e]$. As a consequence, in the corotational approach the need for an accurate modeling of the element could be somewhat relaxed. In fact, internal displacements, ruled by $\bar{\boldsymbol{d}}_e$, are only related to the element distortion and so, by mesh refinement, they can be made small enough to allow the use of the same interpolation laws derived from the linear analysis, without introducing noticeable interpolation locking. The smallness of $\bar{\boldsymbol{d}}_e$ also allows an evaluation of the strain/displacement relationships $\boldsymbol{\varrho}[\bar{\boldsymbol{d}}]$ through its Taylor expansion without noticeable loss in accuracy. A second-order, or even first-order, expansion can be sufficient with fine meshes. In this case, the element description will coincide, in the corotational framing, with that already used in the linear or the so-called second-order analysis, so allowing a direct reuse of standard software libraries widely available for these contexts. This is a great advantage, as pointed out in the pioneering paper [Rankin and Nour-Omid 1988], which is the reason for the diffusion of the corotational approach in the literature (see [M. and C. 2002; Chen et al. 2006; Alsafadie et al. 2010; 2011], to only cite recent proposals), but it is paid for by the need for some complex algebra to obtain derivatives of the nonlinear function $\boldsymbol{g}_e[\boldsymbol{d}_e]$ which are involved in the variations of the strain energy. These can be obtained in standard recursive form as shown in [Garcea et al. 2009], but in any case their derivation adds an extra cost to the analysis.

This extra cost and the need for an appropriate mesh refinement is the weak point of corotational approach. The Lagrangian approach does not have these disadvantages but, conversely, requires a full accurate modeling of the element: that is, it needs an appropriate choice for the structural model to be used in the discretization and a careful setting of interpolation laws. Geometrical coherence plays an important role in path-following and, even more, in asymptotic analysis, and we have to be very careful. The need for an appropriate modeling could be a serious drawback, in general, but the possibility of obtaining geometrically exact models through the ICM procedure described in [Garcea et al. 2012] allows us to eliminate the problem and makes particularly convenient the Lagrangian approach. The beam and shell elements proposed in Sections 4 and 5 are both based on a Lagrangian interpolation.

3.4. ***Mixed or compatible format.*** We know, from previous discussions, that a mixed interpolation can be really convenient in nonlinear analysis. Consider however that the assumption of a mixed or a compatible interpolation does not necessarily imply the use of a mixed or compatible format in the problem description as it might seem by (10) and (12). In fact, the two formats only differ in the writing of the system of equations in terms of the stress and displacement unknowns or the displacement unknowns alone. We can change from a mixed to a compatible format simply by expressing the stress variables in terms of the displacement unknowns or, conversely, change from a compatible format to a mixed one by splitting the system and explicitly introducing the stress unknowns and their relations to the displacement unknowns. The rewriting does not change the nature of the element, only the external format of its description.

Mixed and compatible formats, while completely equivalent in principle, behave very differently when implemented either in path-following or asymptotic solution strategies. This is an important, if frequently misunderstood, point in practical computations which has been widely discussed in [Garcea et al. 1998; 1999]. We refer readers to these papers and to the general discussion given in [Casciaro 2005] for more details, and only recall here that both numerical strategies described in Section 2 need the function $\boldsymbol{K}[\boldsymbol{u}]$ to be appropriately smooth in its controlling variables $\boldsymbol{u}$. In path-following analysis, its smoothness will imply having $\boldsymbol{K}[\boldsymbol{u}] \approx \tilde{\boldsymbol{K}} := \boldsymbol{K}[\boldsymbol{u}_0]$ when $\boldsymbol{u}$ moves in the neighborhood of $\boldsymbol{u}_0$ of interest, so allowing a fast convergence of the Newton iterative process. Analogously, the matrix $\boldsymbol{K}[\boldsymbol{u}]$ being the Hessian of the strain energy, its smoothness implies, in asymptotic analysis, that the higher-order energy term neglected in the fourth-order expansion (6h) be really irrelevant, so allowing an accurate recovery of the equilibrium path. We know that the smoothness of a nonlinear function strictly depends on the choice of the set of its control variables, that is, on the format of its description, and can change noticeably when referring to another, even corresponding, set. As a consequence, the mixed and compatible formats, even if referring to the same problem, can be characterized by a different smoothness and so behave differently in practice, when used within a numerical solution process. Actually, the compatible format is particularly sensitive to what we call *extrapolation locking* in [Garcea et al. 1998; 1999] which can produce a loss of convergence and then a premature arrest of the incremental process, when used in path-following analysis, or unacceptable errors in the path recovery, when used in asymptotic analysis. These inconveniences are easily avoided by changing to a mixed format.

4. A nonlinear beam element based on Saint-Venant general theory

A finite element for the three-dimensional nonlinear beam model, derived from Saint-Venant general rod theory through ICM (see [Garcea et al. 2012, §5]), will be described here. The model accounts for shear deformability and section warping due to the helicoid distortion due to torsion, that is, the so-called Wagner effect. A separate (mixed) interpolation is used for section strengths $\boldsymbol{t}[s]$ and displacements $\boldsymbol{d}[s]$, s being a material abscissa along the beam axis. The element has been implemented into a computer code, named `COBE` (see [Madeo 2008]), aimed at nonlinear analysis of three-dimensional beam assemblages using either asymptotic or the path-following strategies.

4.1. ***Some preliminaries on rotation algebra.*** Before entering into element definition we need to specify how rotation tensors are managed. In fact, we need to refer to a suitable parametrization which allows the configuration to be described in terms of variables belonging to a linear manifold as required by the formulation presented in Section 2, in order for the strain energy variations to be evaluated accurately through standard directional derivatives (see [Garcea et al. 2009]).

Finite three-dimensional rotations can be directly described in terms of a proper orthogonal tensor $\boldsymbol{R}$, that is a member of the nonlinear manifold SO(3). In matrix notation, the rotation tensor $\boldsymbol{R}$ becomes a 3×3 orthogonal matrix that, by exploiting the orthogonality property $\boldsymbol{R}^{-1} = \boldsymbol{R}^T$, is a function of only three parameters. A useful way to express $\boldsymbol{R}$ in terms of quantities lying in a linear manifold is that of [Rodrigues 1840]:

$$\boldsymbol{R}[\boldsymbol{\varphi}] = \boldsymbol{I} + \frac{\sin\varphi}{\varphi}\boldsymbol{W}[\boldsymbol{\varphi}] + \frac{(1-\cos\varphi)}{\varphi^2}\boldsymbol{W}^2[\boldsymbol{\varphi}], \tag{17}$$

which uses the rotation vector $\boldsymbol{\varphi} = [\varphi_1, \varphi_2, \varphi_3]^T$, $\varphi = \sqrt{\varphi_1^2 + \varphi_2^2 + \varphi_3^2}$ being its magnitude and $\boldsymbol{W}[\boldsymbol{\varphi}] := \mathrm{spin}(\boldsymbol{\varphi})$ the associated spin matrix. This representation uses a minimal set of parameters, is singularity free, and gives a one-to-one correspondence in the range $0 \le \varphi < 2\pi$ (see [Ritto-Corrêa and Camotim 2002]). Taking $\boldsymbol{\varphi} := \boldsymbol{\varphi}[s]$, it is also useful to introduce the operator

$$\boldsymbol{T}[\boldsymbol{\varphi}] := \boldsymbol{I} + \frac{1-\cos\varphi}{\varphi^2}\boldsymbol{W}[\boldsymbol{\varphi}] + \frac{\varphi - \sin\varphi}{\varphi^3}\boldsymbol{W}^2[\boldsymbol{\varphi}], \tag{18a}$$

which satisfies the following equivalence (a comma means partial derivative):

$$\boldsymbol{R}(\boldsymbol{\varphi})^T \boldsymbol{R}(\boldsymbol{\varphi})_{,s} = \mathrm{spin}(\boldsymbol{T}^T[\boldsymbol{\varphi}]\boldsymbol{\varphi}_{,s}). \tag{18b}$$

4.2. ***Handling the nonlinear beam model.*** By referring to the nonlinear beam model proposed in [Garcea et al. 2012, §5], we consider a beam element, initially straight and of length ℓ_e. The section strengths $\boldsymbol{t}$ and work-associated section strains $\boldsymbol{\varrho}$ are defined as

$$\boldsymbol{t} := \begin{bmatrix} \boldsymbol{N} \\ \boldsymbol{M} \end{bmatrix}, \quad \boldsymbol{\varrho} = \boldsymbol{\varrho}_L + \boldsymbol{\varrho}_Q, \tag{19a}$$

$\boldsymbol{N}$ and $\boldsymbol{M}$ being the vectors collecting the axial/shear strengths and torsional/bending couples and

$$\boldsymbol{\varrho}_L := \begin{bmatrix} \boldsymbol{\varepsilon}_L \\ \boldsymbol{\chi}_L \end{bmatrix}, \quad \boldsymbol{\varrho}_Q := \begin{bmatrix} \boldsymbol{\varepsilon}_Q[\boldsymbol{\varrho}_L] \\ \boldsymbol{\chi}_Q[\boldsymbol{\varrho}_L] \end{bmatrix}, \tag{19b}$$

where $\boldsymbol{\varepsilon}_L$ and $\boldsymbol{\chi}_L$ are given by

$$\boldsymbol{\varepsilon}_L := \boldsymbol{R}^T(\boldsymbol{v}_{,s} + \boldsymbol{e}_1) - \boldsymbol{e}_1, \quad \boldsymbol{\chi}_L := \boldsymbol{T}^T\boldsymbol{\varphi}_{,s}, \tag{19c}$$

as functions of translations $\boldsymbol{v}[s]$ and rotations $\boldsymbol{\varphi}[s]$ associated to a material abscissa s varying from 0 to ℓ_e, and $\boldsymbol{\varepsilon}_Q$ and $\boldsymbol{\varrho}_Q$ collect the linear and quadratic terms in the expression of $\boldsymbol{\varrho}$ defined by [Garcea et al. 2012, Equation (39)]. The modeling is completed by the compliance operator $\mathbf{H}$ defined in [Garcea et al. 2012, §5.1].

Note that a large part of the components of $\boldsymbol{\varrho}_Q$ could refer to numerically negligible effects and so it can be omitted in practical computations (see [Garcea et al. 2012, §5.2.3]). Also note that, when using an appropriate reference frame suitable to render $\boldsymbol{\varphi} \ll 1$ within the element and making $\boldsymbol{W} := \mathrm{spin}[\boldsymbol{\varphi}]$, we can replace the finite element expressions (17) and (18a) by their Taylor expansions,

$$\boldsymbol{R}[\boldsymbol{\varphi}] = \boldsymbol{I} + \boldsymbol{W} + \tfrac{1}{2}\boldsymbol{W}^2 + \tfrac{1}{6}\boldsymbol{W}^3 + \tfrac{1}{24}\boldsymbol{W}^4 + \ldots, \quad \boldsymbol{T}[\boldsymbol{\varphi}] = \boldsymbol{I} + \tfrac{1}{2}\boldsymbol{W} + \tfrac{1}{6}\boldsymbol{W}^2 + \tfrac{1}{24}\boldsymbol{W}^3 + \ldots. \tag{20}$$

4.3. ***Mixed finite beam element.*** The beam element description starts with the choice of the element reference frame $\boldsymbol{x}_e = \{x_1, x_2, x_3\}$, aligned to the element as will be detailed in the sequel. We denote with $\boldsymbol{R}[s]$ and $\boldsymbol{\varphi}[s]$ the rotation matrix and the corresponding rotation vector relating the alignment of the section $\mathcal{S}[s]$ to the element frame, and with $\boldsymbol{R}_e$ the rotation matrix relating $\boldsymbol{x}_e$ to the global frame $\boldsymbol{x}_G$ which refers to the overall beam assemblage.

Stress is defined by a linear interpolation for $\boldsymbol{M}[s] := \{M_1[s], M_2[s], M_3[s]\}$ while $\boldsymbol{N}[s] = \boldsymbol{N}_e := \{N_1, N_2, N_3\}$ is assumed as constant over the element. Displacement is defined by a quadratic interpolation for the rotation vector $\boldsymbol{\varphi}[s] = \{\varphi_1[s], \varphi_2[s], \varphi_3[s]\}$, and by a linked interpolation for the translation vector $\boldsymbol{v}[s] = \{v_1[s], v_2[s], v_3[s]\}$. As a consequence, the element behavior is controlled by nine stress

parameters $\{\boldsymbol{N}_e, \boldsymbol{M}_i, \boldsymbol{M}_j\}$ and by 15 displacement parameters $\{\boldsymbol{v}_i, \boldsymbol{v}_j, \boldsymbol{\varphi}_i, \boldsymbol{\varphi}_j, \boldsymbol{\varphi}_m\}$, where indexes i and j relate to quantities evaluated in the end-sections of the beam ($s = 0$ and $s = \ell_e$), and

$$\boldsymbol{\varphi}_m := \frac{1}{\ell_e} \int_0^{\ell_e} \boldsymbol{\varphi}[s]\, ds. \tag{21}$$

4.4. ***Setting of the element frame.*** It is convenient to set the element frame $\boldsymbol{x}_e$ such that $\boldsymbol{\varphi}[s]$ is small enough to allow expansions (20). Two different strategies can be used:

(1) assuming $\boldsymbol{x}_e$ as a corotational system moving with the element such that $\boldsymbol{\varphi}_m$ is identical to zero and

(2) assuming $\boldsymbol{x}_e$ as a fixed system but such that $\boldsymbol{\varphi}_m = \boldsymbol{0}$ in some near reference configuration.

The former choice allows the rigid rotations of the element to be accounted for implicitly and so is less demanding of the internal accuracy of the element. For this reason it was made, for instance, in [Garcea et al. 2009], even if it requires some extra algebra. The latter choice, corresponding to a Lagrangian description, is more convenient in the present context due to the use of geometrically exact elements, and will be used here. We can also make the reference configuration coincident with the current one, so satisfying the condition $\boldsymbol{\varphi}_m = \boldsymbol{0}$ exactly, through a simple reference updating scheme. In fact, starting from an initial estimate $\boldsymbol{R}_e^{(j)}$ of the element alignment, providing $\boldsymbol{\varphi}_m^{(j)} \neq 0$, we can obtain the updated evaluation $\boldsymbol{R}_e^{(j+1)}$ by the scheme

$$\boldsymbol{R}_e^{(j+1)} := \boldsymbol{R}^T[\boldsymbol{\varphi}_m^{(j)}]\boldsymbol{R}_e^{(j)}, \tag{22}$$

which provides $\boldsymbol{R}[\boldsymbol{\varphi}_m^{(j)}] = \boldsymbol{R}_e{}^{T(j)}\boldsymbol{R}_e{}^{(j+1)}$ and so, for $\boldsymbol{R}_e^{(j+1)}\boldsymbol{R}_e^{T(j)} = \boldsymbol{I}$ (that is, at convergence), $\boldsymbol{\varphi}_m^{(j)} = \boldsymbol{0}$. The previous updating can be directly coupled with the global iteration schemes used in the analysis, such as the arc-length iteration used in the path-following approach (see (5)) or the iterative eigenvalue search used in asymptotic analysis (see (6c)).

4.5. ***Stress interpolation.*** It is convenient to rearrange the element stress parameters in the *natural* format (see [Argyris et al. 1979])

$$\mathbf{t}_e := \begin{bmatrix} \boldsymbol{m}_r \\ \boldsymbol{m}_s \\ \boldsymbol{m}_e \end{bmatrix}, \quad \boldsymbol{m}_r := \boldsymbol{N}\ell, \quad \boldsymbol{m}_s := \boldsymbol{M}_j + \boldsymbol{M}_i, \quad \boldsymbol{m}_e := \boldsymbol{M}_j - \boldsymbol{M}_i; \tag{23a}$$

in this way the stress interpolation is defined as a function of the *element stress vector* $\mathbf{t}_e$:

$$\boldsymbol{N}[s] = \mathbf{B}_n[s]\mathbf{t}_e, \quad \boldsymbol{M}[s] = \mathbf{B}_m[s]\mathbf{t}_e, \tag{23b}$$

where

$$\mathbf{B}_n := \frac{1}{\ell_e}\begin{bmatrix} \boldsymbol{I} & \cdot & \cdot \end{bmatrix}, \quad \mathbf{B}_m := \frac{1}{2}\begin{bmatrix} \cdot & -\boldsymbol{I} & \zeta\boldsymbol{I} \end{bmatrix}, \tag{23c}$$

with $\zeta := 2s/\ell_e - 1$ being an adimensional abscissa varying from -1 to 1 along the beam axis, and $\boldsymbol{I}$ and " $\cdot$ " the $[3 \times 3]$ identity and zero matrices, respectively.

4.6. ***Displacement interpolation.*** The same natural format can be assumed for the displacements by rearranging the relevant element displacement parameters in the *element displacement vector*

$$\boldsymbol{d}_e := \begin{bmatrix} \boldsymbol{\phi}_r \\ \boldsymbol{\phi}_s \\ \boldsymbol{\phi}_e \\ \boldsymbol{\phi}_m \end{bmatrix}, \qquad \begin{aligned} \boldsymbol{\phi}_r &:= (\boldsymbol{v}_j - \boldsymbol{v}_i)/\ell_e, & \boldsymbol{\phi}_s &:= (\boldsymbol{\varphi}_j - \boldsymbol{\varphi}_i)/2, \\ \boldsymbol{\phi}_e &:= (\boldsymbol{\varphi}_j + \boldsymbol{\varphi}_i)/2 - \boldsymbol{\varphi}_m, & \boldsymbol{\phi}_m &:= \boldsymbol{\varphi}_m. \end{aligned} \tag{24a}$$

The interpolation law for the rotations will be defined by

$$\boldsymbol{\varphi}[\zeta] = \mathbf{B}_\varphi[\zeta]\,\mathbf{d}_e, \quad \mathbf{B}_\varphi := \left[\,\cdot\,, \zeta\boldsymbol{I}, \left(\tfrac{3}{2}\zeta^2 - \tfrac{1}{2}\right)\boldsymbol{I}, \boldsymbol{I}\right]. \tag{24b}$$

The interpolation for translations will be assumed as linked to that of the rotations, according to the following rule:

$$\boldsymbol{\gamma} := \boldsymbol{v}_{,s}\,[\zeta] - \mathrm{spin}(\boldsymbol{\varphi}[\zeta])\boldsymbol{e}_1 = \mathrm{const}. \tag{24c}$$

4.7. ***Expression for the complementary energy.*** The element contribution to the complementary energy will be expressed in the form

$$\Psi_e := \frac{1}{2}\int_e \boldsymbol{t}[s]^T \boldsymbol{H}\boldsymbol{t}[s]\,ds = \frac{1}{2}\mathbf{t}_e^T \mathbf{H}_e \mathbf{t}_e. \tag{25a}$$

Substituting stress interpolation (23) into (10b), we obtain an explicit expression for the compliance element matrix $\mathbf{H}_e$:

$$\mathbf{H}_e := \frac{1}{12\ell_e}\begin{bmatrix} 12\boldsymbol{H}_{nn} & -6\ell_e\boldsymbol{H}_{nm} & \cdot \\ -6\ell_e\boldsymbol{H}_{nm}^T & 3\ell_e^2\boldsymbol{H}_{mm} & \cdot \\ \cdot & \cdot & \ell_e^2\boldsymbol{H}_{mm} \end{bmatrix}. \tag{25b}$$

4.8. ***Expression for the strain work.*** The element contribution to the strain work will be expressed in the form

$$^{\circ}\mathcal{W}_e := \int_e \boldsymbol{t}[s]^T(\boldsymbol{\varrho}_L[s] + \boldsymbol{\varrho}_Q[s])\,ds = \mathbf{t}_e^T(\boldsymbol{\rho}_{eL} + \boldsymbol{\rho}_{eQ}), \tag{26a}$$

where $\boldsymbol{\varrho}_L$ and $\boldsymbol{\varrho}_Q$ are defined in (19) and $\boldsymbol{\rho}_{eL}$ and $\boldsymbol{\rho}_{eQ}$ can be split as

$$\boldsymbol{\rho}_{eL} = \{\boldsymbol{\varrho}_{Lr}, \boldsymbol{\varrho}_{Ls}, \boldsymbol{\varrho}_{Le}\}, \quad \boldsymbol{\rho}_{eQ} = \{\boldsymbol{\varrho}_{Qr}, \boldsymbol{\varrho}_{Qs}, \boldsymbol{\varrho}_{Qe}\}. \tag{26b}$$

Exploiting (19c), (20), (23b), and (24b) we obtain

$$\begin{aligned} \boldsymbol{\varrho}_{Lr} &= \frac{1}{2}\int_{-1}^{1}\left\{\boldsymbol{\gamma} - \boldsymbol{W}\left(\boldsymbol{\gamma} + \frac{1}{2}\boldsymbol{w}\right) + \frac{1}{2}\boldsymbol{W}^2\left(\boldsymbol{\gamma} + \frac{2}{3}\boldsymbol{w}\right) - \frac{1}{6}\boldsymbol{W}^3\left(\boldsymbol{\gamma} + \frac{3}{4}\boldsymbol{w}\right) + \dots\right\}d\zeta, \\ \boldsymbol{\varrho}_{Ls} &= -\int_{-1}^{1}\left\{\left(\boldsymbol{I} - \frac{1}{2}\boldsymbol{W} + \frac{1}{6}\boldsymbol{W}^2 - \frac{1}{24}\boldsymbol{W}^3 + \dots\right)(\boldsymbol{\phi}_s + 3\zeta\boldsymbol{\phi}_e)\right\}d\zeta, \\ \boldsymbol{\varrho}_{Le} &= \int_{-1}^{1}\left\{\left(\boldsymbol{I} - \frac{1}{2}\boldsymbol{W} + \frac{1}{6}\boldsymbol{W}^2 - \frac{1}{24}\boldsymbol{W}^3 + \dots\right)\zeta(\boldsymbol{\phi}_s + 3\zeta\boldsymbol{\phi}_e)\right\}d\zeta, \end{aligned} \tag{26c}$$

where $\boldsymbol{W} := \mathrm{spin}(\boldsymbol{\varphi}[s])$ and $\boldsymbol{w} := \boldsymbol{W}\boldsymbol{e}_1$, that is,

$$\boldsymbol{W} := \boldsymbol{W}_m + \zeta\boldsymbol{W}_s + \left(\tfrac{3}{2}\zeta^2 - \tfrac{1}{2}\right)\boldsymbol{W}_e, \quad \boldsymbol{w} := \boldsymbol{w}_m + \zeta\boldsymbol{w}_s + \left(\tfrac{3}{2}\zeta^2 - \tfrac{1}{2}\right)\boldsymbol{w}_e, \tag{26d}$$

with $\boldsymbol{W}_\beta := \text{spin}(\boldsymbol{\phi}_\beta)$, $\boldsymbol{w}_\beta := \boldsymbol{W}_\beta \boldsymbol{e}_1$, and $\beta = m, s, e$. Constant $\boldsymbol{\gamma}$, defined by (24c), is obtained by integrating over the element:

$$\boldsymbol{\gamma} = \boldsymbol{\phi}_r - \boldsymbol{w}_m. \tag{26e}$$

In a similar fashion it is possible to obtain $\boldsymbol{\varrho}_Q$; its complex expression is not reported here, it being more simple and effective to derive it directly using algebraic manipulators.

4.9. ***Energy variations.*** By combining (25) and (26) we obtain an explicit form for the total strain energy of the element:

$$\Phi_e := \mathcal{W}_e - \Psi_e. \tag{27a}$$

Starting from this expression all energy variations needed by the analysis can be derived by standard algebra. These details, which are easily derived using algebraic manipulators, can be skipped here, and we only recall, as an example for the reader, the expression for the second variation, which is used for defining the tangent stiffness matrix of the element in the mixed format in the simple case where $\boldsymbol{\varrho}_Q$ is neglected.

Assuming that the reference configuration is straight ($\boldsymbol{\varphi}_r = \boldsymbol{\varphi}_s = \boldsymbol{\varphi}_e = \boldsymbol{0}$), we obtain

$$\Phi_e'' \dot{u}^2 = \begin{bmatrix} \dot{\mathbf{t}}_e \\ \dot{\mathbf{d}}_e \end{bmatrix}^T \begin{bmatrix} \mathbf{H}_e & \mathbf{D}_e \\ \mathbf{D}_e^T & \mathbf{G}_e \end{bmatrix} \begin{bmatrix} \dot{\mathbf{t}}_e \\ \dot{\mathbf{d}}_e \end{bmatrix}, \tag{27b}$$

where $\mathbf{H}_e$ is given directly by (25b), and matrices $\mathbf{D}_e$ and $\mathbf{G}_e$ are defined by

$$\mathbf{D}_e := \begin{bmatrix} \boldsymbol{I} & \boldsymbol{0} & \boldsymbol{0} & \text{spin}(\boldsymbol{e}_1) \\ \boldsymbol{0} & -\boldsymbol{I} & \boldsymbol{0} & \boldsymbol{0} \\ \boldsymbol{0} & \boldsymbol{0} & \boldsymbol{I} & \boldsymbol{0} \end{bmatrix}, \quad \mathbf{G}_e := \begin{bmatrix} \boldsymbol{0} & \boldsymbol{0} & \boldsymbol{0} & -\boldsymbol{G}_r \\ \boldsymbol{0} & \frac{1}{3}\boldsymbol{G}_m & -\frac{1}{2}\boldsymbol{G}_s & \frac{1}{2}\boldsymbol{G}_s \\ \boldsymbol{0} & -\frac{1}{2}\boldsymbol{G}_s & \frac{1}{5}\boldsymbol{G}_m & -\frac{1}{2}\boldsymbol{G}_e \\ -\boldsymbol{G}_r & \frac{1}{2}\boldsymbol{G}_s & -\frac{1}{2}\boldsymbol{G}_e & -\boldsymbol{G}_m \end{bmatrix}, \tag{27c}$$

where

$$\begin{aligned} &\boldsymbol{G}_r := \text{spin}(\boldsymbol{m}_r), \quad \boldsymbol{G}_s := \text{spin}(\boldsymbol{m}_s), \quad \boldsymbol{G}_e := \text{spin}(\boldsymbol{m}_e), \\ &\boldsymbol{G}_m := (\boldsymbol{I} - \boldsymbol{e}_1 \boldsymbol{e}_1^T) m_{r1} + \tfrac{1}{2}\,\text{spin}(\{0, -m_{r3}, m_{r2}\}). \end{aligned} \tag{27d}$$

4.10. ***Global handling of the beam assemblage.*** The element vectors $\mathbf{t}_e$ and $\mathbf{d}_e$ are related to the global vectors $\mathbf{t}_G$ and $\mathbf{d}_G$, collecting all kinematical and static degrees of freedom of the overall assemblage, that is, the displacements $\boldsymbol{u}_G$ and rotations $\boldsymbol{\varphi}_G$ in all its nodes, and the average rotations $\boldsymbol{\varphi}_{mG}$ and the stresses $\boldsymbol{N}_e$, $\boldsymbol{M}_i$, and $\boldsymbol{M}_j$ in all its beams. A linear relationship

$$\begin{bmatrix} \mathbf{t}_e \\ \mathbf{d}_e \end{bmatrix} = \mathbf{A}_e \mathbf{d}_G$$

is assumed where matrix $\mathbf{A}_e$ accounts for the different ordering of variables between the two vectors and for the rotations $\boldsymbol{R}_e$ of the element frames with respect to the global frame. In this way we can obtain the relevant matrix, vector, and scalar quantities required by the analysis by a standard assemblage as devised in Section 2.1.

4.11. ***Further remarks.*** The beam element described here has been built from the interpolation laws (23) and (24). This is one of the simplest choices we could make in order to account for the expected solution. It recovers the exact solution for the linear modeling in the case of a straight reference configuration and zero distributed loads, so it can provide satisfactory accuracy even if using a rough mesh refinement. A better element could be obtained by using higher-order interpolation functions or by referring to specialized interpolation rules able to recover more accurately the main aspects of the nonlinear solution. To refer to the linearized solution, for example, as in [Garcea et al. 1999] for planar beams, could mean a noticeable improvement in the element accuracy and allow rougher meshes. An investigation in this direction, which is outside the scope of the present paper, could be of interest.

5. A nonlinear plate element based on Kirchhoff theory

A plate element, based on the nonlinear thin-plate model recovered in [Garcea et al. 2012, §6.6], will be described here. The element has been introduced in the already available code KASP (see [Garcea 2001; Garcea et al. 2002]) aimed at the postbuckling analysis of plate assemblages using either the asymptotic or path-following approaches, according to the solution strategies described in Section 2.

The previous version of the code was based on a mixed version of the well-known von Kármán–Marguerre nonlinear plate model, enriched with the appropriate quadratic kinematical terms related to the in-plane rotations, as described in [Lanzo et al. 1995; Lanzo and Garcea 1996]. This modeling only guarantees second-order accuracy in satisfying frame independence requirements. However, even if exact objectivity is an essential prerequisite in nonlinear analysis, in particular when using an asymptotic approach, the error produced by the code little affects a correct evaluation of the critical and postcritical structural behavior in all the numerical tests referred to in the cited papers. In fact, in most cases examined, the postbuckling behavior was dominated by the strong postbuckling stress redistribution, so making the effects of the objectivity errors quantitatively irrelevant.

As also confirmed in successive papers [Garcea 2001; Garcea et al. 2002] this behavior is typical of box structures built with plate panels, especially when local buckling occurs, but stress redistribution reduces noticeably when modeling slender thin-walled beams as plate assemblages, because of the presence of large global rotations with minimal local distortions. So the use of full objective structural models is needed in these cases and should always be used to assure the general robustness of the code.

5.1. ***Handling the nonlinear thin-plate model.*** Denoting with $\boldsymbol{s} := \{X_1, X_2\}$ an in-plane material abscissa, stress and strain in the plate models are characterized by the local strengths $\mathbf{t}[\boldsymbol{s}] := \{\boldsymbol{N}[\boldsymbol{s}], \boldsymbol{M}[\boldsymbol{s}]\}^T$, where $\boldsymbol{N} := \{N_1, N_2, N_{12}\}$ and $\boldsymbol{M} := \{M_1, M_2, M_{12}\}$ collect the membranal strengths and bending couples, respectively, while the work-conjugate strain $\boldsymbol{\varrho}[\boldsymbol{s}] := \{\boldsymbol{\varepsilon}[\boldsymbol{s}], \boldsymbol{\chi}[\boldsymbol{s}]\}$ is defined in compact form by [Garcea et al. 2012, Equation (54)]. Expanding the products, we obtain

$$\boldsymbol{\varepsilon} = \begin{Bmatrix} u_{,1} + \frac{1}{2}(u_{,1}^2 + v_{,1}^2 + w_{,1}^2) \\ v_{,2} + \frac{1}{2}(u_{,2}^2 + v_{,2}^2 + w_{,2}^2) \\ u_{,2} + v_{,1} + (u_{,1}\, u_{,2} + v_{,1}\, v_{,2} + w_{,1}\, w_{,2}), \end{Bmatrix}, \tag{28a}$$

$$\boldsymbol{\chi} = \left\{ \begin{array}{l} w,_{11} + (w,_{11}\, u,_1 - u,_{11}\, w,_1 - v,_{11}\, w,_2 + w,_{11}\, v,_2) + (u,_2\, v,_{11}\, w,_1 \\ \quad + u,_1\, w,_{11}\, v,_2 - v,_2\, u,_{11}\, w,_1 - u,_1\, v,_{11}\, w,_2 - u,_2\, w,_{11}\, v,_1 + v,_1\, u,_{11}\, w,_2) \\ \\ w,_{22} + (w,_{22}\, u,_1 - u,_{22}\, w,_1 - v,_{22}\, w,_2 + w,_{22}\, v,_2) + (u,_2\, v,_{22}\, w,_1 \\ \quad + u,_1\, w,_{22}\, v,_2 - v,_2\, u,_{22}\, w,_1 - u,_1\, v,_{22}\, w,_2 - u,_2\, w,_{22}\, v,_1 + v,_1\, u,_{22}\, w,_2) \\ \\ w,_{12} + (w,_{12}\, u,_1 - u,_{12}\, w,_1 - v,_{12}\, w,_2 + w,_{12}\, v,_2) + (u,_2\, v,_{12}\, w,_1 \\ \quad + u,_1\, w,_{12}\, v,_2 - v,_2\, u,_{12}\, w,_1 - u,_1\, v,_{12}\, w,_2 - u,_2\, w,_{12}\, v,_1 + v,_1\, u,_{12}\, w,_2) \end{array} \right\}, \tag{28b}$$

$u[s]$, $v[s]$, and $w[s]$ being the components of the average displacement (translation) $\boldsymbol{d}[s]$ of the transversal fiber, according to a fixed frame $\boldsymbol{x}_e := \{x_1, x_2, x_3\}$ aligned to the element. Expressions (28) are frame invariant, so the actual choice for this frame is irrelevant for their accuracy, even if it is convenient to refer to the local average alignment of the plate and make x_3 orthogonal to its average plane, for practical reasons. It is worth noting that the Kirchhoff assumption of zero shear deformation allows the rotation parameters to be taken away from the kinematical description, so the nonlinear model is expressed in terms of the displacement fields alone, avoiding the use of a rotation algebra. Also note that the membranal strain $\boldsymbol{\varepsilon}$ coincides with that of the Green–Lagrange strain tensor, while the curvature $\boldsymbol{\chi}$ takes a complex expression with respect to the linear approximation assumed in the classical von Kármán–Marguerre theory. The difference lies in the addition of some quadratic and cubic extra terms which take into account pointwise differences in the orientations between the local normal to the middle surface and the x_3 axis. The modeling is completed by the compliance operator

$$\mathbf{H} := \begin{bmatrix} \mathbf{C}_n & \cdot \\ \cdot & \mathbf{C}_m \end{bmatrix}, \tag{28c}$$

$\mathbf{C}_n$ and $\mathbf{C}_m$ being defined by [Garcea et al. 2012, Equation (51b)].

It is worth mentioning that both the two approximate models, previously implemented in KASP, were based on the same modeling while a linear approximation was used for the curvatures. Membranal strains were defined by the complete quadratic expression (28a) in what we called the *complete Lagrangian* (LC) model and by a simplified expression, which only maintains quadratic terms in w, in the *simplified Lagrangian* (LS) model. The LS version is characterized by better flexural behavior, so it was the standard option in KASP.

5.2. ***Mixed-plate finite element.*** The discrete model is based on the high-continuity (HC) finite element interpolation proposed in [Aristodemo 1985], which has also been used in the initial version of KASP. The element was one of the first proposals in the spline interpolation approach (see [Hughes et al. 2005]), and it is very convenient in nonlinear plate analysis. We do not include details of this interpolation, which the reader can find in [Garcea 2001; Garcea et al. 2002] and only recall here that its main advantage is that of assuring interelement continuity for both displacement components and their derivatives, with a minimal use of displacement parameters (approximately three kinematical degrees of freedom per element) and without needing rotational degrees of freedom.

As already done in KASP, a $[2\times2]$ Gauss scheme has been used to integrate all the energy terms required by the analysis. Letting $\boldsymbol{s}^g$ be the position of the Gauss point g within the element e and denoting, from now on, with the index g quantities evaluated at point g, the strain energy can be evaluated by Gauss integrations as

$$\Phi_e := \sum_g (\mathcal{W}_g - \Psi_g), \tag{29a}$$

where

$$\mathcal{W}_g := \mathbf{t}_g^T \boldsymbol{\varrho}_g A_g, \quad \Psi_g := \tfrac{1}{2}\mathbf{t}_g^T \mathbf{H}_g \mathbf{t}_g A_g, \tag{29b}$$

$\mathbf{H}_g$ being defined by (28c), $A_g := \frac{1}{4}\ell_1\ell_2$ the area pertaining to point g, the Gauss strain $\boldsymbol{\varrho}_g[\mathbf{d}_e] := \{\boldsymbol{\varepsilon}_g, \boldsymbol{\chi}_g\}$ obtained by (28a) and (28b) making $\boldsymbol{s} = \boldsymbol{s}_g$, and the Gauss point stress $\mathbf{t}_g := \{\boldsymbol{N}_g, \boldsymbol{M}_g\}$ defined by

$$\boldsymbol{N}_g = \begin{bmatrix} N_{g11} \\ N_{g22} \\ N_{g12} \end{bmatrix}, \quad \boldsymbol{M}_g = \begin{bmatrix} M_{g11} \\ M_{g22} \\ M_{g12} \end{bmatrix}, \tag{29c}$$

where $N_{g11}, N_{g22}, \ldots, M_{g12}$ are directly assumed as element parameters controlling the stress interpolation within a mixed format.

This simple integration scheme is generally sufficient for our purpose. Note that, even if more sophisticated interpolations could also be used, this choice provides an exact correspondence with the results obtained in [Lanzo and Garcea 1996; Garcea 2001; Garcea et al. 2002] by allowing attention to be focused on the difference due to the use of a more accurate structural plate model without introducing any disturbing discretization improvement.

The energy variations needed by the analysis can be derived from (29) by standard algebra and assemblage procedures. Explicit expressions, similar to those already given in [Garcea 2001], are simply obtained through the use of algebraic manipulators, so details are not included here.

6. Numerical validation

The numerical results are mainly related to the asymptotic analysis, this context being more sensitive to the correctness of both the structural model and its finite element implementation. The results of path-following analysis are based on the same modeling and discretization, while using the corotational updating strategies described in [Garcea 2001; Garcea et al. 2009], so they can be considered very accurate and are used, essentially as a reference to check the accuracy and robustness of the asymptotic results. In all the numerical tests comparisons are performed with results obtained by other authors and/or with analytical solutions, when available.

The proposed three-dimensional beam finite element, implemented into a FEM code named COBE [Madeo 2008], has been tested for compact and general thin-walled cross sections. In all cases the evaluation of the compliance operator $\boldsymbol{H}_e$ has been obtained through the solution of the Saint-Venant equations using the FEM approach described in [Petrolo and Casciaro 2004] to which the reader is referred for further details (see also [Lacarbonara and Paolone 2007]). The proposed Kirchhoff plate element has been implemented in the KASP code [Garcea 2001]. In this way, it was easy to compare the results provided by the proposed plate model (denoted as ICM) with those obtained, for the same finite element discretization, using the complete Lagrangian (LC) and simplified Lagrangian (LS) approximate plate models already implemented in the code. Thin-walled beams can be modeled as Saint-Venant rods but also as assemblages of thin plates. This allowed further comparisons between the results provided by the two different models and so made it possible to obtain an independent check on their robustness. The comparison also allows us to emphasize the effects of the Saint-Venant simplifying hypotheses on the boundary conditions and cross-section distortions, in some relevant cases.

The section is organized as follows: First we present some simple tests, with known analytical solutions, showing the improvement in accuracy provided by ICM modeling with respect to the LC and LS models. We then present some tests to show the role played by postbuckling stress redistribution in reducing the accuracy demand in the plate modeling. Next, we present some tests to compare the results obtained for thin-walled structures modeled as beams or as three-dimensional plate assemblages, to show the general accuracy of the beam model recovered by the ICM, as well as its possible shortcomings in the presence of relevant boundary disturbances, local buckling, and in-plane section distortions. Finally, we report some tests referring to multimodal coupled buckling phenomena to show the real effectiveness of the proposed approach in general contexts and complex structural problems.

In the monomodal buckling tests, to compare the accuracy with known solutions, the following quantities, defining the postcritical tangent and curvature to the bifurcated path, have been introduced:

$$\dot{\lambda}_b = -\frac{1}{2}\frac{A_{111}}{A_{011}}, \qquad \ddot{\lambda}_b = -\frac{B_{1111} + 3\dot{\lambda}_b B_{0111} + 3\dot{\lambda}_b^2 B_{0011}}{3A_{011}}.$$

6.1. ***Accuracy of ICM models.*** This numerical investigation focuses on the accuracy of the proposed plate model in contexts where analytical results are available, that is, the simply supported Euler beam and the Roorda frame shown in Figures 1 and 2, respectively.

Despite their simplicity, when analyzed with an asymptotic approach, both problems are taxing with regard to the accuracy of the structural model and its FEM discretization. In fact, in both cases the buckling is not followed by a significant stress redistribution, and in order to obtain the correct postbuckling results the modeling has to assure full objectivity and be free, in its FEM implementation, from both interpolation and extrapolation locking phenomena [Garcea et al. 1999; Salerno and Lanzo 1997]. The two tests have been analyzed using either the beam or the plate modeling and, in the case of the plate modeling, referring to either an in-plane or an out-of-plane buckling. The results are compared with known analytical solutions and with the ones obtained using the approximate LC and LS plate models also implemented in KASP. An independent analysis has also been made using the commercial code ABAQUS [Hibbitt et al. 2007] to investigate the convergence behavior of the proposed elements. In all cases the ICM-beam path-following results are assumed as reference values.

6.1.1. *Euler beam.* The test refers to the Euler beam shown in Figure 1. The resulting paths are drawn in Figure 3 and show a good agreement with those provided by path-following analysis. The values for the buckling load λ_b and the postcritical curvature $\ddot{\lambda}_b$, obtained by identifying the expansion parameter ξ as the end-section rotation of the beam, are reported in Tables 1 and 2, for different discretization meshes.

Note that both the ICM models recover the analytical solution [Salerno and Lanzo 1997] $\lambda_b = \pi^2$ and $\ddot{\lambda}/\lambda_b = 0.25$ for sufficiently fine grids exactly. The LC and LS models provide correct answers for the buckling load, but have different postbuckling behavior in the in-plane and out-of-plane analysis: the LC

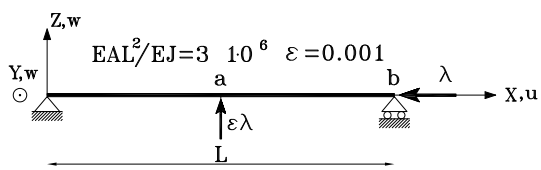

Figure 1. Euler beam.

Plate analysis	elements	Out-plane buckling ICM	S4-R	S8-R	In-plane buckling ICM	S4-R	S8-R
λ_b	16	9.901	9.933	9.868	9.918	33.380	9.868
	32	9.877	9.885	9.868	9.870	14.964	9.867
	64	9.872	9.873	9.868	9.870	10.326	9.867
$\ddot{\lambda}_b/\lambda_b$	16	0.290	·	·	0.332	·	·
	32	0.250	·	·	0.252	·	·
	64	0.250	·	·	0.250	·	·

Table 1. Euler beam: plate element convergence.

agrees perfectly with the exact solution in the in-plane case, whereas the LS provides the wrong result $\ddot{\lambda}/\lambda_b = 2$, eight times greater; conversely, the LS behaves better in the out-of-plane case, by providing the approximation $\ddot{\lambda}_b/\lambda_b = 0$, while the LC gives a completely erroneous unstable postbuckling curvature $\ddot{\lambda}/\lambda_b = -0.75$. So the LS model could be viewed as a better compromise than the LC, considering the importance of flexural buckling in the slender plates (see also [Lanzo et al. 1995]). Note also, from the results reported in Table 1, the good convergence behavior, in recovering the buckling load, of both the proposed beam and plate elements in comparison with the ones used in ABAQUS (three-node beam element, S4-R, and S8-R plate elements). The improvement in convergence is apparent considering the larger number of variables implied by the ABAQUS meshes: generally more than double in the case of the beam elements while about two to six times greater in the cases of the S4-R and S8-R plate elements.

6.1.2. *Roorda frame.* The test refers to the simple frame shown in Figure 2, first investigated by Roorda. An analytical solution for this problem can be found in [Bazant and L. 1991], by obtaining $\lambda_b = 13.89$, $\dot{\lambda}_b/\lambda_b = 0.3805$, and $\ddot{\lambda}_b/\lambda_b = 0.7576$ by reference to the choice $\xi := \varphi_b$ for the expansion parameter. These values are recovered exactly by both the ICM models for sufficiently fine meshes (the plate models are analyzed in out-of-plane conditions). The buckling load λ_b and the postbuckling slope $\dot{\lambda}_b$ are also recovered by the approximate models LC and LS, which, however, provide unsatisfactory results for the

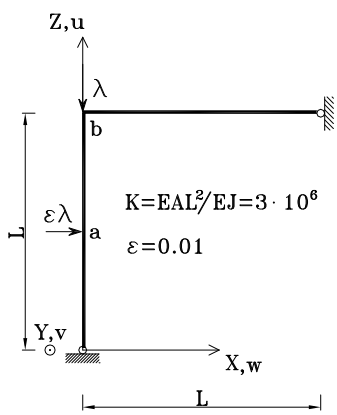

Figure 2. Roorda frame.

Beam analysis elements	ICM λ_b	ICM $\ddot{\lambda}_b/\lambda_b$	ABAQUS λ_b
4	9.880	0.200	9.880
8	9.870	0.238	9.879
16	9.870	0.246	9.870
32	9.870	0.250	9.870

Table 2. Euler beam convergence.

postbuckling curvature $\ddot{\lambda}_b$; we have $\ddot{\lambda}_b/\lambda_b = 0.2844$ for the LS and an even worse estimate $\ddot{\lambda}_b/\lambda_b = -1.4352$ for the LC. Note, from Figure 4, that the paths recovered by asymptotic analysis show good agreement with the reference path-following solution, when using both ICM models (they practically coincide up to a transversal displacement v_a of 10% of the beam length), while the ones obtained by the LC and LS models rapidly deviate with increasing displacement.

A convergence test is also reported in Table 3, including a comparison with the ABAQUS results. Note the good convergence behavior of the ICM model, which confirms that obtained for the Euler beam.

6.2. ***The effect of postbuckling stress redistribution.*** The poor results of both the LC and LS approximate plate models in the previous examples are a direct consequence of their loss of frame invariance. This however does not imply that these models are wholly inadequate in the nonlinear analysis of slender plates. Actually, they provide a satisfactory recovery of the buckling load λ_b and postbuckling slope $\dot{\lambda}_b/\lambda_b$ (at least for initially flat plates) and are inaccurate only in the evaluation of the postbuckling curvature $\ddot{\lambda}_b/\lambda_b$, which only influences the path recovery at large values of the displacements. Moreover, the previous tests were chosen to represent cases with no or very small postbuckling stress redistribution, which can be considered quite unusual for slender plates. If present, the effect of stress redistributions

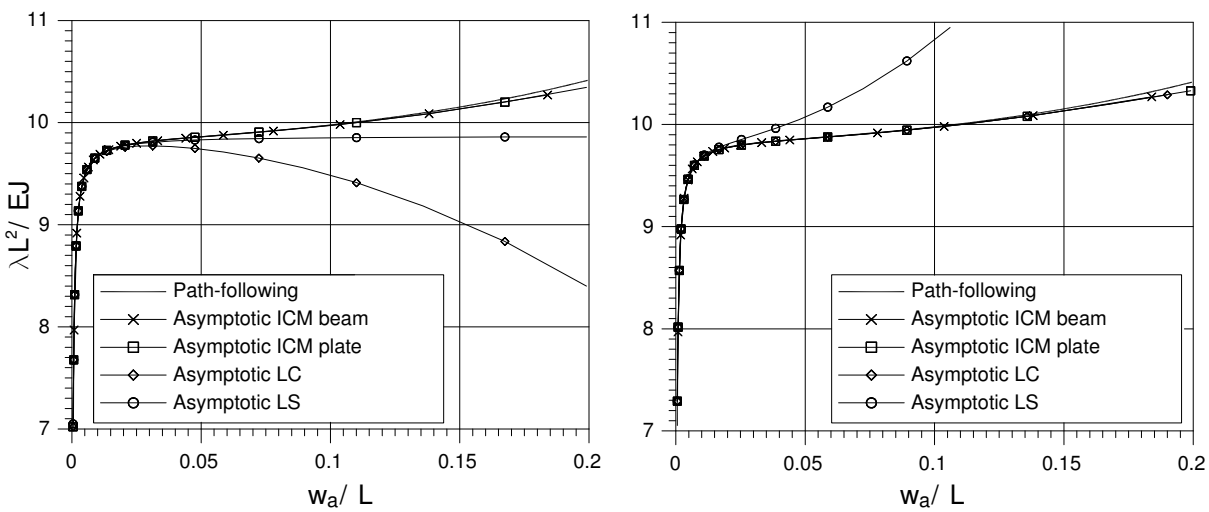

Figure 3. Euler beam: out-plane and in-plane equilibrium paths.

	elements	ICM	S4-R	S8-R	Beam
λ_b	16	13.954	14.005	13.886	13.886
	32	13.903	13.915	13.885	
	64	13.890	13.893	13.884	
$\frac{\dot{\lambda}_b}{\lambda_b}$	16	0.3815	·	·	0.3805
	32	0.3807	·	·	
	64	0.3805	·	·	
$\frac{\ddot{\lambda}_b}{\lambda_b}$	16	0.9070	·	·	0.7574
	32	0.7594	·	·	
	64	0.7570	·	·	

Table 3. Roorda frame: convergence test.

dominates the postbuckling behavior, so reducing the relative size of the error.

Stress redistribution can be considered as a typical phenomenon in the postbuckling behavior of slender plates, especially in the case of relevant local buckling effects. We can show several examples for this, but also counterexamples, as in the following tests.

6.2.1. *Simply supported plate subjected to in-plane shear.* The simply supported plate subjected to in-plane shear shown in Figure 5 represents a suitable test case to show the effects of stress redistribution. In fact, in this case, the buckling mode (see Figure 6) implies a large variation of the Gaussian curvature of the middle surface and consequently a strong in-plane distortion of the plate, with relevant postbuckling stress redistribution.

The plate has been analyzed for $b = 10$, two different aspect ratios, $a = 10$ and $a = 15$, a boundary shear of $\tau = \lambda$, and an imperfection defined by a transversal force $f = 0.01\lambda$ applied at the center of the plate. The results for both the ICM plate models and the approximate LC and LS models are reported

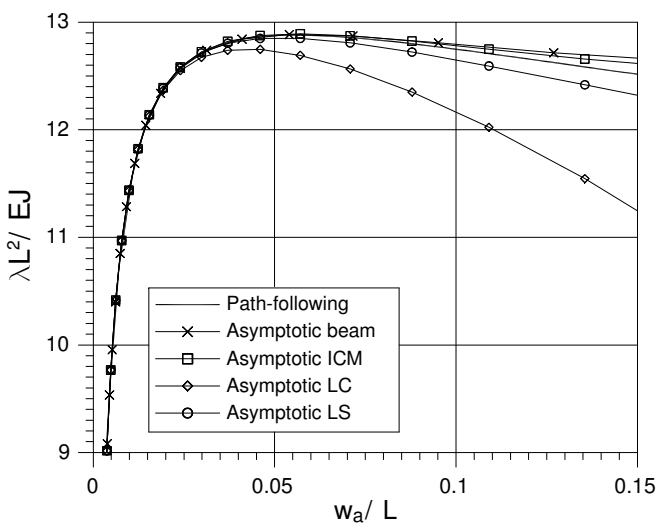

Figure 4. Roorda frame: equilibrium path.

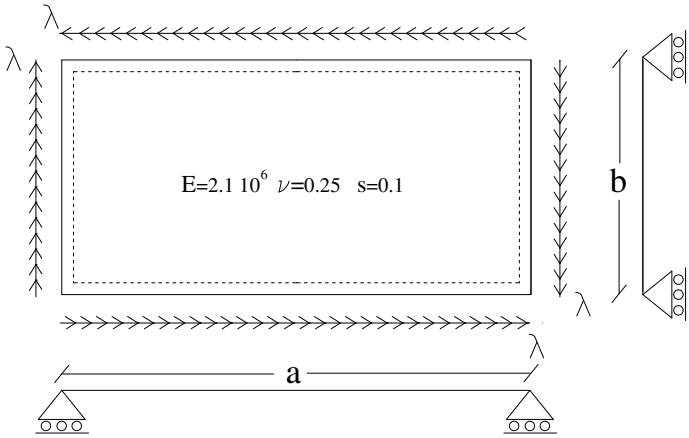

Figure 5. Shear plate: geometry and loads.

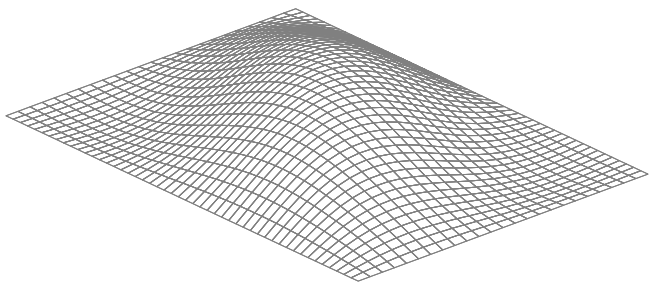

Figure 6. Shear plate: buckling mode ($a/b = 1.5$).

in Figure 7 and Table 4. We obtain from the three models the same evaluations for the buckling load ($\lambda_b = 171.8$ and $\lambda_b = 130.3$) and the postbuckling curvature ($\ddot{\lambda}_b = 5.1474$ and $\ddot{\lambda}_b = 1.053$, referring to the choice $\xi := \varphi_b$) in the two cases of $a/b = 1$ and $a/b = 3/2$. The ICM versus ABAQUS convergence test reported in Table 4 confirms the good convergence behavior of HC-ICM elements.

Note, from Figure 7, the excellent agreement between the asymptotic and path-following paths for moderate transversal displacements (of the order of the plate depth). As the displacement increases, the asymptotic solution tends to deviate by overestimating the load. This deviation is an expected consequence of the asymptotic approach, because of the omission of higher-order terms in the expansion. The error, which is higher than in the previous test cases, can be related to the importance, in this case, of the stress redistribution process which is largely influenced by corrective modes w_{ij}, taken into account in (6h) only to within a third-order accuracy (see also the discussion in [Lanzo et al. 1995]).

6.2.2. *C-section cantilever beam.* This second test refers to the cantilever beam with a C-shaped cross section shown in Figure 8, fully clamped at the first edge (by assuming zero displacements and rotations in each point of the section) and subjected to a shear force at the other edge acting at the top of the web. This structure has a flexural/torsional buckling with a minimal section distortion (see Figure 9), which does not involve noticeable postbuckling stress redistributions. As a consequence, the postbuckling curvature will be very sensitive to the accuracy of the nonlinear modeling, as clearly shown in Figure 8,

Convergence for λ_b at the mesh refining				
a/b	elements	ICM	S4-R	S8-R
1	9×9	173.2	186.7	170.6
	27×27	172.2	172.5	170.2
	81×81	171.8	170.6	170.2
1.5	9×18	132.08	139.0	129.53
	27×54	130.52	130.69	129.46
	81×162	130.28	129.63	129.46

Table 4. Shear plate: λ_b convergence.

which shows the paths recovered by asymptotic analysis, using the three considered plate models, in comparison with the reference path-following one. The latter was obtained using an ICM plate that gives results practically coincident with those of ABAQUS. The good agreement between the ICM results and the reference ones is apparent, while both the LC and LS give highly incorrect answers.

6.2.3. *Need for a robust code implementation.* The previous examples show that asymptotic analysis can be very sensitive to even small approximations in frame invariance requirements. Approximate models can give acceptable results in appropriate contexts, but we need to examine the suitability of the context in advance, or, at least, verify the reliability of the results provided by the analysis. Obviously this is unacceptable in a code aimed at general use and, in order to obtain a robust code implementation, we need to use models which are definitely free from objectivity errors such as those we can set up with the ICM procedure.

6.3. ***Saint-Venant beam versus Kirchhoff plate modeling.*** Tests presented in this subsection compare results from the beam and plate ICM models for thin-walled structures. They show the general accuracy

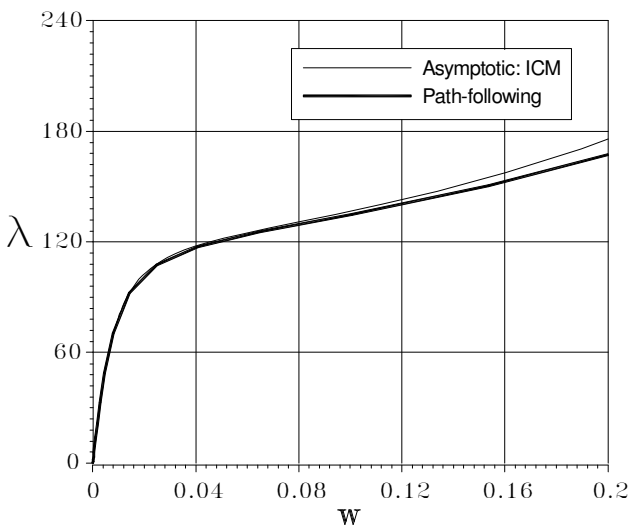

Figure 7. Shear plate: equilibrium paths.

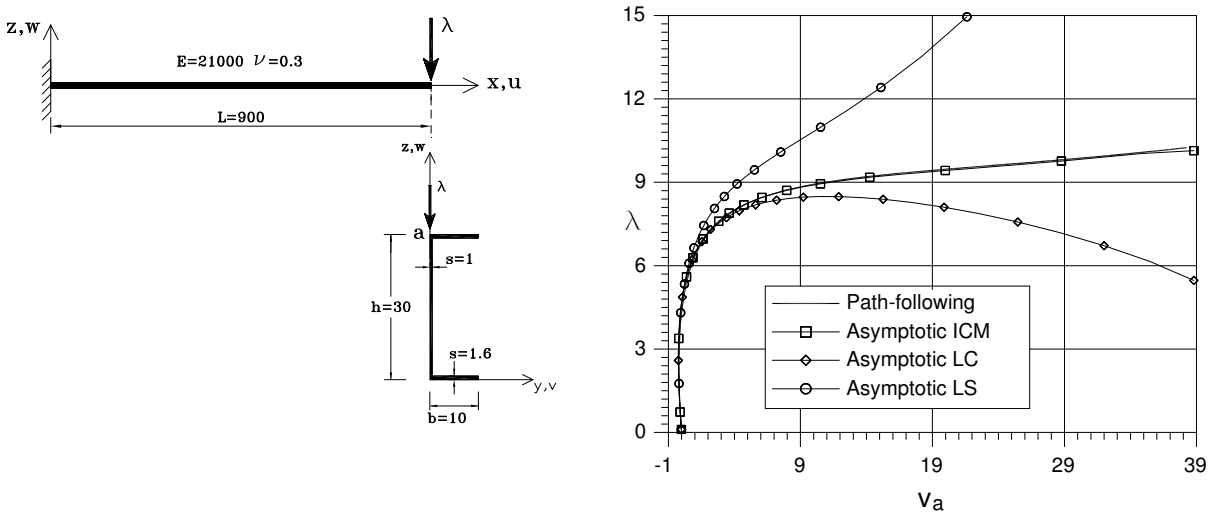

Figure 8. Cantilever beam subjected to shear force: geometry and equilibrium path.

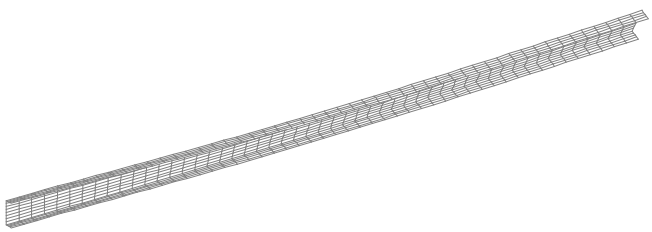

Figure 9. Cantilever beam in Figure 8: buckling mode.

of the proposed beam model with respect to the plate reference solution, but also some differences arising from the presence of relevant boundary disturbances or in-plane distortion of the section which cannot be modeled by Saint-Venant one-dimensional theory.

6.3.1. *Clamped C-section beam under compression or shear.* The first test regards the cantilever beam with a C-shaped cross section, shown in Figure 10. The beam has been analyzed for two loading conditions: the first refers to a compressive force and to a small transversal imperfection, both applied at the barycenter of the free edge section; the second refers to a shear force applied at the same point. In the plate analysis, the loading conditions are described by a constant compressive stress in the overall end section and by a constant shear stress in the web, respectively. In both cases an appropriate constant shear is added in the flanges to reproduce the assigned resultants. The boundary constraints are described either by assuming zero displacements and rotations in all points of the clamped section (full clamped), or by assuming zero displacements and rotations in the web and a stress distribution in the flanges corresponding to the one obtained by the Saint-Venant solution (SV clamped). The latter assumption can be considered more adequate for reproducing the Saint-Venant clamping condition in the shear test. Relatively fine element meshes are utilized for both the beam and plate analyses (16 beam elements and $(5 + 10 + 5) \times 50$ plate elements, respectively) to avoid interference from discretization errors. In all

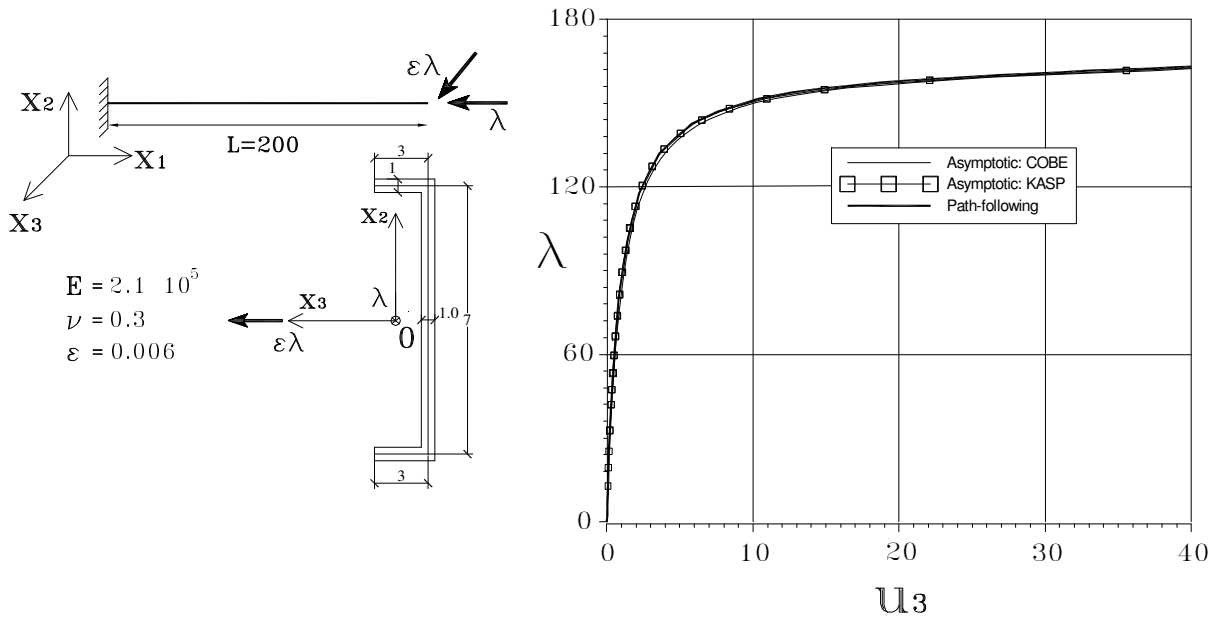

Figure 10. C-beam under axial force: geometry and equilibrium paths.

cases, the path-following results were practically coincident with those provided by asymptotic analysis, at least in the range considered, so their plots were generally omitted.

In the compression test, flexural buckling occurs (see Figure 11) at $\lambda_b = 164.17$, coincident with the analytical solution in [Bazant and L. 1991], for both the beam and plate analyses. We also obtain an excellent agreement between the beam and the two plate solutions, which are practically coincident, in the recovery of the equilibrium path, as shown in Figure 10, by reference to the transversal components of the edge displacement (in the plate case, the plot refers to the average displacement of the edge section).

When considering the results of the shear test, some differences can be seen in Figures 12 and 13, between the results from the ICM plate and beam models, even if the elastic compliance matrix of the beam section is evaluated by the procedure described in [Petrolo and Casciaro 2004] and so the beam

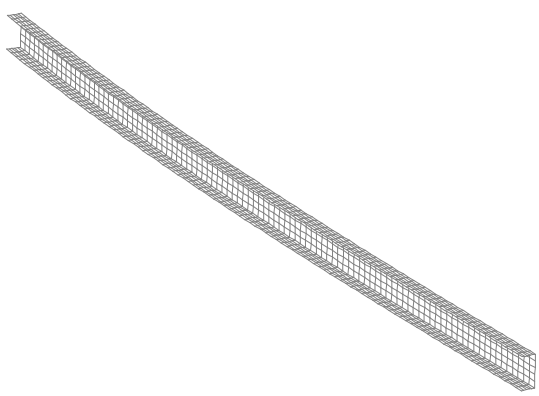

Figure 11. C-beam under axial force: buckling mode.

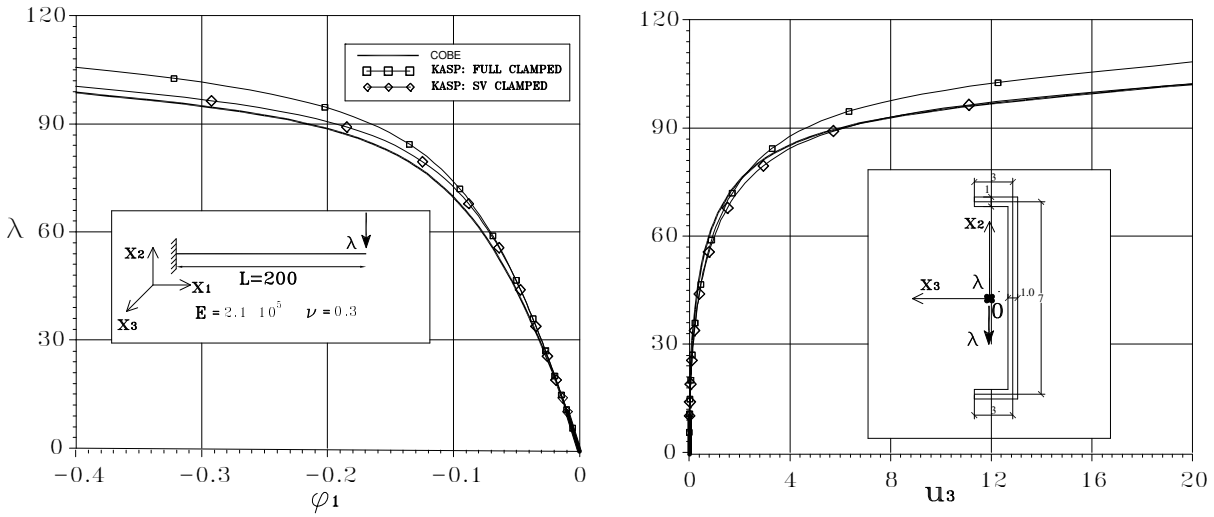

Figure 12. C-beam under shear force: geometry and equilibrium paths.

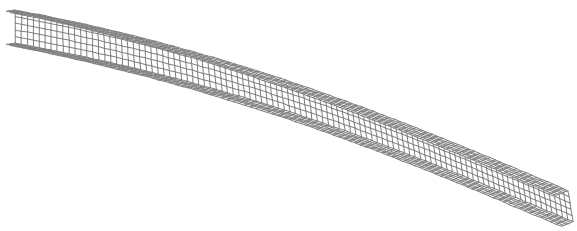

Figure 13. C-beam under shear force: buckling mode.

modeling correctly accounts for all Saint-Venant couplings between shear and torsion. Moreover, in the case of plate analysis, the results are very sensitive to the boundary constraint details. Note that we have a quite large difference, 6%, between the beam and plate results in both the λ/u_3 and λ/φ curves, when considering full clamped constraints. This difference reduces noticeably when considering SV clamped constraints, even if a residual error still remains in the λ/φ plot, which could refer to the overestimate of the torsional flexibility in the Saint-Venant beam solution caused by the omission of the increment in torsional stiffness due to Vlasov's nonuniform torsion.

6.3.2. *Z-shaped section beam under axial/shear forces.* To appropriately relate boundary constraints for the beam and plate models is even more difficult in the case of nonsymmetric sections, as shown by the two test-cases shown in Figures 14 and 16. Both refer to the same cantilever beam with Z-shaped section, with a compressive or a shear force applied at the centroid of the edge section. As before, relatively fine element meshes have been used in both the beam and plate analyses (16 beam elements and $(5+10+5)\times 100$ plate elements) to avoid the influence of discretization errors, and, in the case of the plate, both full clamped and SV clamped have been considered.

In the compressive test, flexural buckling (see Figure 15) occurs at $\lambda_b = 24.371$ for both beam and plate modeling. Plate analysis is practically uninfluenced by the two different boundary conditions. An excellent agreement can also be seen in the equilibrium paths shown in Figure 14.

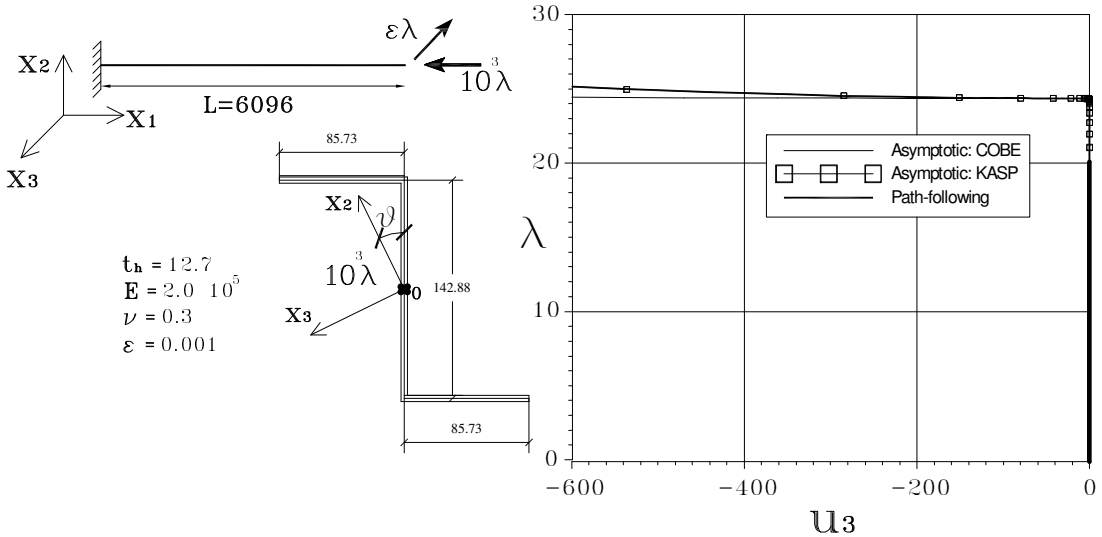

Figure 14. Z-beam under axial force: geometry and equilibrium paths.

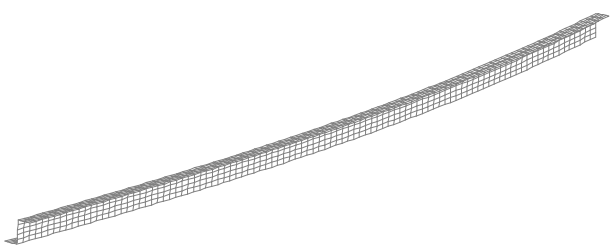

Figure 15. Z-beam under axial force: buckling mode.

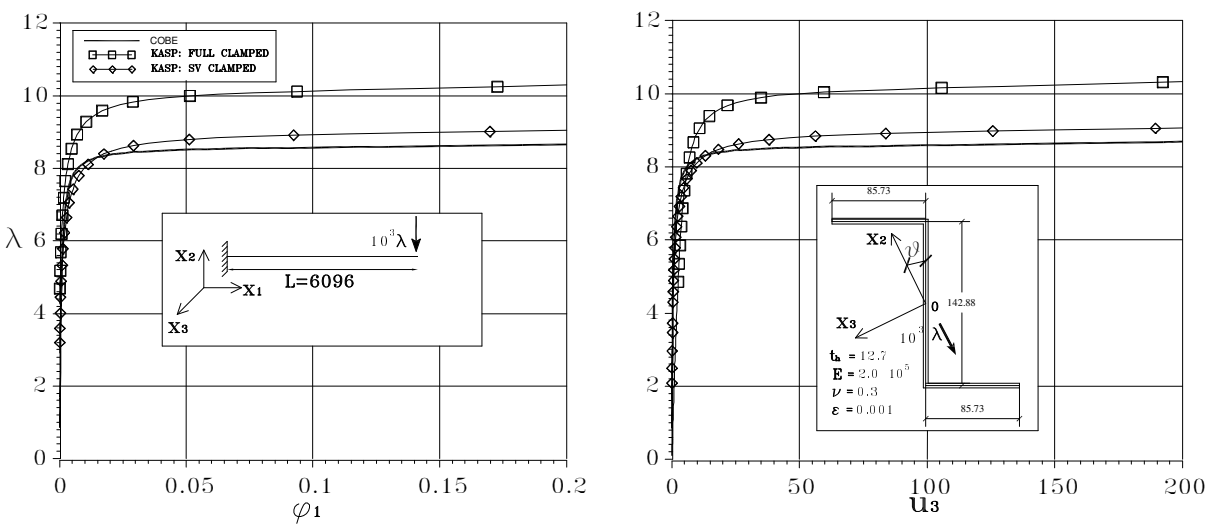

Figure 16. Z-beam under shear force: geometry and equilibrium paths.

Conversely, in the shear test (see Figure 17), we can see from the path comparisons shown in Figure 16 a large difference between the plate and beam models. This is apparent in the full clamped case, which has an error of about 18%, but is also present in the SV clamped case, with an error of 4%, perhaps related to a residual difference in boundary constraints between the plate and beam models or/and to the omission of the Vlasov increment of torsional stiffness in the Saint-Venant beam modeling.

6.3.3. *Wagner effect: flexural/torsional buckling in a compressed T-section cantilever.* The quadratic component $\boldsymbol{\chi}_Q$ of the section strain defined in [Garcea et al. 2012] accounts for the Wagner axial-torsional nonlinear coupling. This effect could be important in compressed thin-walled beams exploiting flexural/torsional buckling. As an example of this, we refer to the cantilever beam with a T-shaped cross section shown in Figure 18. The analysis has been performed for two different beam lengths, $L_1 = 300$ and $L_3 = 500$, using both the ICM beam and plate FEM models. The latter, based on a refined $(4 + 8 + 4) \times 41$ plate element mesh and on the assumption of full clamped constraints, can be assumed as reference. The beam model uses eight beam elements and the analysis is repeated with (Q-ICM) or without (L-ICM) the quadratic term $\boldsymbol{\chi}_Q$, as an expression of the ICM strain (19). In all cases a flexural/torsional buckling is recovered, as shown in Figure 19.

A notable difference in path recovery is obtained from the three FEM models, as shown in Figure 18 and Table 5. Neither of the two beam solutions recovers the reference plate result exactly. The largest discrepancy occurs for the L-ICM solution as a consequence of the loss of the Wagner coupling. A residual error is however present also in the Q-ICM solution, which could be related to in-plane distortion

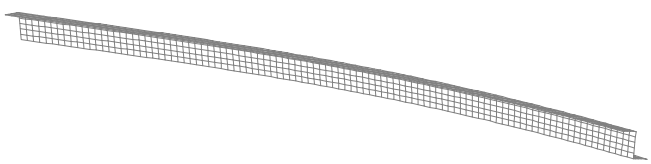

Figure 17. Z-beam under shear force: buckling mode.

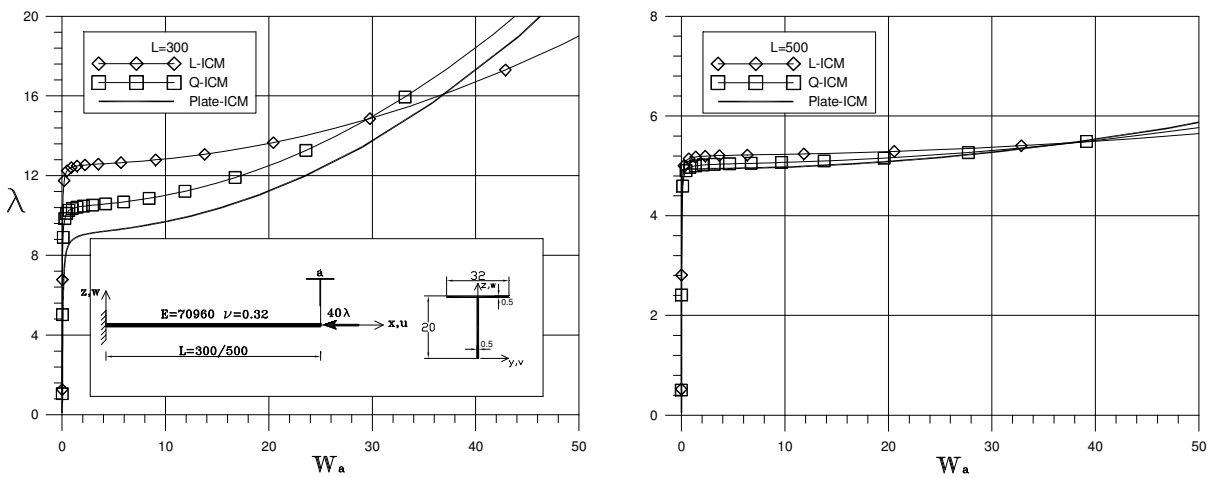

Figure 18. T-beam cantilever: equilibrium paths.

	L	L-ICM	Q-ICM	Plate
λ_b	300	12.601	10.540	9.246
	400	7.754	7.214	6.849
	500	5.219	5.049	4.940
$\ddot{\lambda}_b/2\lambda_b 10^3$	300	1.299	2.447	11.31
	400	0.6354	1.210	2.048
	500	0.3385	0.5648	0.5148

Table 5. T-beam cantilever: buckling parameters.

of the section, neglected in the Saint-Venant solution. The relative error rapidly reduces as the beam length increases, which confirms these interpretations.

6.3.4. *A comment about Saint-Venant beam modeling.* The proposed one-dimensional beam model represents an essential and very simple model in comparison with the plate model. It also allows a very accurate recovery of the buckling and postbuckling behavior in all cases where Saint-Venant assumptions, which are the basis of the model, are satisfied. We have, however, seen that even minor deviations from the Saint-Venant solution can have a nonnegligible effect on both the buckling and postbuckling recovery. So, there is a cost for that simplification.

The relative error could be explained by reference to three possible effects: first, the in-plane distortion of the section, which is allowed by the plate model and ignored by the beam model; second, the Vlasov increment in torsional stiffness due to nonuniform torsion, which is obliged by the Saint-Venant solution; and third, the unsatisfactory correspondence in boundary constraints between the two models which requires a different average alignment of the clamped section. The latter seems to play a major role in some of the examined test cases.

It is worth mentioning that a more accurate recovery could be obtained by refined one-dimensional models which can be derived through the ICM procedure from more sophisticated linear beam theories, such as that of [Vlasov 1959] or even better the ones obtained by the so-called GBT approach (see [Goncalves et al. 2009]) which allow a more realistic modeling of boundary conditions. An investigation of this would be of interest, but is outside the scope of the present paper. Note also that, in any case, when

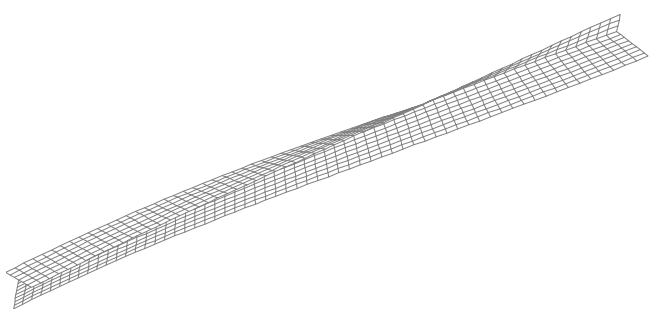

Figure 19. T-beam cantilever ($L = 500$): buckling mode.

analyzing beam assemblages, great care has to be paid to detailed modeling of both boundary constraints and interelement connections.

6.4. ***Modal interaction test: Channel beam in compression.*** The inadequacy of the beam modeling becomes apparent in the presence of local buckling phenomena which produce significant in-plane section distortions, as in the case of the thin-walled Channel beam shown in Figure 20. The beam is subjected to compressive loads applied at the ends (through a uniform distribution on the sections) and to a small transversal load in the middle section (through a uniform distribution on the flanges). A simple support is also assumed at the ends of the bottom plate, and the analysis was performed by either the beam or plate assemblage models, using an eight ICM beam element mesh or $(4+8+4)\times 45$ ICM plate elements, respectively.

The results obtained by the two models are completely different. Beam analysis recovers a simple Eulerian flexural buckling at $\lambda_b = 1290$ (see Figure 21) and provides a stable postbuckling behavior (see Figure 23), while plate assemblage analysis further detects three distortional modes, occurring at $\lambda_b = 1387$, $\lambda_b = 1979$, and $\lambda_b = 2063$ (see Figure 22), and reproduces a complex coupled-buckling phenomenon characterized by a strongly unstable behavior. Note, from Figures 23 and 24, that the interaction between the first two modes changes the postbuckling making it unstable, and a secondary bifurcation, which redirects the path to a strongly unstable branch, is produced because of the activation of localized distortions due to the interaction with the other two modes.

The contribution of fourth mode is actually very small and including further buckling modes in the analysis does not change the overall behavior. This is also confirmed by an independent path-following analysis, whose results are also shown in Figure 23. Note the very good agreement between the path-following and asymptotic analysis. The two paths are practically coincident and only tend to deviate,

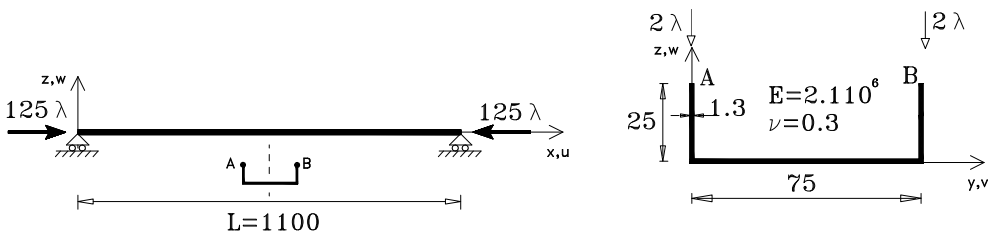

Figure 20. Channel beam: geometry.

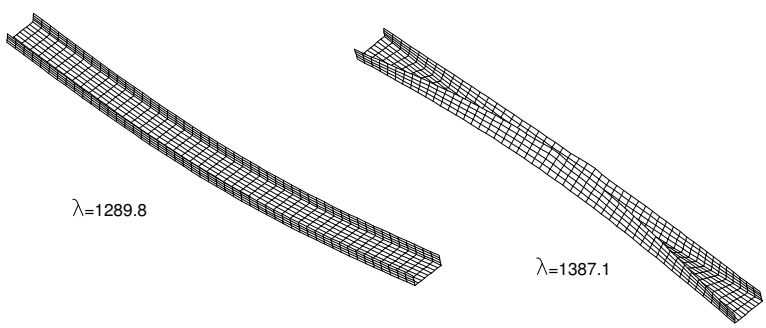

Figure 21. Channel beam: flexural and distortional buckling modes.

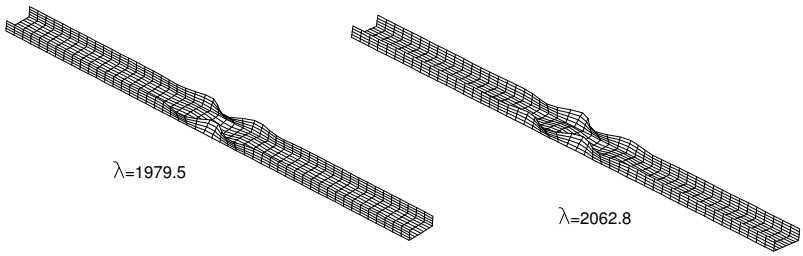

Figure 22. Channel beam: local distortional buckling modes.

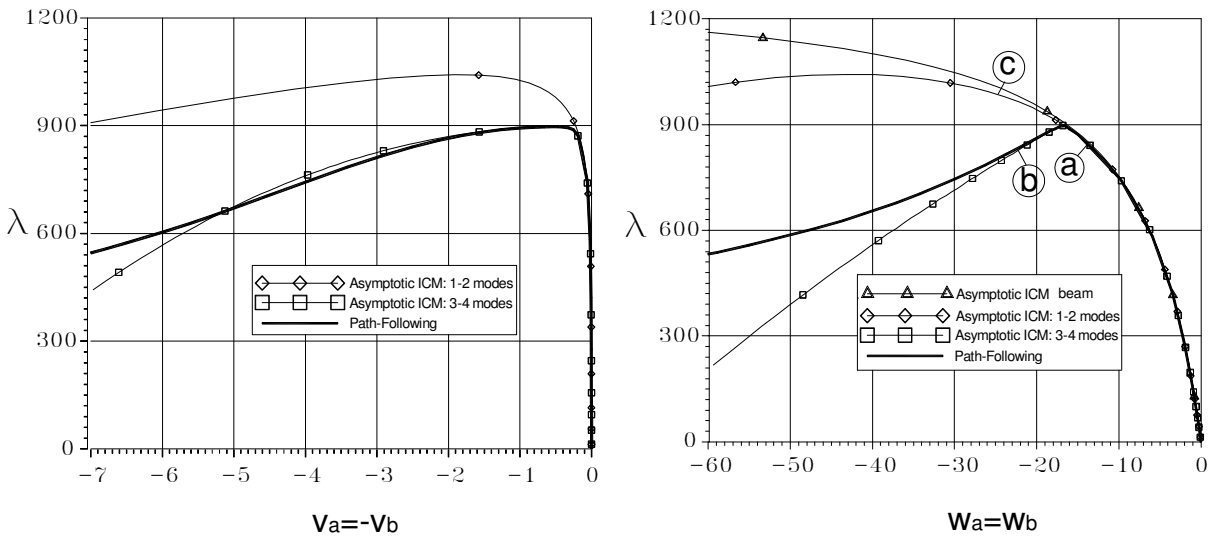

Figure 23. Channel beam: equilibrium paths.

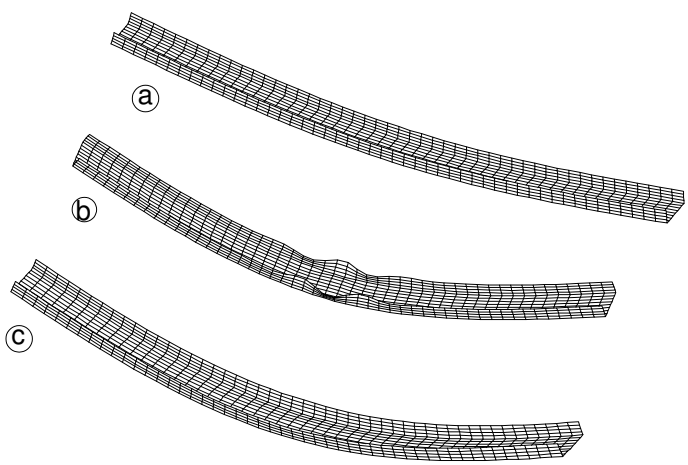

Figure 24. Channel beam: equilibrium configurations at a, b, and c.

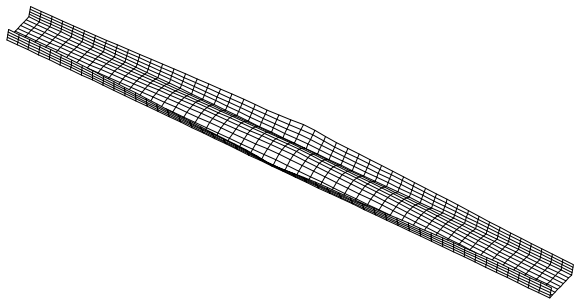

Figure 25. Channel beam: corrective mode in the one-mode analysis.

after the secondary bifurcation, in correspondence to a quite large distortion of the middle section (see Figure 24b). Note also that, in plate analysis, the same unstable behavior determined by the two-mode analysis is also recovered by considering the first (purely flexural) mode alone. This result might be surprising but it is due to the fact that a section distortion, similar to that coming from the second buckling mode, is also contained in the corrective mode w_{11} (see Figure 25). So the one-mode analysis can actually reproduce the flexural/distortional evolution of the buckling process.

The previous results clearly show that beam modeling, at least if based on Saint-Venant theory, can be inadequate in problems presenting coupled buckling with relevant in-plane section distortions. So it has to be used with certain care in the analysis of thin-walled folded plates. But they also show, from the results of plate analysis, the accuracy and reliability of the ICM approach in these quite difficult contexts.

7. Concluding remarks

The implicit corotational method (ICM) has been developed in [Garcea et al. 2012] as a general procedure for deriving frame-independent nonlinear structural models starting from the corresponding linear theories. Its use as a numerical tool, able to provide relevant results in technical practice, requires the implementation of the recovered models within a finite element approach. While the implementation procedure could be similarly as straightforward as that used in linear analysis, some difficulties can arise due to the presence of finite three-dimensional rotations and the need to assure frame invariance, as well as in the interpolation of the mechanical quantities internal to the element.

Different aspects of FEM implementation have been discussed, in relation to path-following or asymptotic analysis approaches, and some suitable strategies have been suggested to avoid locking problems related to the loss of frame invariance in the element definition or to an inappropriate format in their representation.

Two elements have been described in detail. The elements are derived from nonlinear models defined in [Garcea et al. 2012], through a separate (mixed) interpolation of the displacement and stress fields, and they are described in a mixed format which uses both stress and displacement control variables. The first element derives from the nonlinear three-dimensional beam model based on Saint-Venant rod theory described in [Garcea et al. 2012, §5]. It uses quite simple interpolation laws, directly derived from the linear case, and can be considered the simplest choice in the nonlinear beam context. The second is derived from the thin-plate model based on Kirchhoff linear theory described in [Garcea et al. 2012, §6]. It uses a spline interpolation for the translations which allows a rotation-free kinematical

description. This interpolation, which has already been used in [Garcea 2001], implies C^1 continuity for the displacement field and is highly suitable for the discrete modeling of rectangular plates and their three-dimensional assemblages.

The elements have been inserted into the two computer codes COBE [Madeo 2008] and KASP [Garcea 2001], aimed at the FEM analysis of three-dimensional beam or plate assemblages, using either path-following or asymptotic solution strategies. Extensive numerical testing has been performed with these codes and some of the results have been reported and discussed in Section 6. In all cases the proposed elements show strong robustness and high accuracy when compared with existing reference analytical solutions. The good agreement between the results obtained by an independent modeling of thin-walled structures, such as Saint-Venant beams or Kirchhoff plates assemblages, gives a further mutual validation of both models, and differences, if present, are clearly related to some inadequacies in Saint-Venant linear theory. The inadequacy of Saint-Venant beam modeling in the presence of relevant in-plane section distortions, as well as the overall effectiveness of the proposed approach and its ability to recover even complex buckling behavior, is apparent from the results reported in Section 6.4.

It is worth mentioning that both proposed elements should be viewed as first simple implementation examples, only aimed at showing the effectiveness of the ICM as a computational tool to be used in FEM analysis for solving practical problems. More refined elements with even better behavior can be derived for both beams and plates, starting from the nonlinear models presented in [Garcea et al. 2012]. Further elements can also be obtained by more refined nonlinear continua which can be derived through the ICM approach as nonlinear generalizations of more sophisticated linear theories, such as, for instance, the Vlasov or GBT beam theories or laminated shell theory.

References

[Alsafadie et al. 2010] R. Alsafadie, M. Hjiaj, and J.-M. Battini, "Corotational mixed finite element formulation for thin-walled beams with generic cross-section", *Comput. Methods Appl. Mech. Eng.* **199**:49-52 (2010), 3197–3212.

[Alsafadie et al. 2011] R. Alsafadie, J.-M. Battini, H. Somja, and M. Hjiaj, "Local formulation for elasto-plastic corotational thin-walled beams based on higher-order curvature terms", *Finite Elem. Anal. Des.* **47**:2 (2011), 119–128.

[Argyris et al. 1979] J. H. Argyris, H. Balmer, S. S. Doltsinis, P. C. Dunne, M. Haase, M. Kleiber, G. A. Malejannakis, H. P. Mlejnek, M. Muller, and D. W. Scharpf, "Finite element method - The natural approach", *Comput. Methods Appl. Mech. Eng.* **17-18**:1 (1979), 1–106.

[Aristodemo 1985] M. Aristodemo, "A high-continuity finite element model for two–dimensional elastic problem", *Comput. Struct.* **21**:5 (1985), 987–993.

[Babuška 1971] I. Babuška, "Error-bounds for finite element method", *Numer. Math.* **16**:4 (1971), 322–333.

[Bazant and L. 1991] Z. P. Bazant and C. L., *Stability of Structurers*, Dover, New York, 1991.

[Bilotta et al. 2012] A. Bilotta, L. Leonetti, and G. Garcea, "An algorithm for incremental elastoplastic analysis using equality constrained sequential quadratic programming", *Comput. Struct.* **102-103** (2012), 97–107.

[Boutyour et al. 2004] E. H. Boutyour, H. Zahrouni, M. Potier-Ferry, and M. Boudi, "Asymptotic-numerical method for buckling analysis of shell structures with large rotations", *J. Comput. Appl. Math.* **168**:1-2 (2004), 77–85.

[Brezzi 1974] F. Brezzi, "On the existence, uniqueness and approximation of saddle-point problems arising from Lagrangian multipliers", *Rev. Française Automat. Informat. Recherche Opérationnelle Sér. Rouge* **8**:R-2 (1974), 129–151.

[Brezzi et al. 1986] F. Brezzi, M. Cornalba, and A. Di Carlo, "How to get around a simple quadratic fold", *Numer. Math.* **48**:4 (1986), 417–427.

[Budiansky 1974] B. Budiansky, *Theory of buckling and post–buckling of elastic structures*, Advances in Applied Mechanics **14**, Academic Press, New York, 1974.

[Casciaro 2004] R. Casciaro, "A fast iterative solver for nonlinear eigenvalue problem", report 35, LABMEC, University of Calabria, 2004, Available at www.labmec.unical.it/pubblicazioni/collana.php.

[Casciaro 2005] R. Casciaro, *Computational asymptotic post-buckling analysis of slender elastic structures*, CISM Courses and Lectures **470**, Springer, Wien, 2005.

[Casciaro and Garcea 2002] R. Casciaro and G. Garcea, "An iterative method for shakedown analysis", *Comput. Methods Appl. Mech. Eng.* **191**:49-50 (2002), 5761–5792.

[Casciaro and Mancusi 2006] R. Casciaro and G. Mancusi, "Imperfection sensitivity due to coupled local instability: a non-convex QP solution algorithm", *Int. J. Numer. Methods Eng.* **67**:6 (2006), 815–840.

[Casciaro et al. 1992] R. Casciaro, G. Salerno, and A. D. Lanzo, "Finite element asymptotic analysis of slender elastic structures: a simple approach", *Int. J. Numer. Methods Eng.* **35**:7 (1992), 1397–1426.

[Casciaro et al. 1998] R. Casciaro, G. Garcea, G. Attanasio, and F. Giordano, "Perturbation approach to elastic post-buckling analysis", *Comput. Struct.* **66**:5 (1998), 585–595.

[Chen and Virgin 2006] H. Chen and L. N. Virgin, "Finite element analysis of post-buckling dynamics in plates, I: An asymptotic approach", *Int. J. Solids Struct.* **43**:13 (2006), 3983–4007.

[Chen et al. 2006] H. H. Chen, W. Y. Lin, and K. M. Hsiao, "Co-rotational finite element formulation for thin-walled beams with generic open section", *Comput. Methods Appl. Mech. Eng.* **195**:19-22 (2006), 2334–2370.

[Flores and Godoy 1992] F. G. Flores and L. A. Godoy, "Elastic postbuckling analysis via finite element and perturbation techniques, I: Formulation", *Int. J. Numer. Methods Eng.* **33**:9 (1992), 1775–1794.

[Garcea 2001] G. Garcea, "Mixed formulation in Koiter analysis of thin-walled beam", *Comput. Methods Appl. Mech. Eng.* **190**:26-27 (2001), 3369–3399.

[Garcea and Leonetti 2011] G. Garcea and L. Leonetti, "A unified mathematical programming formulation of strain driven and interior point algorithms for shakedown and limit analysis", *Int. J. Numer. Methods Eng.* **88**:11 (2011), 1085–1111.

[Garcea et al. 1998] G. Garcea, G. A. Trunfio, and R. Casciaro, "Mixed formulation and locking in path-following nonlinear analysis", *Comput. Methods Appl. Mech. Eng.* **165**:1-4 (1998), 247–272.

[Garcea et al. 1999] G. Garcea, G. Salerno, and R. Casciaro, "Extrapolation locking and its sanitization in Koiter asymptotic analysis", *Comput. Methods Appl. Mech. Eng.* **180**:1-2 (1999), 137–167.

[Garcea et al. 2002] G. Garcea, G. A. Trunfio, and R. Casciaro, "Path-following analysis of thin-walled structures and comparison with asymptotic post-critical solutions", *Int. J. Numer. Methods Eng.* **55**:1 (2002), 73–100.

[Garcea et al. 2005] G. Garcea, G. Formica, and R. Casciaro, "A numerical analysis of infinitesimal mechanisms", *Int. J. Numer. Methods Eng.* **62**:8 (2005), 979–1012.

[Garcea et al. 2009] G. Garcea, A. Madeo, G. Zagari, and R. Casciaro, "Asymptotic post-buckling FEM analysis using a corotational formulation", *Int. J. Solids Struct.* **46**:2 (2009), 523–532.

[Garcea et al. 2012] G. Garcea, A. Madeo, and R. Casciaro, "The implicit corotational method and its use in the derivation of nonlinear structural models for beams and plates", *J. Mech. Mater. Struct.* **7**:6 (2012), 509–538.

[Goncalves et al. 2009] R. Goncalves, P. B. Dinis, and D. Camotim, "GBT formulation to analyse the first-order and buckling behaviour of thin-walled members with arbitrary cross-sections", *Thin-Walled Struct.* **47**:5 (2009), 583–600.

[Hibbitt et al. 2007] Hibbitt, Karlsson, and Sorenson, "ABAQUS Version 6.7", Pawtucket, 2007.

[Hughes et al. 2005] T. J. R. Hughes, J. A. Cottrell, and Y. Bazilevs, "Isogeometric analysis: CAD, finite elements, NURBS, exact geometry and mesh refinement", *Comput. Methods Appl. Mech. Eng.* **194**:39-41 (2005), 4135–4195.

[Koiter 1945] W. T. Koiter, *On the stability of elastic equilibrium*, Ph.D. thesis, 1945.

[Lacarbonara and Paolone 2007] W. Lacarbonara and A. Paolone, "On solution strategies to Saint-Venant problem", *J. Comput. Appl. Math.* **206**:1 (2007), 473–497.

[Lanzo and Garcea 1996] A. D. Lanzo and G. Garcea, "Koiter analysis of thin-walled structures by a finite element approach", *Int. J. Numer. Methods Eng.* **39**:17 (1996), 3007–3031.

[Lanzo et al. 1995] A. D. Lanzo, G. Garcea, and R. Casciaro, "Koiter post-buckling analysis of elastic plates", *Int. J. Numer. Methods Eng.* **38**:14 (1995), 2325–2345.

[M. and C. 2002] B. J. M. and P. C., "Co-rotational beam elements with warping effects in instability problems", *Comput. Methods Appl. Mech. Eng.* **191**:17-18 (2002), 1755–1789.

[Madeo 2008] A. Madeo, *The implicit corotational method: General theory and FEM implementation*, Ph.D. thesis, LABMEC, University of Calabria, 2008, Available at www.labmec.unical.it/dottorato/tesi/Madeo.pdf.

[Pacoste and Eriksson 1995] C. Pacoste and A. Eriksson, "Element behavior in post-critical plane frame analysis", *Comput. Methods Appl. Mech. Eng.* **125**:1-4 (1995), 319–343.

[Petrolo and Casciaro 2004] A. S. Petrolo and R. Casciaro, "3D beam element based on Saint Venánt's rod theory", *Comput. Struct.* **82**:29-30 (2004), 2471–2481.

[Poulsen and Damkilde 1998] P. N. Poulsen and L. Damkilde, "Direct determination of asymptotic structural postbuckling behaviour by the finite element method", *Int. J. Numer. Methods Eng.* **42**:4 (1998), 685–702.

[Rahman and Jansen 2010] T. Rahman and E. L. Jansen, "Finite element based coupled mode initial post-buckling analysis of a composite cylindrical shell", *Thin-Walled Struct.* **48**:1 (2010), 25–32.

[Rankin and Nour-Omid 1988] C. C. Rankin and B. Nour-Omid, "The use of projectors to improve finite element performance", *Comput. Struct.* **30**:1-2 (1988), 257–267.

[Riks 1979] E. Riks, "An incremental approach to the solution of snapping and buckling problems", *Int. J. Solids Struct.* **15**:7 (1979), 529–551.

[Riks 1987] E. Riks, "Progress in collapse analysis", *J. Pressure Vessel Technol.* (*ASME*) **109**:1 (1987), 33–41.

[Riks 2004] E. Riks, "Buckling", pp. xii+830 in *Encyclopedia of computational mechanics*, vol. 2, edited by E. Stein et al., Wiley, Chichester, 2004.

[Ritto-Corrêa and Camotim 2002] M. Ritto-Corrêa and D. Camotim, "On the differentiation of the Rodrigues formula and its significance for the vector-like parameterization of Reissner-Simo beam theory", *Int. J. Numer. Methods Eng.* **55**:9 (2002), 1005–1032.

[Rodrigues 1840] O. Rodrigues, "Des lois géometriques qui régissent les déplacements d'un système solide dans l'espace", *J. Math. Pures Appl.* **5** (1840), 380–440.

[Salerno and Casciaro 1997] G. Salerno and R. Casciaro, "Mode jumping and attractive paths in multimode elastic buckling", *Int. J. Numer. Methods Eng.* **40**:5 (1997), 833–861.

[Salerno and Lanzo 1997] G. Salerno and A. D. Lanzo, "A nonlinear beam finite element for the post-buckling analysis of plane frame by Koiter's perturbation approach", *Comput. Methods Appl. Mech. Eng.* **146**:3-4 (1997), 325–349.

[Salerno and Uva 2006] G. Salerno and G. Uva, "Ho's theorem in global-local mode interaction of pin-jointed bar structures", *Int. J. Non-Linear Mech.* **41**:3 (2006), 359–376.

[Schafer and Graham-Brady 2006] B. W. Schafer and L. Graham-Brady, "Sthocastic post-buckling of frames using Koiter methods", *Int. J. Struct. Stab. Dynamics* **6**:3 (2006), 333–358.

[Silvestre and Camoti 2005] N. Silvestre and D. Camoti, "Asymptotic-Numerical Method to Analyze the Postbuckling Behavior, imperfection-Sensitivity, and Mode Interaction in Frames", *J. Eng. Mech.* (*ASCE*) **131**:6 (2005), 617–632.

[Vlasov 1959] V. Z. Vlasov, Тонкостенные упругие стержни, Fizmatgiz, Moscow, 1959. Translated as *Thin walled elastic beams*, NSF (Washington, DC) and Israel Program for Scientific Translations (Jerusalem), 1961.

[Wu and Wang 1997] B. Wu and Z. Wang, "A perturbation method for the determination of the buckling strength of imperfection-sensitive structures", *Comput. Methods Appl. Mech. Eng.* **145**:3-4 (1997), 203–215.

Received 30 May 2012. Revised 30 Aug 2012. Accepted 14 Sep 2012.

GIOVANNI GARCEA: giovanni.garcea@unical.it
Dipartimento di Modellistica per l'ingegneria, Università della Calabria, Via P. Bucci Cubo 39/C 87036 Rende (CS), Italy

ANTONIO MADEO: antonio.madeo81@unical.it
Dipartimento di Modellistica per l'ingegneria, Università della Calabria, Via P. Bucci Cubo 39/C 87036 Rende (CS), Italy

RAFFAELE CASCIARO: raffaele.casciaro@unical.it
Dipartimento di Modellistica per l'ingegneria, Università della Calabria, Via P. Bucci Cubo 39/C 87036 Rende (CS), Italy

JOURNAL OF MECHANICS OF MATERIALS AND STRUCTURES
Vol. 7, No. 6, 2012
dx.doi.org/10.2140/jomms.2012.7.575

DAMAGE DEVELOPMENT IN AN ARMOR ALUMINA IMPACTED WITH DUCTILE METAL SPHERES

BRETT G. COMPTON, ELEANOR A. GAMBLE, VIKRAM S. DESHPANDE AND FRANK W. ZOK

The present article describes a coupled experimental/computational study of damage development in confined ceramic tiles impacted by spherical metal projectiles. The principal objective is to calibrate the material parameters in the Deshpande–Evans constitutive model for an armor alumina and assess its utility in predicting trends in damage development with impact velocity. The nature of the damage at the impact site is probed through optical and scanning electron microscopy of cross-sections through the impact site as well as surface profile measurements. Once calibrated, the model is used in finite element simulations and shown to predict reasonably accurately the variation in the size of the comminuted zone beneath the impact site with incident projectile velocity. The numerical simulations also provide new insights into the spatial and temporal evolution of subsurface damage and deformation processes as well as the role of metal face sheets in the these processes.

1. Introduction

The ballistic performance of ceramics cannot be readily predicted solely on the basis of material composition and microstructure nor on the basis of common physical and mechanical properties. Consequently, the pathway to developing better materials for armor systems remains ill-defined. The goal of the present study is to advance the understanding of the connections between ballistic resistance and intrinsic material properties of ceramics. The study consists of a coupled experimental/computational study of damage development in confined ceramic tiles impacted by spherical metal projectiles. The computational portion utilizes a mechanistic model of ceramic deformation in which the calibrating parameters relate directly to normative material properties. Through numerical simulations of representative impact scenarios, the model has the potential to identify the key microstructural characteristics that govern ballistic performance and hence guide the directions of future material development activities. It could also prove to be an effective tool in the design of armor systems.

Although the relationships between failure mechanisms and material properties during ballistic impact have been studied extensively [Ashby and Sammis 1990; Compton et al. 2011; Longy and Cagnoux 1989; Rhee et al. 2001; Shih et al. 2000], no consensus exists on exactly how hardness, toughness and strength affect ballistic performance. In regard to penetration resistance, hardness, H, is arguably the most important material property; a hard material is more effective than a soft one at deforming and eroding an impacting projectile. Fracture toughness, K_C, is a second. A material with low toughness has greater propensity for fragmentation and comminution at an impact site, rendering the material ineffective at further impeding projectile penetration. But the tradeoffs between these two properties — H and K_C — are poorly understood. For instance, altering material composition or microstructure to increase

Keywords: impact, ceramic, damage, microcracking.

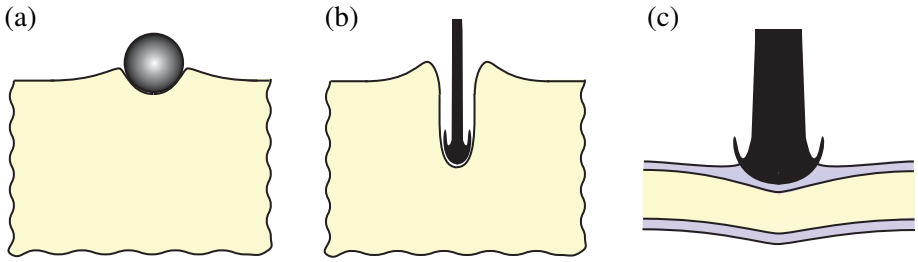

Figure 1. Model impact scenarios used to probe material responses and assess material models: (a) penetration initiation; (b) deep penetration; (c) trilayer penetration.

hardness usually results in a lower toughness, and vice versa [Chantikul et al. 1990]. Predicting with confidence whether the combined changes improve or diminish ballistic performance is presently not possible. Furthermore, it is unlikely that property changes have the same effect under all impact scenarios.

The Young's modulus, E, and the mass density, ρ, can also play important roles. For instance, a material with a high acoustic impedance, $\sqrt{E\rho}$, generates a higher stress on an impacting projectile and is thus more effective at impeding penetration. Naturally the benefits of a material with higher density come at the expense of increased system weight (assuming that volume is held fixed).

With the goal of establishing connections between ballistic performance and material properties, Deshpande et al. [2011] devised a mechanistic constitutive model for deformation and damage of ceramics. The model has been coded as a user-material subroutine for use in the finite element code ABAQUS. Three modes of deformation are included: dislocation plasticity, distributed microcracking, and granular flow of fully comminuted material. Additional details of the model are presented below.

The study is part of a broader effort to probe, both experimentally and computationally, the features associated with various impact scenarios and the effects of material properties. Three such scenarios are illustrated in Figure 1. The one in (a) — penetration initiation — is the focus of the present paper. The second (b) deals with deep penetration by long-rod projectiles and the third (c) involves penetration through ceramic/metal multilayers. Analyses and simulations of the latter scenarios will be presented elsewhere.

The predictive capabilities of this model in the quasi-static deformation regime were demonstrated in [Gamble et al. 2011]. The principal objective of the present study is to assess the capabilities of the DE model *in the dynamic deformation regime* for predicting *damage initiation and growth* in a ceramic in the vicinity of an impact. This is accomplished through comparisons between numerical simulations and experimental observations on impact damage in an armor ceramic. A secondary objective is to relate the damage development sequence during impact to the temporal evolution of contact pressure and force at the impact site.

2. Materials and experimental methods

Experiments were conducted on a fine-grained armor-grade ceramic (Corbit 98, produced by Industri Bitossi and characterized in [Gamble et al. 2011; Denzel 2010]). The material consists of 98% alumina and minor amounts of a glassy phase at the grain boundaries. It was obtained and tested in the form of 50 mm × 50 mm × 12 mm tiles.

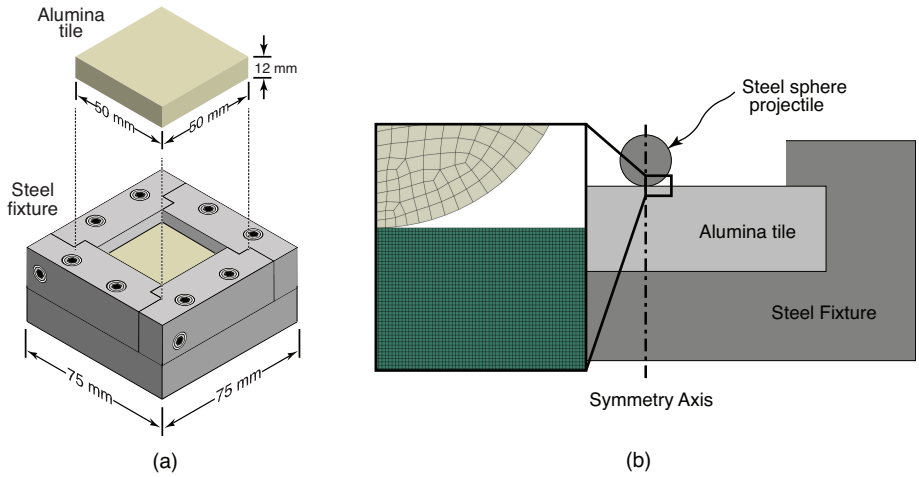

Figure 2. (a) Schematic of alumina target and steel fixture used for impact tests. (b) The corresponding finite element geometry and mesh.

Impact tests were conducted in one of two light-gas guns using either helium or nitrogen as the propellant. Each tile was inserted and clamped within a steel fixture, illustrated in Figure 2. To ensure intimate contact between the tile face and the fixture, 0.1 mm thick steel shims were placed between all lateral faces. Additionally, to protect the back plate of the fixture, a sacrificial 1 mm thick annealed 4130 steel sheet was placed between the back face of the tile and the fixture. The fixture was bolted together and tightened to roughly 10 MPa lateral compression. In some instances, a sheet of 304 stainless steel (either 0.5 or 1 mm thick) was placed on the front face of the ceramic target, to assess the effects of such sheets on the damage process. The target assembly was then mounted in the gas gun against a thick steel backing. The target was impacted with a 304 stainless steel sphere, either 7.6 or 7.15 mm in diameter (depending on the sabot design for the two gas guns). Spheres were obtained from Salem Specialty Ball Company and McMaster-Carr. Tests were performed at velocities in the range 250–800 m/s. Velocities were measured by laser gates.

Following impact, the tile was removed from the test fixture, coated with a dye-penetrant (to enhance viewing of cracks) and imaged using macro-photography. Surface profiles of the tile at and around the impact site were measured using a Wyko NT1100 Optical Profiling System^{TM}. To image subsurface damage, the tiles were first cast in epoxy (to prevent material loss during subsequent operations) and sectioned through the point of impact with a diamond wafering blade. As-cut surfaces were sufficient to identify the presence and approximate size of the comminuted regions as well as the cone and radial cracks via macro-photography. In some instances, the sectioned surfaces were polished to 0.5 μm finish and subsequently examined with optical and scanning electron microscopy.

3. Experimental observations and measurements

The key experimental results are illustrated in Figures 3–5. They reveal the following trends.

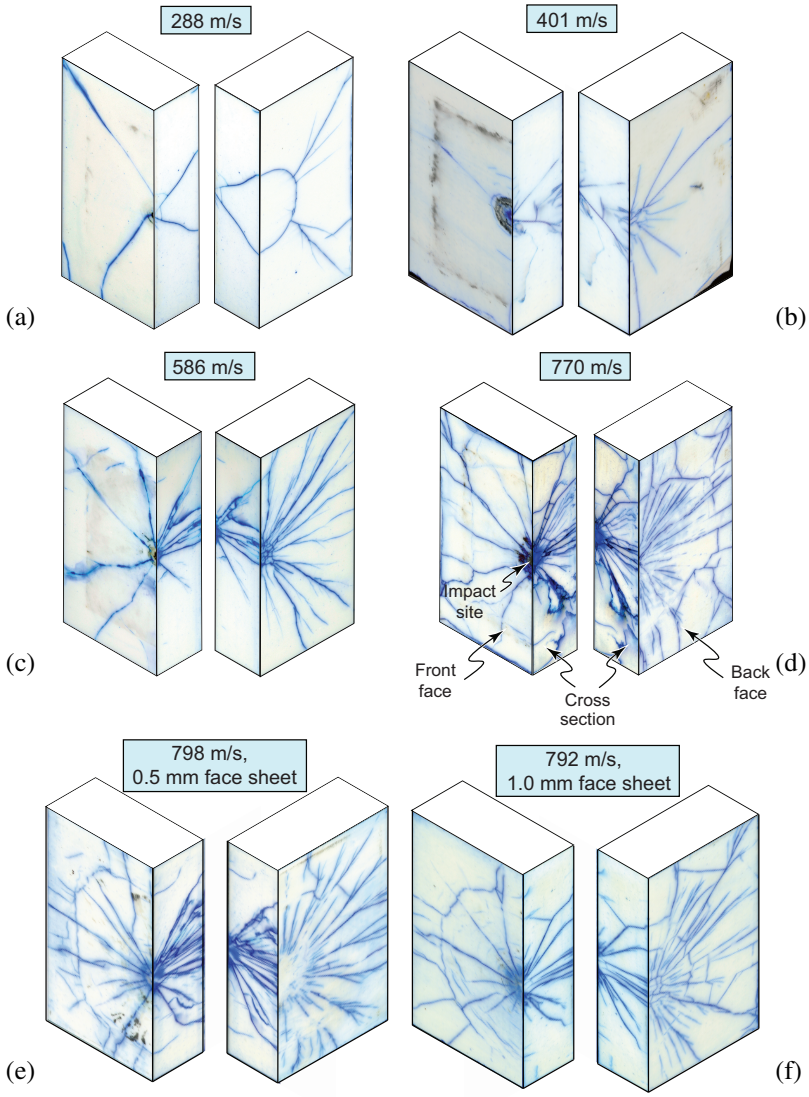

Figure 3. Crack patterns and damage in impacted alumina tiles.

At low impact velocities, defined by V_0 <350 m/s, a single dominant cone crack is observed emanating from the impact site with no evidence of a residual crater (Figure 3a). At slightly higher velocities, typically 350–400 m/s, the cone crack is accompanied by a small number (5–10) of radial cracks, principally on the back face, but also present to a lesser extent on the impact face. The first indications of a permanent crater appear, manifested as slight surface depressions ($\approx$ 1–5 μm). Within the resolution of the imaging techniques employed in this study, there does not appear to be evidence of microcracking at the impact site in this velocity range.

More dramatic changes are observed at velocities $\geq$500 m/s. In addition to increased densities of cone cracks and radial cracks, the crater becomes more pronounced and a well-defined comminuted zone directly beneath the impact site emerges. The latter zone is manifested macroscopically as a distinct

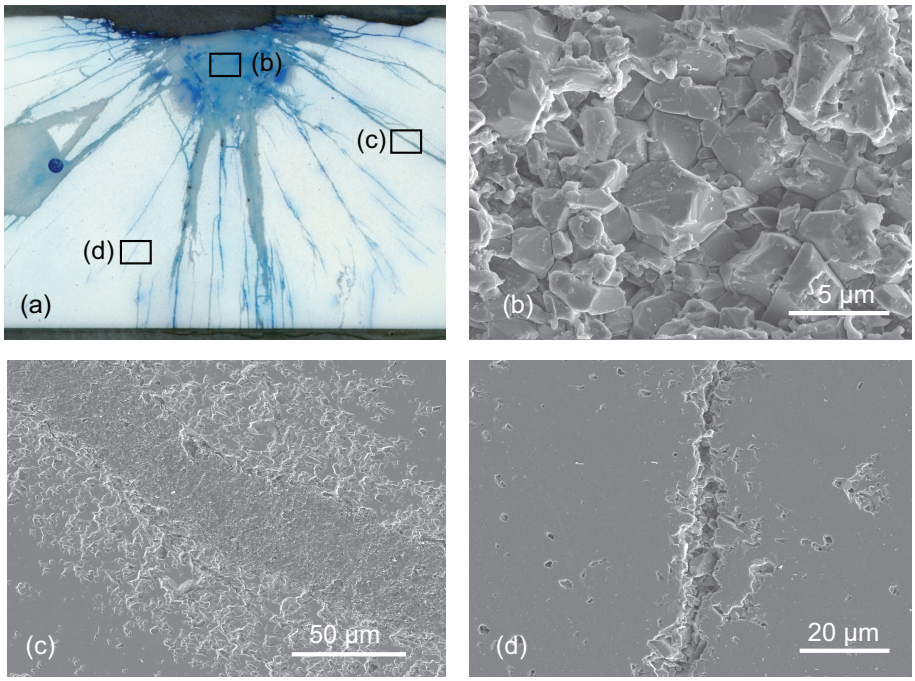

Figure 4. Cross-section through specimen impacted at 778 m/s. (a) Optical overview of the damage zone. (b) SEM image of the comminuted region. (c) A dominant cone crack. The central 50 μm wide band is epoxy that had filled the crack during sample preparation. Flanking this are 50 μm wide strips of microcracked material. (d) A relatively sharp crack with no adjacent comminution.

concentrated patch of dye penetrant. The nature of the damaged region was elucidated from examinations of polished cross-sections in a scanning electron microscope (SEM). Representative images are shown in Figure 4. These confirm that the region of high penetrant concentration is indeed due to comminution. That is, despite the polishing, the images reveal (unpolished) granules with dimensions comparable to the grain diameter (3 μm). Virtually all grains are separated from their neighbors in this region. One consequence is that, upon polishing, the near surface grains are pulled out, exposing the underlying comminuted material.

Similar features are observed in the regions flanking some of the "wider" cone cracks. In the example shown in Figure 4c, the central region (about 50 μm wide) has been filled with epoxy during mounting. On either side of the crack, the material has been polished to some extent, although damage, in the form of grain pullout, is clearly evident. The present interpretation is that these regions represent *damage bands* that form in conjunction with the cone cracks. Precise definition of their boundaries and the extent of comminution within these bands is not possible using the present sectioning and polishing technique, largely because of the extreme friability of the damaged material coupled with incomplete infiltration of the supporting epoxy (especially if contiguous paths to the free surfaces are lacking). In other cases, such as that shown in Figure 4d, single dominant cracks are obtained without damage in adjacent material. These are reminiscent of cone cracks found under quasi-static loading conditions.

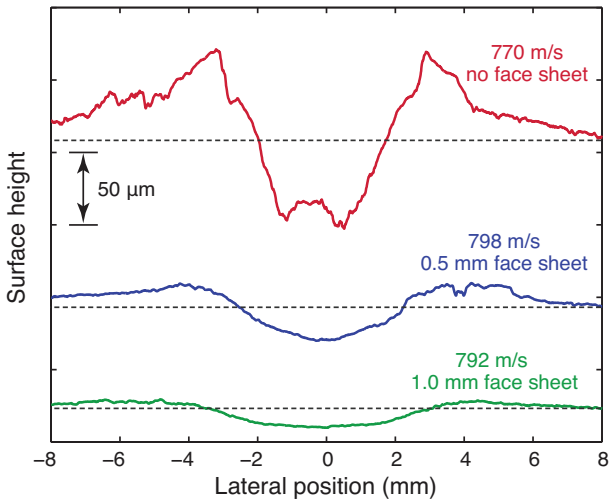

Figure 5. Surface profiles after impact. Dashed lines represent approximate locations of initial surfaces.

In the highest velocity range probed (750–800 m/s), the presence of a thin (0.5 or 1.0 mm) sheet on the impact face has two important effects. First, the size of the comminuted zone is significantly reduced. Indeed, for a sheet thickness of 1.0 mm, comminution is virtually non-existent (Figure 3f). However, there does not appear to be a significant change in the pattern of macroscopic radial and cone cracks (compare Figures 3d–3f). The second is a reduction in the depth of the crater produced upon impact. For instance, absent an outer sheet, the crater depth is 100 μm; for a 1 mm sheet, the depth is <20 μm (Figure 5). The benefits associated with the metal face sheet are addressed by finite element calculations presented in a subsequent section.

4. Numerical simulations of damage growth

A numerical analysis of damage evolution within the alumina tiles follows. The principal goal is to assess the capabilities and limitations of the Deshpande–Evans constitutive model for ceramics.

4.1. ***Finite element geometry.*** Axisymmetric finite element calculations of impact were performed using ABAQUS/Explicit V6.9-EF. The projectile was represented by a graded, unstructured quad mesh. The element sizes ranged from 180 μm (R/20) at the point of initial contact to roughly 700 μm (R/5) on the opposite side. This mesh was capable of accommodating the distortions in the projectile during impact without resorting to element deletion. The ceramic tile was meshed using structured quad elements, 60 μm on a side, over the entire area. Its diameter was selected to coincide with the width of the actual tiles (50 mm). The steel fixture was meshed using unstructured quad elements, nominally 350 μm in size (Figure 2b), with appropriate inner diameter (to match the test specimen geometry) and clamp dimensions (to match those in the experiments).

4.2. ***Constitutive laws for projectile and face sheet.*** The projectile and the face sheet were modeled using the von Mises yield criterion and the Johnson–Cook constitutive law for both strain and strain-rate

	projectile (304 steel)	face sheet (annealed 304 steel)		projectile (304 steel)	face sheet (annealed 304 steel)
A	1100 MPa	260 MPa	T_m	1800 K	1800 K
B	610 MPa	1350 MPa	T_0	300 K	300 K
n	0.4	0.62	c_p	450 J/kg K	450 J/kg K
m	0.82	1.0			
C	0.013	0.02	Inelastic heat fraction	0.9	0.9
$\dot{\epsilon}_0$	1.0	1.0			

Table 1. Johnson–Cook parameters for steels used in the finite element analyses.

hardening as well as thermal softening. The pertinent material parameter values are listed in Table 1. These parameters were obtained in part from a parallel investigation of the flow properties of 304 stainless steel sheet [unpublished data] as well as data reported in the literature [Stout and Follansbee 1986]. Additionally, both the projectile and the face sheets were assumed to be adiabatic during the impact, consistent with observations of heat tinting and some melting on recovered projectile fragments and face sheets.

To enable the computations to run to completion (up to and beyond projectile rebound), the large distortions in the face sheet (when used) were handled by assigning a large plastic failure strain ($\epsilon_{pl} = 4$) to this material and subsequently deleting the failed elements. Although the failure strain is selected somewhat arbitrarily, it has virtually no effect on the results presented here, since face sheet failure (regardless of whether the failure strain is selected to be 1 or 4) does not initiate until long after the damage within the ceramic has reached its terminal state.

4.3. *Constitutive law for ceramic.*

Model description. The alumina in the simulations is represented by the extended Deshpande–Evans (DE) constitutive model. Explicit formulations are presented in [Deshpande et al. 2011]. The model accounts for three inelastic deformation mechanisms.

Lattice plasticity is described by standard power law relations between equivalent stress, plastic strain and strain rate. The key material properties are the initial yield stress, σ_Y, the strain hardening exponent, M, the reference strain rate, $\dot{\epsilon}_0$, the strain rate sensitivity exponent, n, and the transition strain rate, $\dot{\epsilon}_t$, at which dislocation velocity becomes limited by phonon drag.

Distributed microcracking is described by a generalization of Ashby and Hallam's model for wing crack extension under compressive stress states [Ashby and Hallam 1986]. Two non-dimensional parameters characterize the initial damage state: the initial flaw size, $g_1 \equiv a_0/d$, and the flaw spacing, $g_2 \equiv s/d = (f^{1/3}d)^{-1}$ where d is the average grain size, s is the flaw spacing and f is the number of flaws per unit volume. Three behavioral regimes are obtained, delineated by the stress triaxiality, $\lambda \equiv \sigma_m/\sigma_e$ (σ_m being the mean stress). In Regime I, pre-existing cracks are closed and the shear stress is insufficient to overcome the frictional resistance of the contacting crack surfaces. Consequently, the mode I crack tip stress intensity is zero and crack growth cannot occur. This behavior is obtained when the stress triaxiality is less than a critical value, λ_C: dictated largely by the friction coefficient, μ, of the crack surfaces and the current level of microcrack damage. For friction coefficients typical of engineering ceramics, $\lambda_C \approx -0.5$ to -1. At higher triaxialities, in Regime II, the crack surfaces remain in contact

but are able to slide past one another. Sliding leads to a finite stress intensity which drives the formation of wing cracks at the tips of existing flaws. The cracks extend, initially stably, and eventually link to produce a fully comminuted ceramic. Following [Aeberli and Rawlings 1983], the crack growth rate is taken to scale with $(K_I/K_{IC})^m$ where $m \approx 30$. The crack growth rate is further restricted from exceeding the shear wave speed of the uncracked material. In Regime III, at yet higher triaxialities, the cracks are open and thus behave as Griffith-type defects.

The competition between microcracking and plasticity — as manifested in the relative positions of the yield surface and the damage initiation surface in stress space — is set by the ductility parameter, Δ, defined by (see [Horii and Nemat-Nasser 1986])

$$\Delta \equiv \frac{K_{IC}}{\sigma_Y \sqrt{\pi a_0}} = \frac{K_{IC}}{\sigma_Y \sqrt{\pi g_1 d}}. \tag{1}$$

One implication is that, for constant yield strength, the same damage behavior would be expected for combinations of fracture toughness and flaw size for which $K_{IC}/\sqrt{a_0}$ is constant.

Following crack coalescence, *granular flow* can occur by rotation and sliding of the resulting comminuted particles. Granular flow is taken to obey the linear Drucker–Prager yield criterion, characterized by a critical strength σ_e^{cr} at $\sigma_m = 0$ and a friction angle ω, and with a linear plastic potential, characterized by a dilation angle, ψ. Associated flow is obtained by setting $\psi = \omega$, whereupon the plastic strain exhibits significant dilation. At the other extreme, where $\psi = 0$, the granular plastic strain is purely deviatoric.

Calibration procedure. Calibration of the DE model was performed in the following way. Where possible, input parameters were taken or inferred from direct measurement. For example, density was measured using the Archimedes method, the elastic modulus was calculated from ultrasonic wave speed measurements [Denzel 2010], and plasticity parameters were taken from previously reported quasi-static indentation tests and associated numerical analyses [Gamble et al. 2011]. Tensile (fracture) properties were calibrated to the measured biaxial flexure strength, $\sigma_f = 355 \pm 12$ MPa (J. Shaw and M. Rossol, private communication). Confirmation of the selected plastic properties ($M = 0.1$, $n = 34$, σ_Y=5.75 GPa) was accomplished by comparing numerical simulations to the results of a series of 1D plate impact experiments reported in [Denzel 2010]. Comparisons between computed and measured particle velocities U_P for plate impact are shown in Figure 6. Also shown are the results of parametric studies of the effect of the hardening and rate sensitivity exponents. Using the yield strength and hardening values inferred from quasi-static indentation and a linear pressure-density relationship, the experimental particle velocity traces and Hugoniot elastic limit (HEL) are reproduced remarkably well. Further details on the shock response are presented [Denzel 2010].

For parameters not amenable to direct measurement or inference, a narrow range of realistic values was identified and parameter sensitivity studies were conducted at one impact velocity (750 m/s, no face sheet). For instance, the mode I long-crack fracture toughness of the alumina of present interest is 2.9 MPa$\sqrt{\text{m}}$. However, since the microcracks that form beneath the indent are inherently short and generally experience combined mode I/II loading, the pertinent toughness may differ somewhat from this value. To cover the range of realistic possibilities, the fracture toughness values investigated in the present computations span the range 2.5 to 3.5 MPa$\sqrt{\text{m}}$. A realistic range for the initial flaw size a_0 for microcracking is identifiable as well. Assuming the existence of flaws on grain boundary facets, the flaw size is $g_1 \equiv a_0/d \approx 1/4$. Alternatively, if flaws are initiated by slip within the grains, the flaw size is

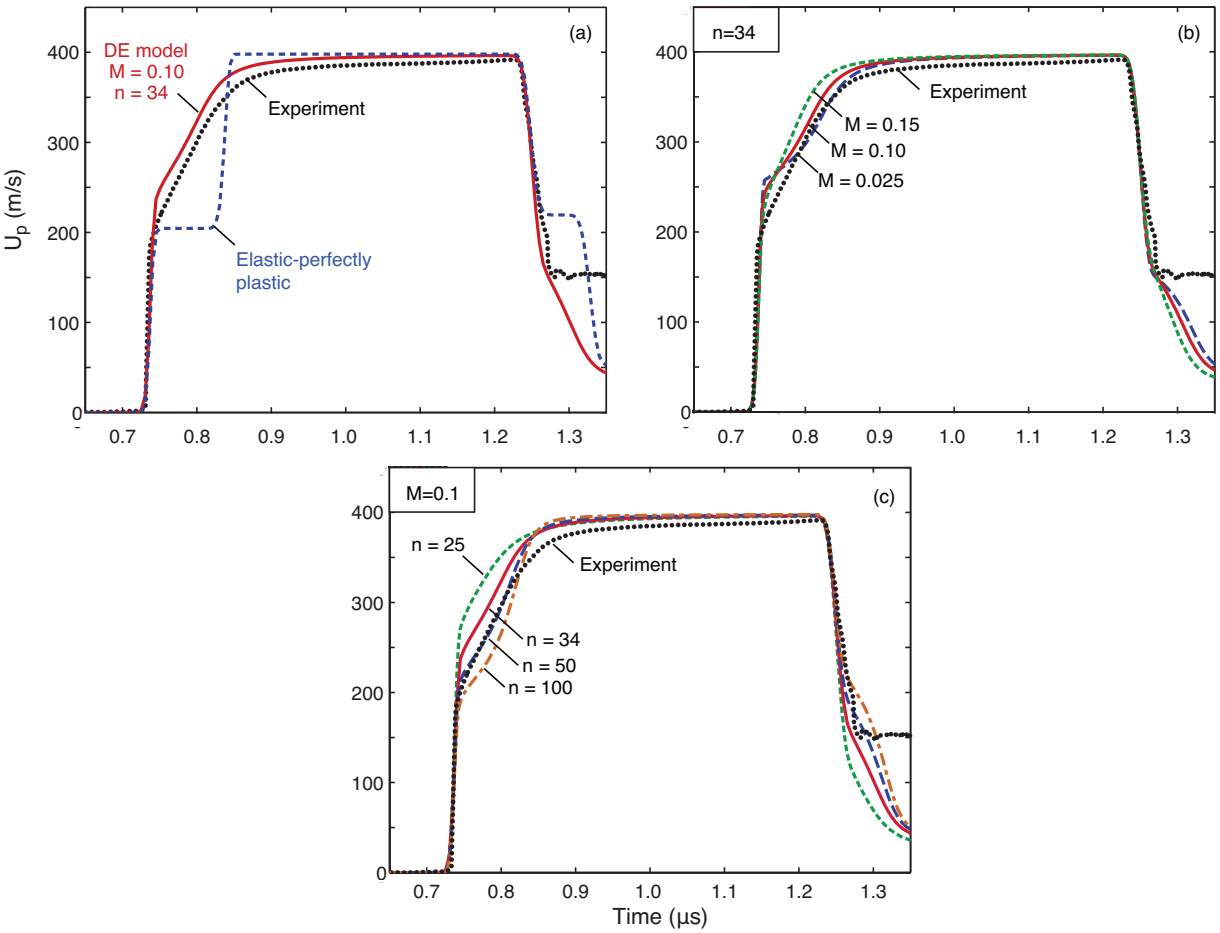

Figure 6. Experimental measurements of the one-dimensional shock loading response of alumina and effects of strain hardening and strain rate hardening in the predicted response from the DE model.

$g_1 \approx \frac{1}{2}$. Thus the range of interest for the computations is expected to be bounded approximately by $\frac{1}{4} \le g_1 \le \frac{1}{2}$. The flaw spacing parameter, g_2, and dilation angle, ψ, are more difficult to estimate *a priori*. But, as demonstrated below, the computed results are insensitive to their values over a rather broad range ($3 \le g_2 \le 12$, $0 \le \psi \le 35°$).

The results of the parametric studies used for model calibration (for an impact velocity of 750 m/s, without a face sheet) are shown in Figures 7 and 8. Comparisons with observed damage patterns through transverse cross-sections show that a reasonably good match is achieved for a fracture toughness $K_{IC} = 3\,\mathrm{MPa}\sqrt{\mathrm{m}}$ and a flaw spacing $g_1 = \frac{1}{2}$: both falling within their respective expected ranges. They also confirm the insensitivity of the damage patterns to flaw spacing, g_2, and dilation angle, ψ, over the range $0 \le \psi \le 35°$. Similar insensitivity was found in an earlier study on quasi-static indentation [Gamble et al. 2011]. All subsequent numerical simulations utilize $g_2 = 6$ and $\psi = 0°$. These and other material parameter values employed in the subsequent simulations are summarized in Table 2.

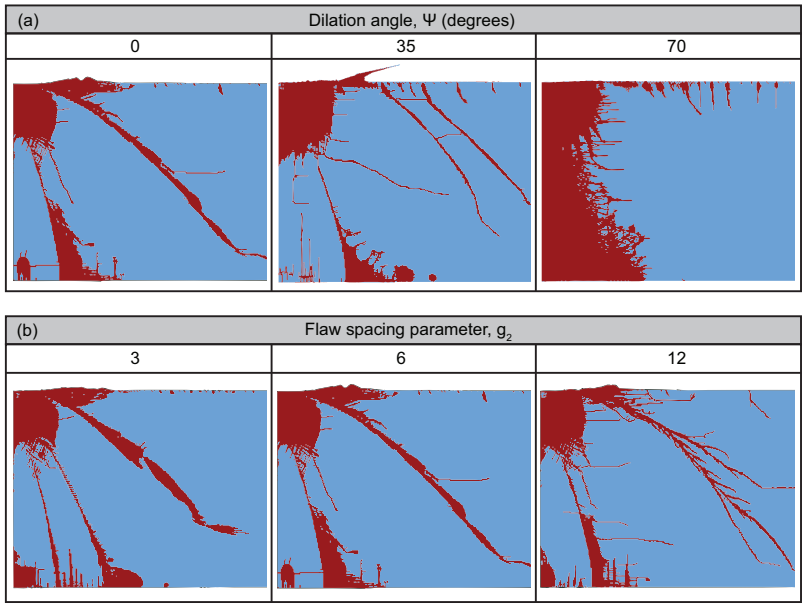

Figure 7. Effects of (a) dilation angle and (b) flaw spacing on damage zone for impact at 750 m/s.

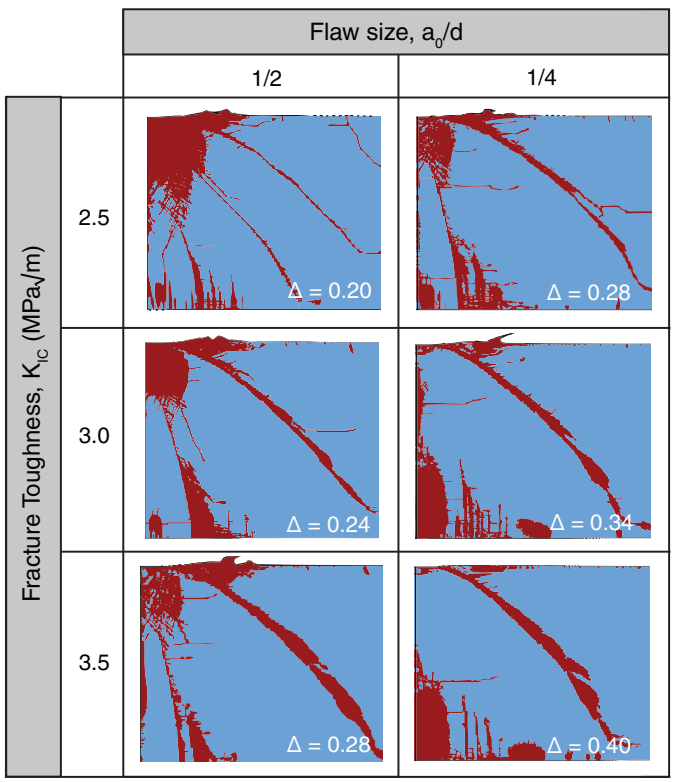

Figure 8. Effect of fracture toughness and flaw size as well as ductility parameter, Δ, on the predicted damage zone size in alumina impacted at 750 m/s.

Parameter	selected value	range considered
Density, ρ (kg/m^3)	3864	
Poisson's ratio, ν	0.239	
Young's modulus, E (GPa)	366	
Grain diameter,d (μm)	3.0	
Yield stress, σ_Y (GPa)	5.75	
Fracture toughness, K_{IC} (MPa$\sqrt{\text{m}}$)	3.0	2.5–3.5
Strain hardening exponent, M	0.1	0.025–0.15
Crack growth rate sensitivity exponent, m	30	
Strain rate dependence exponent, n	34	25–500
Reference crack growth rate, $\dot{l}_0$ (m/s)	0.01	
Reference strain, ϵ_0	0.002	
Reference plastic strain rate, $\dot{\epsilon}_0$ (1/s)	0.001	
Normalized flaw size, g_1	0.5	0.25, 0.5
Normalized flaw spacing, g_2	6	3–12
Crack geometry factor, γ	6	4–8
Crack coefficient of friction, μ	0.75	
Transition shear strain rate, $\dot{\epsilon}_t$ (1/s)	10^6	
Soil friction angle, ω	70°	
Soil uniaxial compressive strength, σ_C (MPa)	1	
Soil transition exponent, χ_d	5	
Soil transition strain rate, $\dot{\epsilon}_{\text{cut-off}}$ (1/s)	$2 \cdot 10^6$	
Dilation angle, ψ	0°	0°–70°

Table 2. Summary of alumina property data used in the extended DE model.

4.4. ***Numerical results.*** Using the material parameter set ascertained from the preceding calibrations, additional simulations were performed over a velocity range corresponding to that in the experiments. Comparisons of subsurface damage zones for direct impact are presented in Figure 9. Effects of the metal face sheet are shown in Figure 10. The numerical predictions match experimental observations remarkably well over the entire range of impact velocities and loading conditions investigated. Notably, they capture the general features of the size of the comminuted region directly beneath the impact, the formation of conical damage bands emanating from the impact site, and the damage that emanates from the back face as a result of stress wave reflections and/or bending at the tile/fixture interface. They also correctly capture the reduction in the size of the comminuted zone with the addition of metal sheets on the impact face. Indeed, for a 1 mm thick face sheet, the simulations correctly predict that no comminution occurs directly beneath the impact site.

The results from the numerical simulations have also been analyzed to enable improved understanding of contact pressure and force history as well as the damage evolution process. Representative results, for $V_0 = 750$ m/s, are plotted in Figures 11–13. Absent a face sheet, the maximum contact pressure occurs

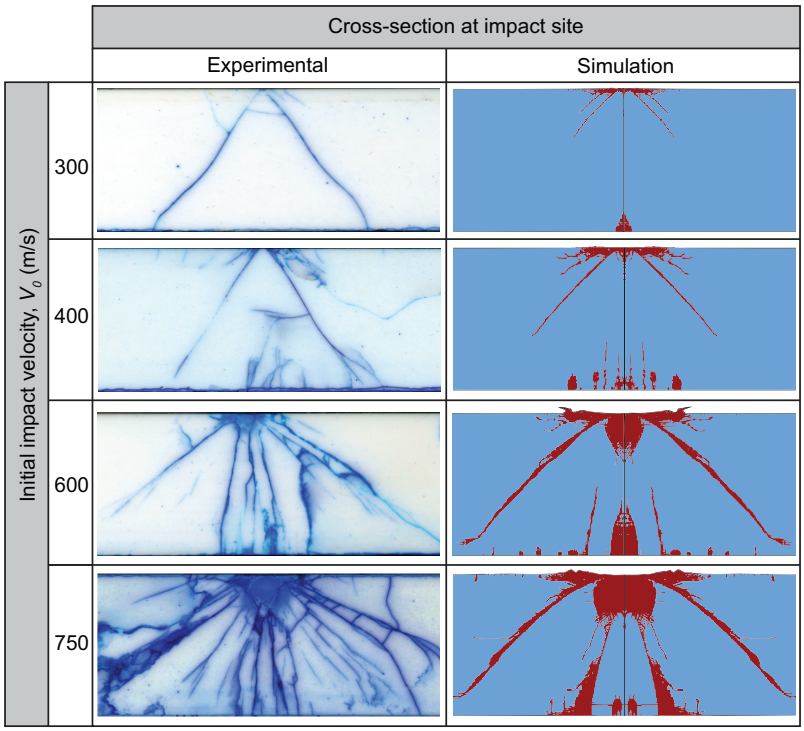

Figure 9. Computed and observed damage patterns. Computed results taken at 17 ms from first contact (immediately after projectile rebound). Experimental impact velocities are within ±20 m/s of the indicated velocity.

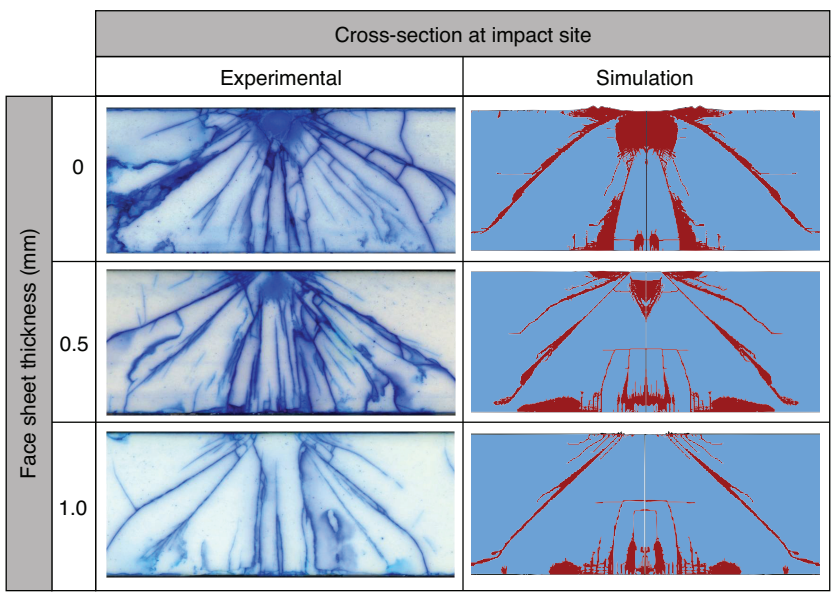

Figure 10. Effects of face sheet thickness on computed and observed damage patterns for impact velocity of 750±20 m/s. Computed results taken at 17 μs after first contact.

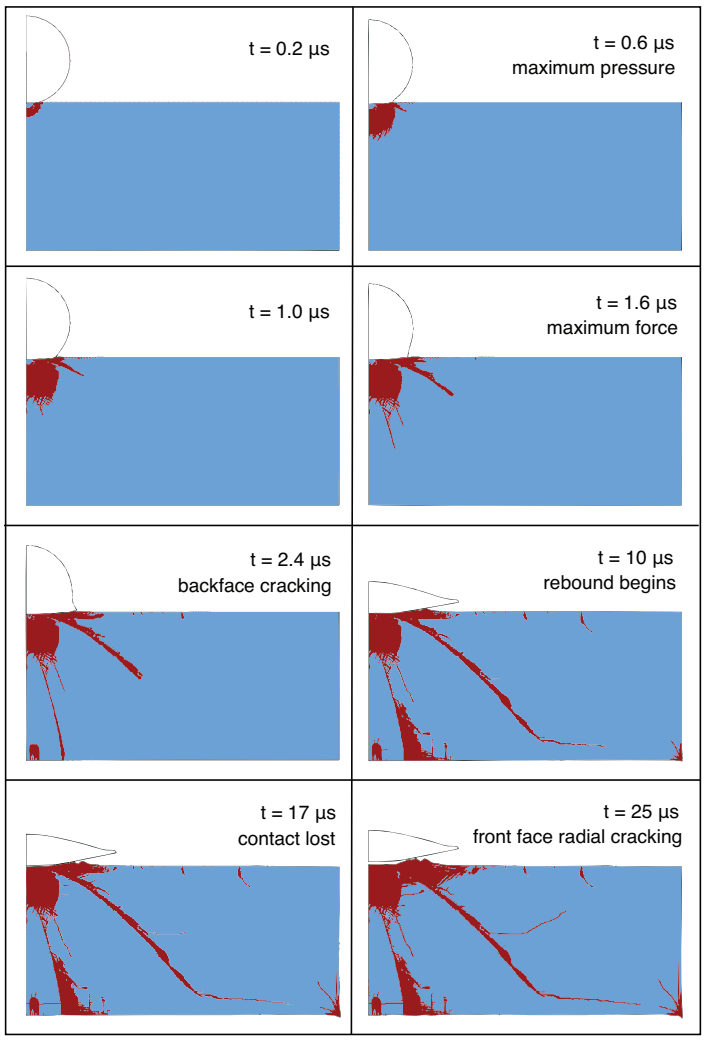

Figure 11. Progression of damage with time after impact for impact velocity of 750 m/s.

very shortly after impact ($< 1\ \mu$s). The pressure then drops quickly, reaching half its peak value within $2\ \mu$s. The corresponding sequence of damage events falls into three time domains.

(1) At short times (comparable to that at peak pressure), the damage zone grows in a roughly hemispherical pattern at the impact site. As the contact pressure falls and the magnitude of the stress waves in the ceramic is diminished, the conditions for further microcracking are no longer met and the damage ceases. For the example in Figure 11, the critical time for the latter event is about $1.6\ \mu$s after impact.

(2) Thereafter, while the pressure drops, the total contact *force* continues to rise. During this time, damage bands in an approximately conical configuration emanate from the intense damage zone directly beneath the impact. In addition, damage, representative of radial cracking, initiates at the

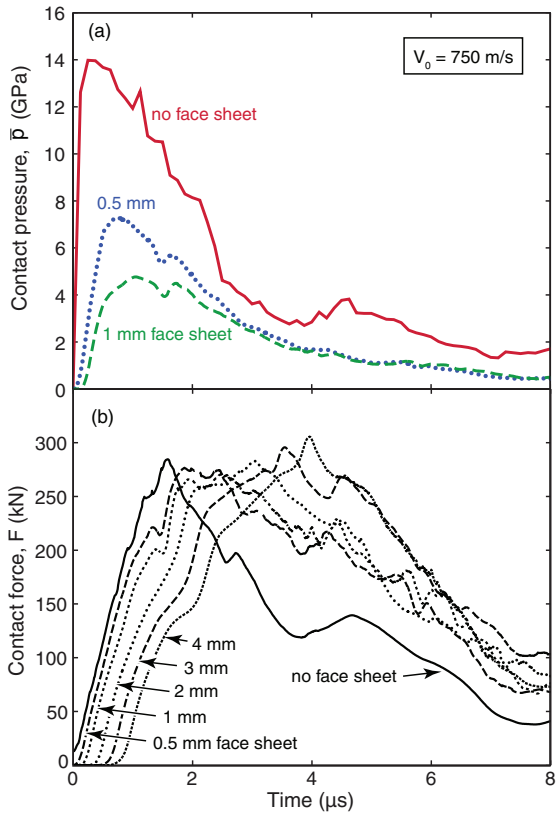

Figure 12. Effects of face sheets on histories of (a) average contact pressure and (b) contact force.

tile backface and grows upwards through the tile. Then, once the projectile begins to rebound, the contact force diminishes and the damage evolution process once again seemingly ceases.

(3) In the final stage, the ceramic tile itself undergoes a form of rebound, placing the impacted surface (and most importantly the damaged zone) into a state of biaxial tension. Damage growth then resumes at this location. In the present example, this event occurs about 17 μs after impact. It should be noted that the prediction of damage in this stage may be an artifact of the axisymmetric nature of the model. That is, in reality, the hoop stresses could be relieved by radial cracking rather than further diffuse damage growth. Indeed, such cracking is observed in the tiles tested in the high velocity domain. This feature, however, cannot be captured by the present (axisymmetric) model.

The role of a metal face sheet is illustrated in Figure 12. Its main effect is to increase the effective contact area on the top surface of the ceramic (at the interface with the face sheet) and hence lower the contact pressure (Figure 12a). Plots of the local contact pressure distribution on the ceramic surface at various times during the impact confirm this (Figure 13). In turn, the predicted size of the damage zone diminishes. The experimental results provide confirmation of this effect. The reduced pressure also leads to reduced plasticity and hence a shallower impact crater, as shown in Figure 5.

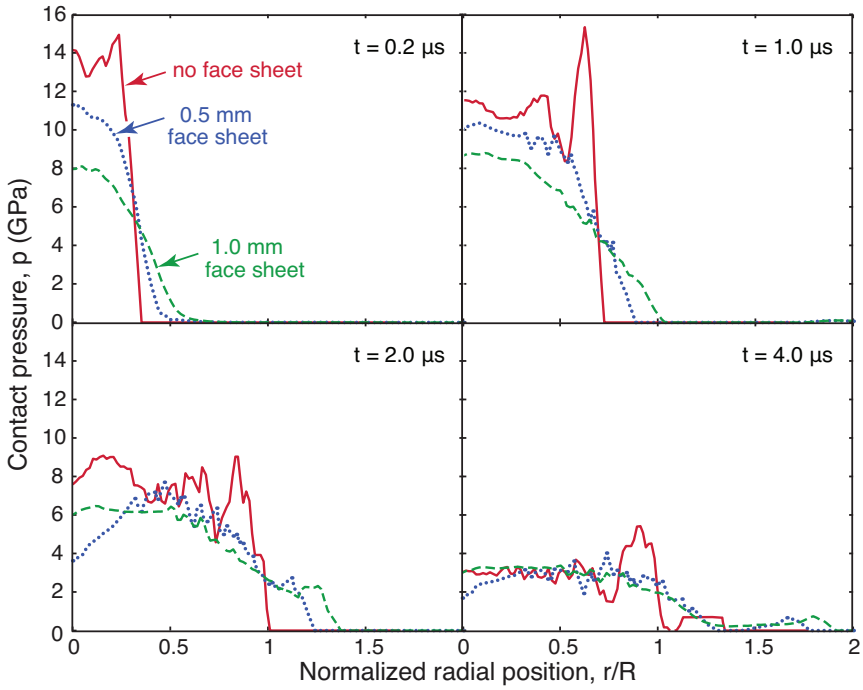

Figure 13. Contact pressure distributions at various times after impact. Impact velocity is 750 m/s. Time is measured from the instant that stresses reach the ceramic surface.

The finite element results further show that the face sheet does *not* significantly affect the maximum force imparted to the ceramic (Figure 12b). This result, along with the experimental observation that face sheets do not affect the degree of back-face radial cracking (Figure 3), strongly suggests that such cracking is dictated predominantly by the maximum contact force, as opposed to the contact pressure. This is supported by the results of a recent numerical study [Compton et al. 2011], demonstrating that the maximum back-face hoop stress in a supported tile under impact loading is essentially the same as that obtained under quasi-static loading at the same contact force.

5. Summary and conclusions

The material parameters in the extended Deshpande–Evans constitutive model have been calibrated for an armor alumina through a combination of independent property measurements, judicious selection of parameter ranges when direct measurement is not feasible, and comparisons of parametric numerical studies with experimental measurements and observations. The model has been shown to predict reasonably accurately the variation in the size of the comminuted zone beneath the impact site with impact velocity as well as secondary damage processes such as those manifested as cone and radial cracks. The evolution of damage and cracking has been explained in terms of the contact pressure and force evolution throughout the impact: the microcrack damage zone develops with the contact pressure, while the secondary cracking develops with the contact force and structural rebound of the tile. The numerical simulations have also provided new insights into the role of metal face sheets on the damage processes.

Specifically, these sheets aid in distributing the load over a larger area in the early stages of impact, when the peak contact pressures are attained, and thus reduce the propensity for microcracking as well as lattice plasticity. But, for the thicknesses employed here, they do not significantly affect the peak contact force transmitted to the underlying ceramic tile and thus have no apparent effect on the degree of radial and cone cracking. The expectation is that, for larger values of normalized sheet thickness, h/R, the latter processes may be affected.

In its present implementation, the model is restricted to 2D loadings and is thus unable to capture features that break radial symmetry. Most notably, it cannot predict the radial cracks that occur on both the impacted face and the back face. This deficiency has been mitigated recently through the implementation of a 3D version of the constitutive model by Radovitzky and co-workers for use in 3D simulations (R. Radovitzy, private communication). The latter simulations do indeed predict the formation of radial cracks during an impact event. The results of that study will be reported elsewhere.

Acknowledgements

Support from the Office of Naval Research through a Multidisciplinary University Research Initiative Program on "Cellular Materials Concepts for Force Protection," Prime Award No. N00014-07-1-0764, is gratefully acknowledged. EAG was supported by a National Defense Science and Engineering Graduate Fellowship.

References

[Aeberli and Rawlings 1983] K. E. Aeberli and R. D. Rawlings, "Effect of simulated body environments on crack propagation in alumina", *J. Mater. Sci. Lett.* **2**:5 (1983), 215–220.

[Ashby and Hallam 1986] M. F. Ashby and S. D. Hallam, "The failure of brittle solids containing small cracks under compressive stress states", *Acta Metall.* **34**:3 (1986), 497–510.

[Ashby and Sammis 1990] M. F. Ashby and C. G. Sammis, "The damage mechanics of brittle solids in compression", *Pure Appl. Geophys.* **133**:3 (1990), 489–521.

[Chantikul et al. 1990] P. Chantikul, S. J. Bennison, and B. R. Lawn, "Role of grain size in the strength and R-curve properties of alumina", *J. Am. Ceram. Soc.* **73**:8 (1990), 2419–2427.

[Compton et al. 2011] B. G. Compton, E. A. Gamble, and F. W. Zok, "Failure initiation during impact of metal spheres onto ceramic targets", 2011. Submitted to *Int. J. Impact Eng.*

[Denzel 2010] J. R. Denzel, "Determination of shock properties of ceramic corbit 98: 98% alumina", Master's thesis, Naval Postgraduate School, Monterey, CA, June 2010, Available at http://hdl.handle.net/10945/5312.

[Deshpande et al. 2011] V. S. Deshpande, E. A. N. Gamble, B. G. Compton, R. M. McMeeking, A. G. Evans, and F. W. Zok, "A constitutive description of the inelastic response of ceramics", *J. Am. Ceram. Soc.* **94**:S1 (2011), 204–214.

[Gamble et al. 2011] E. A. Gamble, B. G. Compton, V. S. Deshpande, A. G. Evans, and F. W. Zok, "Damage development in an armor ceramic under quasi-static indentation", *J. Am. Ceram. Soc.* **94**:S1 (2011), 215–225.

[Horii and Nemat-Nasser 1986] H. Horii and S. Nemat-Nasser, "Brittle failure in compression: splitting, faulting and brittle-ductile transition", *Phil. Trans. R. Soc. A* **319**:1549 (1986), 337–374.

[Longy and Cagnoux 1989] F. Longy and J. Cagnoux, "Plasticity and microcracking in shock-loaded alumina", *J. Am. Ceram. Soc.* **72**:6 (1989), 971–979.

[Rhee et al. 2001] Y.-W. Rhee, H.-W. Kim, Y. Deng, and B. R. Lawn, "Brittle fracture versus quasi plasticity in ceramics: a simple predictive index", *J. Am. Ceram. Soc.* **84**:3 (2001), 561–565.

[Shih et al. 2000] C. Shih, M. A. Meyers, V. F. Nesterenko, and S. J. Chen, "Damage evolution in dynamic deformation of silicon carbide", *Acta Mater.* **48**:9 (2000), 2399–2420.

[Stout and Follansbee 1986] M. G. Stout and P. S. Follansbee, "Strain rate sensitivity, strain hardening, and yield behavior of 304L stainless steel", *J. Eng. Mater. Technol.* (*ASME*) **108**:4 (1986), 344–353.

Received 27 Feb 2012. Accepted 16 Mar 2012.

BRETT G. COMPTON: bcompton@engineering.ucsb.edu
Materials Department, University of California, Santa Barbara CA 93106-5050, United States

ELEANOR A. GAMBLE: nell.gamble@gmail.com
Materials Department, University of California, Santa Barbara CA 93106-5050, United States

VIKRAM S. DESHPANDE: vsd@eng.cam.ac.uk
Engineering Department, Cambridge University, Trumpington Street, Cambridge, CB2 1PZ, United Kingdom

FRANK W. ZOK: zok@engineering.ucsb.edu
Materials Department, University of California, Santa Barbara, Santa Barbara CA 93106-5050, United States
http://engineering.ucsb.edu/~zok/zok.html

JOURNAL OF MECHANICS OF MATERIALS AND STRUCTURES
Vol. 7, No. 6, 2012
dx.doi.org/10.2140/jomms.2012.7.593

AN ASYMPTOTIC METHOD FOR THE PREDICTION OF THE ANISOTROPIC EFFECTIVE ELASTIC PROPERTIES OF THE CORTICAL VEIN: SUPERIOR SAGITTAL SINUS JUNCTION EMBEDDED WITHIN A HOMOGENIZED CELL ELEMENT

RANIA ABDEL RAHMAN, DANIEL GEORGE, DANIEL BAUMGARTNER, MATHIEU NIERENBERGER, YVES RÉMOND AND SAÏD AHZI

Bridging veins (BVs) are frequently damaged in traumatic brain injury due to brain-skull relative motion. These veins, connected to the superior sagittal sinus (SSS), are prone to rupture upon head impact giving rise to an acute subdural hematoma (ASDH). We modeled the biomechanical characteristics of ASDH to study the behavior of the SSS-BVs compound with its surrounding medium. The almost periodic distribution of the BVs along the SSS allowed the use of the homogenization method based on asymptotic expansion to calculate the effective elastic properties of the brain-skull interface region. The representative volume element (RVE) under study is an anisotropic equivalent medium with homogenized elastic properties, accounting for the variations of each constituent's mechanical properties. It includes the sinus, the BVs and blood, and the surrounding cerebrospinal fluid and tissue. The results show large variations in the RVE anisotropic properties depending on each constituent of the BV and, to a certain extent, on the variability of the surrounding constituents' mechanical properties.

1. Introduction

Acute subdural hematoma (ASDH) is a potentially devastating, yet curable extra-axial fluid collection within the potential subdural space. It is classically associated with head trauma rising from rapid acceleration and/or deceleration that produces the rupture of cortical arteries and most often occurs by tearing of bridging veins (BVs) as they cross from the brain surface to the dural sinus [Maxeiner and Wolff 2002]. Fenderson et al. [2007] reported that these veins are prone to rupture at the point of their entry into the SSS, and this was confirmed by the results of microscopy examination [Yamashima and Friede 1984; Vignes et al. 2007]. They found that, due to the histological composition of the BVs and the change in the collagen pattern in the vein walls near their entrance into the superior sagittal sinus (SSS), the subdural portion of a BV is more fragile than its subarachnoidal portion. The rupture of BVs is induced by the brain-skull relative motion following a head impact as described by neuropathologists [Yamashima and Friede 1984] and by experimental work conducted in vivo [Willinger et al. 1995; Ji et al. 2004; Bayly et al. 2005; Ji and Margulies 2007; Sabet et al. 2008].

The motion between the brain and the skull has been considered potentially important to head injury. In order to evaluate this potential problem, finite element (FE) modeling of the human head was developed to evaluate the brain-skull interface conditions [Kleiven and Hardy 2002; Wittek and Omori 2003]. An important issue in the numerical analysis is the selection of material properties. While there

Keywords: homogenization, mechanical behavior, bridging veins, brain-skull interface, elastic properties, biological material.

are several macroscopic FE models of the human head, only one local 3D FE model has been developed, by Moghadam and Sadegh [2009], to study the details of the brain-skull interface region to analyze the rupture of BVs. The use of classical finite element methods to find the local behavior at each point of a complicated biological structure such as the brain-skull interface region is very difficult. Thus, the use of homogenization methods at different scales is becoming unavoidable. Different authors have used multiscale approaches [Sanz-Herrera et al. 2009; Bertaud et al. 2010; Soliman et al. 2010] to define the mechanical behavior of biological tissue. The finite element approach has been adopted by Karami et al. [2009] to analyze the homogenized mechanical response of brain white matter under large deformation. Yoon et al. [2002] estimated the effective transversely isotropic elastic constants of bones from orthotropic data found in the literature. The aim of the present work is to analytically determine the homogenized mechanical properties of the segment representing the junction between the SSS, the BV, and the surrounding constituents. This zone will be considered as a heterogeneous medium which will be transformed to a mechanically equivalent medium (effective medium) that is anisotropic and homogeneous. In turn, this equivalent medium can be incorporated as a heterogeneous element in a macroscopic model, such as FEM.

The calculations are conducted on a representative volume element (RVE) of the size order of the BV. To achieve this goal, the anatomy, the geometrical arrangement, and the mechanical properties of the tissues forming the investigated segment must be adequately defined. In addition, in order to be able to include this analysis in a macroscopic model of the head, the geometry and size of the RVE should be able to fulfill the following two requirements: first, have a similar size and geometry as the local geometrical element present in the macroscopic model, and second, be able to take into account the local microscopic heterogeneous medium of the BV and surroundings in order to provide an accurate anisotropic heterogeneous behavior. These constraints are strong and influence the results of the analysis. Nevertheless, this work will enable us to make a first evaluation of the elastic behavior of BVs, which is carried out on the local level using a micromechanical approach. This paper presents the geometrical model development together with theoretical analysis. The results are given for the anisotropic behavior of the RVE at the macroscopic scale. The variations of these results are discussed as a function of the local constituents' behavior and the surrounding environment.

2. Materials description

2.1. ***Geometry localization and material properties.*** Figure 1 shows the distribution and positioning of the anisotropic RVE along the SSS in order to take into account the BVs' specific behavior. We assumed that the homogenized cell follows the SSS main axis with a perpendicular BV attached to it. This cell will represent the RVE for which the homogenization method will be applied.

It is always difficult to precisely characterize the mechanical response of biological tissue and especially soft tissue. The local geometries and material properties for the RVE's local constituent were extracted from [Yamashima and Friede 1984; Lee and Haut 1989; Henrikson et al. 1997; Kleiven 2002; Bashkatov et al. 2003; Horgan 2005] for the dimensions and [Melvin et al. 1970; Ruan et al. 1993; Huang et al. 1999; Willinger et al. 1999; Monson et al. 2005] for the mechanical properties. All the materials in the current study were supposed linear elastic in a first approximation. The chosen geometry and corresponding mechanical properties for the SSS and BVs are presented in Table 1. In this table,

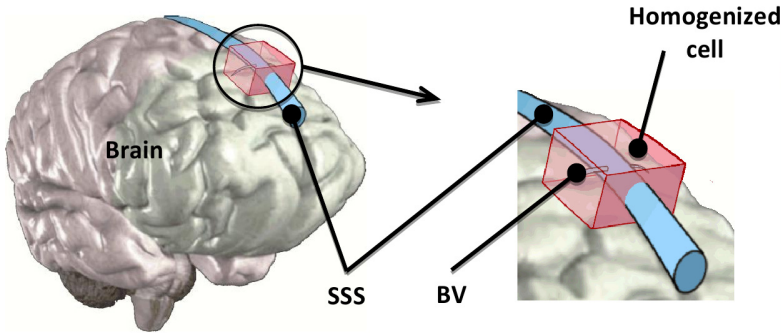

Figure 1. Schematic positioning of the anisotropic RVE as a part of the macroscopic model of the head.

E_l and E_t represent the longitudinal (relative to the BV's main axis) and transverse Young's moduli, respectively, and ν_{lt} and ν_{tt} are the corresponding Poisson's coefficients. Apart from the wall thickness and diameter of the blood vessels, other dimensions are irrelevant in our study since they depend on the size of the used homogenized cell and are accounted for in the homogenization method.

Some work was carried out on the brain and surrounding tissue such as in [Pham and Sun 2010; Prevost et al. 2011a; 2011b]. In these works, the investigated volume represents the brain-skull interface region (BSIR) in the zone of the junction of the BVs with the SSS walls. This volume is a complex zone mostly filled with liquid and comprises the sinus, the bridging veins, the blood circulating inside them, and the surrounding cerebrospinal fluid and tissues. An experimental study using modal analysis of the head in vivo was conducted by Willinger and Césari [1990; 1995; 1999] on the dynamic behavior of the brain-skull interface. This study was based on a hammer impact method on the head. It showed that for so-called long shocks in the range 0.012 to 0.025 ms, the shock spectrum energy is distributed in a frequency range below 150 Hz and the brain follows the movement of the head. On the contrary, for so-called short impacts in the range 0.004 to 0.012 ms, the shock spectrum is distributed in a frequency range above 150 Hz, the brain no longer follows the skull movement, and relative displacement occurs between the brain and the skull. This experimental work coupled with an FEM modal analysis using springs and dashpots based on rheological models enabled the evaluation of an equivalent stiffness of the BSIR zone, which was 0.012 MPa. It appears to be of the same order as the average stiffness values of the brain, measured between 0.07 MPa and 0.675 MPa [Ruan et al. 1991; Willinger et al. 1992; Kumaresan and Radhakrishnan 1996; Ruan and Prasad 1996; Sarkar et al. 2004]. However it is much smaller than the stiffness value of the skull, measured at 15 GPa for parietal bone and 4 GPa for the diploë [Willinger et al. 1999;

		Mechanical properties	
Tissue	Geometry (mm)	Young's modulus, E (MPa)	Poisson's ratio, ν
SSS	Wall thickness = 0.5	31.5	0.45
BVs	Diameter = 1.5	$E_l = 6.43$	$\nu_{lt} = 0.385$
	Wall thickness = 0.25	$E_t = 2.4$	$\nu_{tt} = 0.49$

Table 1. Geometry and mechanical properties of the studied tissues.

Ho and Kleiven 2007; Yao et al. 2008; Yu et al. 2008]. In the current work, we used this measured value (0.012 MPa) in our mechanical analysis for the BSIR and, in order to be consistent with a fluid-like mechanical behavior, we allocated a Poisson's ratio of 0.49. The thickness of the BSIR included in the RVE was 1.5 mm. The mechanical behavior of the blood inside the BVs poses a similar problem as the mechanical behavior of the BSIR between the brain and skull, although it is enclosed within the BVs' or SSS's walls. However, the BVs' walls are of different stiffness than those of the brain and skull. Therefore, the stiffness response of the blood inside the BVs is different from its response between the brain and skull. In order to take this into account in our analysis, we made a parametric study of the influence of blood properties on the overall mechanical behavior of the RVE. This will be presented in the results section.

The average reported viscosity of the blood ($\mu_{\mathrm{bl,av}} = 0.004$ Pa·s [Chatziprodromou et al. 2007; Li et al. 2007]) is situated in between that of water ($\mu_{\mathrm{water}} = 0.001$ Pa·s) and that of the BSIR ($\mu_{\mathrm{BSIR}} = 0.0085$ Pa·s [Bloomfield et al. 1998]). For an average strain rate under the given loading conditions of about $10\,\mathrm{s}^{-1}$ for the BVs (depending on their length and loading time), the stresses developed due to viscosity are very small (typically of the order of 0.01 Pa) compared to other stresses developed by the harder materials of the RVE under the same mechanical loads. Therefore we can assume that the stresses developed by the viscosity of the blood inside the RVE will be of the same order of magnitude as that of the BSIR at the brain-skull interface. In the current work, the studied range of blood properties was varied between 0.012 MPa (equivalent to that of the BSIR from Willinger and Césari [1990; 1995; 1999]) and 1 MPa, which is about half the stiffness value of the BV walls. We believe this range of study is large enough to validate our model and determine accurately the anisotropic behavior of the RVE in the range of the applied mechanical loads. For convenience, we named the equivalent stiffness of the blood (K_{bl}) and in the same way as for the BSIR mechanical characteristics, we allocated a Poisson's ratio of 0.49. Finally, the value of the elastic modulus of the SSS (E_s) was varied from 30 to 60 MPa. These values were extracted from [Delye et al. 2006; Mukherjee et al. 2006] to cover an average range of values cited in the literature. The effect of variations in these parameters on the values of the RVE homogenized elasticity coefficients was also determined and is presented in the results section.

The BV was treated as an orthotropic material composed of collagen fibers of Young's modulus (E_c) = 1 GPa surrounded by a matrix formed of elastin of Young's modulus (E_{el}) = 0.6 MPa, as mentioned in [Park and Lakes 2007]. The collagen to elastin ratio was considered to be 3:1 as reported in [Samet and Lelkes 1999]. The transverse elastic modulus (E_t) and transverse Poisson's ratio (ν_{tt}) were calculated by considering a lower bound approach using a simple Reuss averaging scheme while the longitudinal elastic modulus (E_l) was chosen from [Monson et al. 2005]. The longitudinal Poisson's ratio (ν_{lt}) was obtained from the standard rule of mixture. Table 2 summarizes the elastic mechanical properties of the BV. In our analyses, the properties of the BV itself are kept constant since they are directly taken from data from the literature. Some patient-dependant variations are to be expected but it is believed that they will not influence greatly the anisotropic behavior of the considered RVE in this simple case. The muscle strength in the BVs was not taken into account in this work since their rigidity is very small (there are

Property	E_l (MPa)	E_t (MPa)	ν_{lt}	ν_{tt}	G_{tt} (MPa)	G_{lt} (MPa)
Value	6.43	2.4	0.385	0.49	0.8	0.8

Table 2. Elastic mechanical properties of the BV.

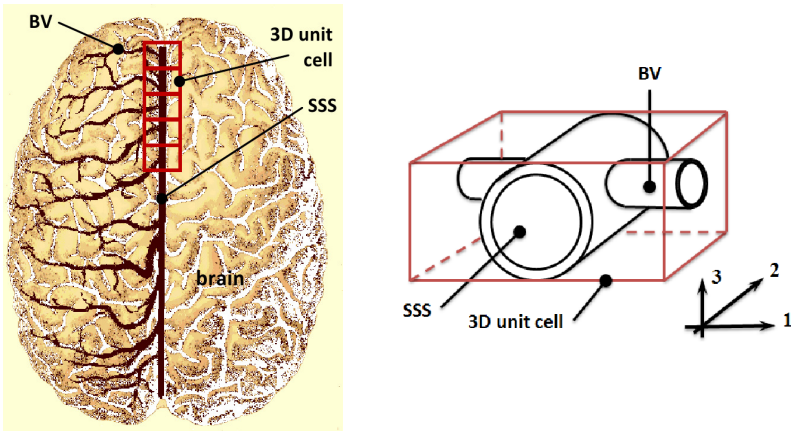

Figure 2. Left: distribution of BVs along the SSS as shown in [Rhoton 2002]. Right: a schematic of the RVE on the SSS-BV junction.

almost no muscles in the BVs due to their location and size). Therefore, the muscles have a negligible impact on the BVs' mechanical behavior compared to the rigidity of the collagen and elastin fibers.

The RVE is therefore composed of SSS, BV, blood, and BSIR components for which all mechanical characteristics are defined. Other tissues are not taken into account in this analysis since they are supposed to be outside the RVE.

2.2. ***Periodicity problem.*** BVs are fairly symmetrically distributed on both sides of the SSS and evenly distributed along the axis of the sinus in the sagittal plane as shown in Figure 2, left. Therefore we considered the distribution of BVs to be almost periodic in the sagittal direction and we applied the homogenization method based on the asymptotic expansion.

Figure 2, right, illustrates the SSS-BV junction. As explained previously, the investigation zone is defined as a geometrical 3D unit cell. This unit cell was chosen to be the representative volume element (RVE) used in the current micro-meso homogenization calculations. Note that the symmetrical distribution (or not) of the BVs on each side of the SSS is not relevant here since this is automatically taken into account in the asymptotic homogenization process.

3. Homogenization method by asymptotic expansion

3.1. ***Theory.*** We will present here the main steps of the method. Let L represent the characteristic dimension of the overall structure, then ηL will define the size of the RVE. We denote by X the slow variable reflecting the variation in the magnitude of the properties at the structure scale and by Y the local variable describing the rapid variation on the RVE. Thus, X and Y are related together through

$$\eta = \frac{X}{Y}. \tag{1}$$

If $\vec{U}(X, Y)$ is the displacement field, it may be expressed in terms of infinite expansion series, as proposed in [Sanchez-Palencia 1974; Ladeveze et al. 1985; Dumont et al. 1987; Devries et al. 1989]:

$$\vec{U}(X, Y) = \vec{U}_0(X, Y) + \eta\vec{U}_1(X, Y) + \eta^2\vec{U}_2(X, Y) + \cdots. \tag{2}$$

The elastic deformation written here in small deformations is decomposed as a function of slow and rapid variables (it can be developed for large deformation):

$$\epsilon_{ij} = \epsilon_{xij} + \frac{1}{\eta}\epsilon_{yij}, \tag{3}$$

where ϵ_x and ϵ_y are the strain tensors corresponding to the slow and rapid variables, respectively. Knowing that $\sigma = K\epsilon$ (Hooke's law), the stress differential operator $\operatorname{div}\sigma(X, Y)$ may be written as follows:

$$\operatorname{div} K\epsilon = \operatorname{div}_x K\epsilon + \frac{1}{\eta}\operatorname{div}_y K\epsilon, \tag{4}$$

where K represents the local elastic properties and div_x and div_y are the divergence operators corresponding to slow and rapid variables, respectively.

The equilibrium equation of the periodic medium is $\operatorname{div}\sigma(X, Y) + f = 0$ where f is the volume force. It induces

$$\operatorname{div}_y K\epsilon_y(\vec{U}_0) = 0, \tag{5}$$

$$\operatorname{div}_y K\epsilon_y(\vec{U}_1) + \operatorname{div}_y K\epsilon_x(\vec{U}_0) + \operatorname{div}_x K\epsilon_y(\vec{U}_0) = 0, \tag{6}$$

$$\operatorname{div}_y K\epsilon_y(\vec{U}_2) + \operatorname{div}_y K\epsilon_x(\vec{U}_1) + \operatorname{div}_x K\epsilon_y(\vec{U}_1) + \operatorname{div}_x K\epsilon_x(\vec{U}_0) + f = 0. \tag{7}$$

Solving (5), (6), and (7) gives $\vec{U}_0$, $\vec{U}_1$, and $\vec{U}_2$, which are the solutions of the following variational formulation:

$$\text{Find} \quad \vec{\vartheta} \in \vartheta_{\text{per}} / \forall \vec{\vartheta}^* \in \vartheta_{\text{per}}, \quad \int_M \operatorname{Tr}[K\epsilon_y(\vec{\vartheta})\epsilon_y(\vec{\vartheta}^*)]d\Omega = \int_M \overrightarrow{g.\vartheta^*} d\vec{\Omega}, \tag{8}$$

with $\vec{g} = -\operatorname{div}[K.\epsilon_y(\vec{U})]$ and $\vartheta_{\text{per}} = \vec{U}/U^+ = U^-$, where U^+ and U^- represent the values of $\vec{U}$ on 2 opposite faces of the RVE and are equal. M represents the unit cell (RVE) and $\int_{M^*} d\vec{\Omega} = V^*$, where V^* is the volume of the RVE. For more details, see [Mahmoud 2010, pp. 44–65].

From the solution of (5), (6), and (7) it can be concluded that

- $\vec{U}_0$ depends only on X: $\vec{U}_0 = \vec{U}_0(X)$.
- $\vec{U}_0$ and $\vec{U}_1$ are linearly dependent since

$$K_{ijkl}\epsilon_{ykl}(\vec{U}_1) = H_{ijkl}\epsilon_{xkl}(\vec{U}_0) \tag{9}$$

  where H is a symmetric linear operator.

The equilibrium equation of the periodic medium becomes

$$\operatorname{div}_x \int_M [(H + K)\epsilon_x(\vec{U}_0)]d\Omega + f\int_M d\Omega = 0. \tag{10}$$

Note that $\vec{U}_0$ represents the homogenized displacement over the RVE while $\vec{U}_1$ represents the perturbation of the displacement.

Finally, using the macroscopic (RVE) Hooke's law $\sigma^* = K^*\epsilon^*$, relating the macroscopic stress tensor σ^* to the macroscopic elastic strain tensor ϵ^*, along with (9) and (10) we get the homogenized behavior of the periodic medium. This leads to the following expression of the effective elastic stiffness tensor K^*:

$$K^*_{ijkl} = \frac{1}{\operatorname{vol}(M)}\int_M (H_{ijkl} + K_{ijkl})dM. \tag{11}$$

Moreover, we can express the problem in $\vec{U}_1$ as follows:

$$\vec{U} \to \frac{1}{2}\int_M K_{ijkl}\epsilon_{yij}(\vec{U})\epsilon_{ykl}(\vec{U})\,dM + \int_M K_{ijkl}\epsilon_{xij}(\vec{U}_0)\epsilon_{ykl}(\vec{U})\,dM. \tag{12}$$

Knowing that $\epsilon_y(\vec{U}_1)$ and $\epsilon_x(\vec{U}_0)$ are linearly dependent as shown in relation (9), we have $\vec{U}_1 = A_{rs}\epsilon_{rs}(\vec{U}_0)$ with $A_{rs} \in W(M)$. Thus the variational problem (12) is now as follows.

Find $A_{rs} \in W(M)$ by minimizing the following functions:

$$U \to \frac{1}{2}\int_M K_{ijkl}\epsilon_{yij}(\vec{U})\epsilon_{ykl}(\vec{U})\,dM + \int_M K_{rskl}\epsilon_{xij}(\vec{U}_0)\epsilon_{ykl}(\vec{U})\,dM, \tag{13}$$

$$K^*_{ijkl} = \frac{1}{\mathrm{vol}(M)}\int_M [K_{ijrs} + K_{ijkl}\epsilon_{kl}(\vec{U})]\,dM. \tag{14}$$

Here $W(M)$ is the displacement space, and (r, s) equals (1, 1), (2, 2), and (3, 3) in the case of normal loading and (1, 2), (2, 3), and (3, 1) in the case of shear loading.

3.2. ***Application to the representative volume element.*** Since the basic unit cell (RVE) is symmetric about the three orthogonal planes, we can develop the theory only on an eighth of the RVE. By making this simplification we assume that the periodicity is present in all directions, which is not the real case. This assumption can be justified since the results of the homogenization done in the current study were applied to estimate the global and local behaviors of the constituents of the brain-skull interface region only in the case of sagittal impacts. The anatomical periodicity being in the sagittal plane, the previous assumption is valid since no influence will be developed in other directions. In addition, the principle of our calculations is linear. It is simply transposed to the curvilinear structure of the head.

The different loading cases can be dissociated and the relations (13) and (14) are minimized on

$$W_0(M) = \left\{\vec{U}/U_1 = 0\big|_{0,L_1}; U_2 = 0\big|_{0,L_2}; U_3 = 0\big|_{0,L_3}\right\} \quad \text{for } r, s = (1,1), (2,2), (3,3), \tag{15}$$

$$W_1(M) = \left\{\vec{U}/U_1 = 0\big|_{0,L_1}; U_1 = U_3 = 0\big|_{0,L_2}; U_1 = U_2 = 0\big|_{0,L_3}\right\} \quad \text{for } r, s = (2,3), \tag{16}$$

$$W_2(M) = \left\{\vec{U}/U_2 = U_3 = 0\big|_{0,L_1}; U_2 = 0\big|_{0,L_2}; U_1 = U_2 = 0\big|_{0,L_3}\right\} \quad \text{for } r, s = (3,1), \tag{17}$$

$$W_3(M) = \left\{\vec{U}/U_2 = U_3 = 0\big|_{0,L_1}; U_1 = U_3 = 0\big|_{0,L_2}; U_3 = 0\big|_{0,L_3}\right\} \quad \text{for } r, s = (1,2). \tag{18}$$

To find the homogenized coefficients, the eighth of the RVE takes into account each single constituent individually by subdividing the RVE into smaller parts. The loading cases were treated separately and applied on the unit cell as follows:

- A displacement condition was used in the case of normal load because the strain remains almost constant in this case.
- The stresses being quasiuniform with shear loading, they were applied to find the lower limit values of the shear components for the effective elastic stiffness. Then, a weighting approach between the stress applied and the rule of mixture was used to find the average values of the upper and lower limits of these coefficients.

Description of the displacement field loading condition. First we treated the case of displacement field $\vec{U}$ affine per part and continuous in normal loading situations in the space $W_0(M)$ and we got the values of K^*_{ijkl} where $i = j$. The associated deformation field is constant per part.

The problem in $\vec{U}_1$ was resolved by minimizing the relation (15) over $W_0(M)$. For the case of $r, s = (1, 1)$ the problem in $\vec{U}_1$ was written as follows:

$$\sum_{i=1}^{8} \int_i \{(K_{11}\epsilon_{11} + K_{12}\epsilon_{22} + K_{13}\epsilon_{33})\epsilon^*_{11} + (K_{12}\epsilon_{11} + K_{22}\epsilon_{22} + K_{23}\epsilon_{33})\epsilon^*_{22} + (K_{13}\epsilon_{11} + K_{23}\epsilon_{22} + K_{33}\epsilon_{33})\epsilon^*_{33} + (K_{11}\epsilon^*_{11} + K_{12}\epsilon^*_{22} + K_{13}\epsilon^*_{33})\, dV_i\} = 0, \quad \forall \epsilon^*_{11}, \epsilon^*_{22}, \epsilon^*_{33} \in W_0(M). \tag{19}$$

Replacing K by the characteristics of the tissues existing in each portion and by isolating the terms associated with ϵ^*_{11}, ϵ^*_{22}, and ϵ^*_{33}, we found a system of three equations as a function of the strain supposed constant per part.

The homogenized coefficients K^*_{11}, K^*_{21}, and K^*_{31}, were calculated from the relation (14) for $r, s = (1, 1)$ as follows:

$$K^*_{11} = \frac{1}{\text{vol}(M)} \int_M [K_{11} + K_{11}\epsilon_{11} + K_{12}\epsilon_{22} + K_{13}\epsilon_{33}]\, dM, \tag{20}$$

$$K^*_{21} = \frac{1}{\text{vol}(M)} \int_M [K_{21} + K_{21}\epsilon_{11} + K_{22}\epsilon_{22} + K_{23}\epsilon_{33}]\, dM, \tag{21}$$

$$K^*_{31} = \frac{1}{\text{vol}(M)} \int_M [K_{31} + K_{31}\epsilon_{11} + K_{32}\epsilon_{22} + K_{33}\epsilon_{33}]\, dM. \tag{22}$$

By a summation over all the subdivided parts of the RVE, we obtained the values of K^*_{11}, K^*_{21}, and K^*_{31}. The same procedure was repeated for the cases of $r, s = (2, 2)$ and $r, s = (3, 3)$ to evaluate the values of K^*_{22}, K^*_{12}, K^*_{32}, K^*_{33}, K^*_{13}, and K^*_{23}.

Description of the stress field loading condition. To find the lower limits of the shear coefficients, we used the duality on the displacement spaces. The dual stress formulation is as follows.

Find $\bar{\sigma} \in W^*(M)$, by minimizing the form

$$\frac{1}{2} \int_M \text{Tr}[\bar{\sigma}\, K^{-1} \bar{\sigma}]\, dM + \int_M \text{Tr}[\epsilon(U_0)\bar{\sigma}]\, dM, \tag{23}$$

where $W^*(M)$ are the spaces for statically admissible stress fields.

The spaces $W_i(M)$, $i = 1, 2, 3$, become:

$$W^*_1(M) = \left\{\sigma / \sigma_{12} = \sigma_{13} = 0\big|_{0,L_1}; \sigma_{22} = 0\big|_{0,L_2}; \sigma_{33} = 0\big|_{0,L_3}\right\}, \tag{24}$$

$$W^*_2(M) = \left\{\sigma / \sigma_{11} = 0\big|_{0,L_1}; \sigma_{21} = \sigma_{23} = 0\big|_{0,L_2}; \sigma_{33} = 0\big|_{0,L_3}\right\}, \tag{25}$$

$$W^*_3(M) = \left\{\sigma / \sigma_{11} = 0\big|_{0,L_1}; \sigma_{22} = 0\big|_{0,L_2}; \sigma_{31} = \sigma_{32} = 0\big|_{0,L_3}\right\}. \tag{26}$$

The stress field is statically admissible and is assumed to be constant by part and continuous on the interfaces between parts.

For the case of $r, s = (2, 3)$:

$$W^*_1(M) = \left\{\frac{\sigma}{\sigma_{12}} = \sigma_{13} = 0\big|_{0,L_1}; \sigma_{22} = 0\big|_{0,L_2}; \sigma_{33} = 0\big|_{0,L_3}\right\}.$$

Thus, we have only σ_{11} continuous in direction 1 σ_{23} continuous in directions 2 and 3.

The dual formulation is expressed as follows:

$$\sum_{i=1}^{8}\left\{\int_i \mathrm{Tr}[\sigma K^{-1}\sigma^*]\,dM_i + \int_i \mathrm{Tr}[\epsilon(\vec{U}_0)\sigma^*]\,dM_i\right\} = 0, \quad \forall\,\sigma^* \in W_1^*, \tag{27}$$

which is equivalent in this case to:

$$\int_M (\sigma K^{-1}\sigma^* - \sigma_{23})\,dM = 0. \tag{28}$$

It is possible to solve the problem analytically and when partitioning the RVE into 64 subdivided elements (8×8) we obtained for the fairly simple case of K_{44}^*:

$$K_{44}^* = 2G_{23}^* = \frac{1}{\frac{3}{8}K_{44\mathrm{BSIR}}^{-1} + \frac{1}{14.4}K_{44\mathrm{BV}}^{-1} + \frac{1}{2.9}K_{44\mathrm{bl}}^{-1} + \frac{1}{4.7}K_{44\mathrm{SS}}^{-1}}. \tag{29}$$

G^* is the homogenized shear coefficient. The K variables are the rigidities for the BSIR, BV, blood, and SSS respectively. The same procedure can be used to determine the other effective stiffness coefficients, and K_{55}^* and K_{66}^* can be obtained fairly easily. Solving the system of equations is more complex for the other coefficients but workable. An overview of the methodology is given in the Appendix to obtain the whole matrix of effective stiffness coefficients.

4. Results and discussion

4.1. ***Numerical results of the homogenization.*** The described methodology enabled us to obtain the values of the homogenized properties of the periodic structure for the orthotropic RVE. Different cases were studied as a function of, firstly, the variability of the Young's modulus and Poisson's ratio for the SSS and, secondly, the parametric study of the variable blood response enclosed within the RVE. The material characteristics of the BVs and dura matter were kept constant using the values presented above. The four studied cases are presented in Table 3. In this table, we used the word "stiffness" corresponding to the Young's modulus in the case of the SSS material properties. However, in the case of blood, we understand stiffness as the equivalent stiffness measured by Willinger and César [1990; 1995; 1999] as mentioned above. The resulting homogenized stiffness coefficients of the RVE are presented in Table 4 and the elastic moduli and Poisson's ratios, obtained using the minimum and maximum values for the SSS and blood, are illustrated in Table 5.

Tissue	Case 1		Case 2		Case 3		Case 4	
	E	ν	E	ν	E	ν	E	ν
SSS	31.5	0.45	31.5	0.45	60	0.45	60	0.45
	K	ν	K	ν	K	ν	K	ν
Blood	1	0.49	0.012	0.49	1	0.49	0.012	0.49

Table 3. Range of values tested for the SSS and blood. Young's moduli, E, and equivalent stiffness, K, values are in MPa and Poisson's ratios, ν, are nondimensional.

When the macroscopic model is used, the local anisotropic properties of the SSS-BV junction are calculated and evaluation of a potential rupture strain of the BV is made. The advantage of using this approach is twofold: the macro-micro effect enables us to obtain the local constituents' behavior in a 3D macroscopic analysis and the micro/macro effect enables us to evaluate the influence of variability of the local phenomena for each local constituent on the 3D global behavior.

It can be noticed that the studied RVE is highly anisotropic. The anisotropy governing the tensile behavior of our structure is deduced from the large differences existing between the material properties. This is true for the Young's and shear moduli, but the Poisson's ratios are closer to each other. Since the definition of the RVE was derived using one-eighth symmetry (that is, it assumes periodic distributions in all three directions of space), it is not possible to assess the influence of the loading direction in a general loading case. But in the current study, this symmetry is not relevant for the calculation of the effective properties of the RVE since the loading direction is exclusively in the direction of the SSS main axis and using one-eighth symmetry enables us to use known boundary conditions. However, a uniaxial periodicity would definitely change the effective material response in a more random situation.

We believe that the herein obtained results for a uniaxial periodicity should be of the same order of magnitude (as a function of the parameters' variability) under other loading symmetries. However, it is necessary to develop a numerical model in order to accurately evaluate this influence.

$$\text{Case 1} \begin{pmatrix} 5.9 & 4.66 & 4.75 & 0 & 0 & 0 \\ 4.66 & 12.85 & 7.8 & 0 & 0 & 0 \\ 4.75 & 7.8 & 12.3 & 0 & 0 & 0 \\ 0 & 0 & 0 & 2.52 & 0 & 0 \\ 0 & 0 & 0 & 0 & 2.26 & 0 \\ 0 & 0 & 0 & 0 & 0 & 1.26 \end{pmatrix} \quad \text{Case 2} \begin{pmatrix} 2.56 & 1.46 & 1.38 & 0 & 0 & 0 \\ 1.46 & 9.15 & 3.9 & 0 & 0 & 0 \\ 1.38 & 3.9 & 7.6 & 0 & 0 & 0 \\ 0 & 0 & 0 & 2.96 & 0 & 0 \\ 0 & 0 & 0 & 0 & 2.12 & 0 \\ 0 & 0 & 0 & 0 & 0 & 1.18 \end{pmatrix}$$

$$\text{Case 3} \begin{pmatrix} 6.1 & 4.8 & 4.9 & 0 & 0 & 0 \\ 4.8 & 20.3 & 10.7 & 0 & 0 & 0 \\ 4.9 & 10.7 & 18.5 & 0 & 0 & 0 \\ 0 & 0 & 0 & 4.6 & 0 & 0 \\ 0 & 0 & 0 & 0 & 4.14 & 0 \\ 0 & 0 & 0 & 0 & 0 & 2.30 \end{pmatrix} \quad \text{Case 4} \begin{pmatrix} 2.6 & 1.48 & 1.4 & 0 & 0 & 0 \\ 1.48 & 16.4 & 6.5 & 0 & 0 & 0 \\ 1.4 & 6.5 & 13.4 & 0 & 0 & 0 \\ 0 & 0 & 0 & 4.52 & 0 & 0 \\ 0 & 0 & 0 & 0 & 4.06 & 0 \\ 0 & 0 & 0 & 0 & 0 & 2.26 \end{pmatrix}$$

Table 4. The homogenized stiffness coefficients, in units of MPa.

	Hom. elastic and shear moduli (MPa)						Hom. Poisson's ratios		
Case	E_1	E_2	E_3	G_{12}	G_{23}	G_{13}	ν_{12}	ν_{23}	ν_{13}
1	1.66	7.2	6.7	1.26	1.13	0.63	0.2	0.2	0.25
2	1.54	6.9	5.7	1.48	1.06	0.59	0.1	0.1	0.13
3	1.48	13.3	11.7	2.3	2.07	1.15	0.14	0.14	0.18
4	1.55	13	10.5	2.26	2.03	1.13	0.06	0.06	0.07

Table 5. The homogenized elastic moduli and Poisson's ratios.

To the best of our knowledge, there is currently no experimental work available in the literature done on the brain-skull interface region in order to describe its mechanical behavior as a function of the local constituents. In addition, the finite element models of the human head from [Ruan et al. 1993; Zhou et al. 1995; Willinger et al. 1999; Kleiven 2002; Baumgartner and Willinger 2005] all consider the brain-skull interface elements to have isotropic behavior. Therefore, no anisotropic numerical results exist to compare with the current study. In addition, brain injury and head response to impact such as in [Gong et al. 2008; Paka et al. 2011] are always developed on macroscopic models although the behaviors of the different constituents are taken into account. It is therefore clear that intracranial stresses and strains for which safety devices are developed cannot be determined from the influence of these local constituents using these models. However, the methodology used for this analysis is now well established and is based on experimental data available in the literature. A clear anisotropic material behavior is obtained. It can easily be integrated within a 3D macroscopic model (such as a finite element model) in order to study the macroscopic behavior of the brain-skull interface as a function of each local constituent. The influence of the stiffness variations E_s and K_{bl} is presented in the next section.

4.2. *Influence of external parameter variability.*

Influence of the variation of the superior sagittal sinus Young's modulus E_s. As shown in Figure 3, the variation of E_s leads to nearly linear variations of the homogenized elastic and shear moduli and Poisson's ratio for Case 1. In Figure 3a it can be noticed that the value of the homogenized E_1 remained almost constant and remarkably lower than the values of E_2 and E_3 which increased linearly as functions of E_s. This behavior is justified by the fact that direction 2 represents the axis of the sinus in the sagittal direction and direction 3 is perpendicular to the SSS and the BV, while direction 1 is that of the BV axis, which is the weakest, and not much affected by the variation of the SSS mechanical properties. On the contrary, the values of the Poisson's ratios (Figure 3b) decreased with the increase of E_s. The effect of increasing the Young's modulus by a factor of two showed a Poisson's ratio decreasing by a factor of two.

The small results variations shown between the different directions depend on the experimental data used from the literature. On the other hand, the shear moduli increase remarkably as shown in Figure 3c. The observed differences between the different shear moduli are similar to those observed for the Young's moduli. The increase in the SSS stiffness improved the shear resistance of the studied structure in the three planes, which means that the SSS properties control the shear behavior.

Influence of the variation of the blood equivalent stiffness K_{bl}. The variation of the blood equivalent stiffness K_{bl} also showed a nearly linear variation in all cases as shown in Figure 4 for the homogenized elastic properties (for Case 1). In general, the homogenized properties did not experience remarkable change with the change of K_{bl}. However the evolution of the RVE Young's moduli follows the same trend as for the variation of (E_S). In the same manner, the value of E_1 remains small compared to E_2 and E_3. On the contrary to the results found with E_S, the shear moduli are not much affected by the increase of K_{bl}. However, as opposed to the SSS Young's modulus variation, the Poisson's ratios increase with the increase of K_{bl} which means that the structure will suffer more Poisson's effect with increasing K_{bl}.

Regarding the variation of the blood mechanical properties, we can say that it has a limited influence on the overall RVE homogenized mechanical response. This result shows that the influence of the SSS and BVs' walls' stiffness has only a small influence on the mechanical evaluation of the enclosed blood

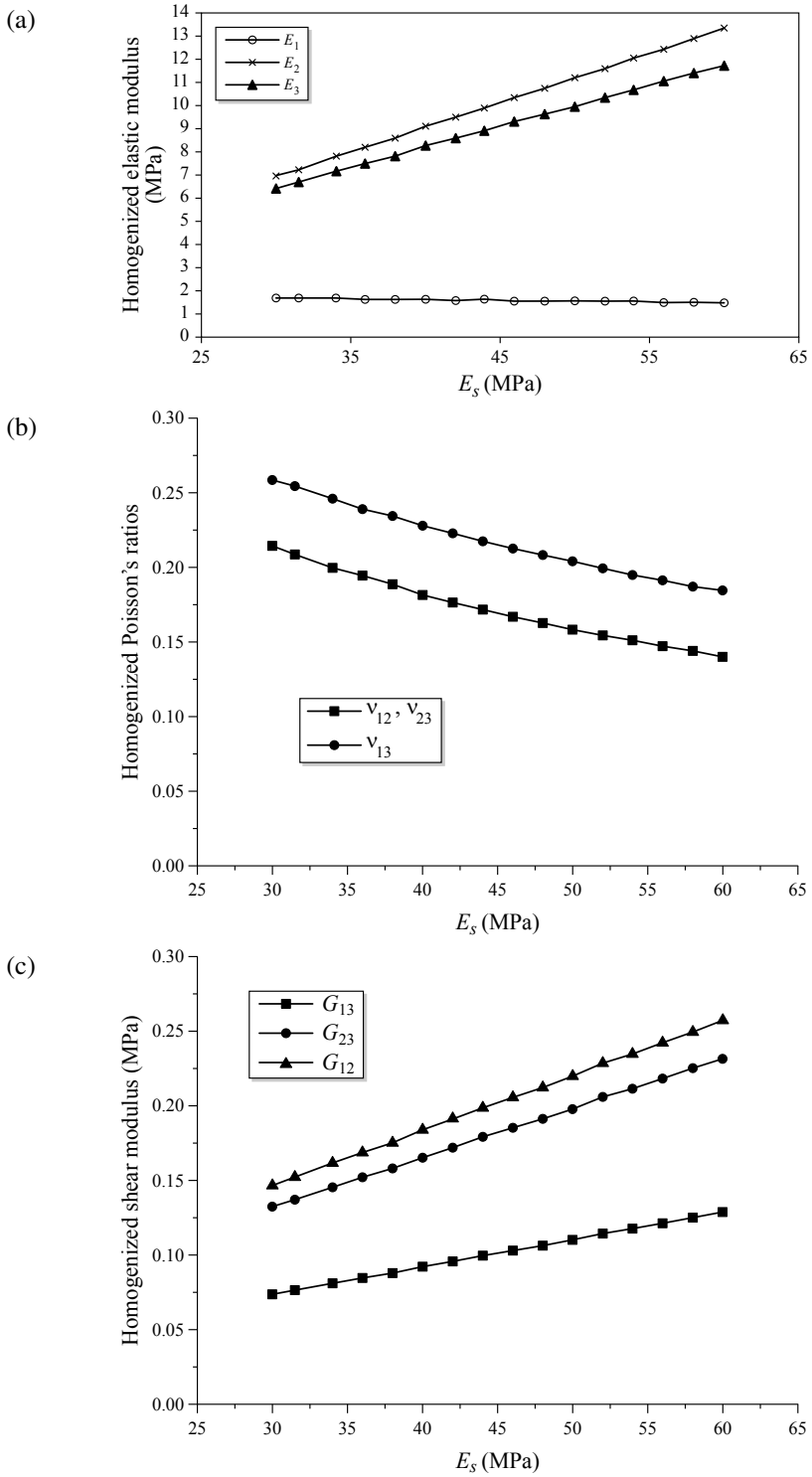

Figure 3. Variation of elastic properties of the RVE as a function of E_s. (a) Elastic modulus. (b) Poisson's ratio. (c) Shear modulus.

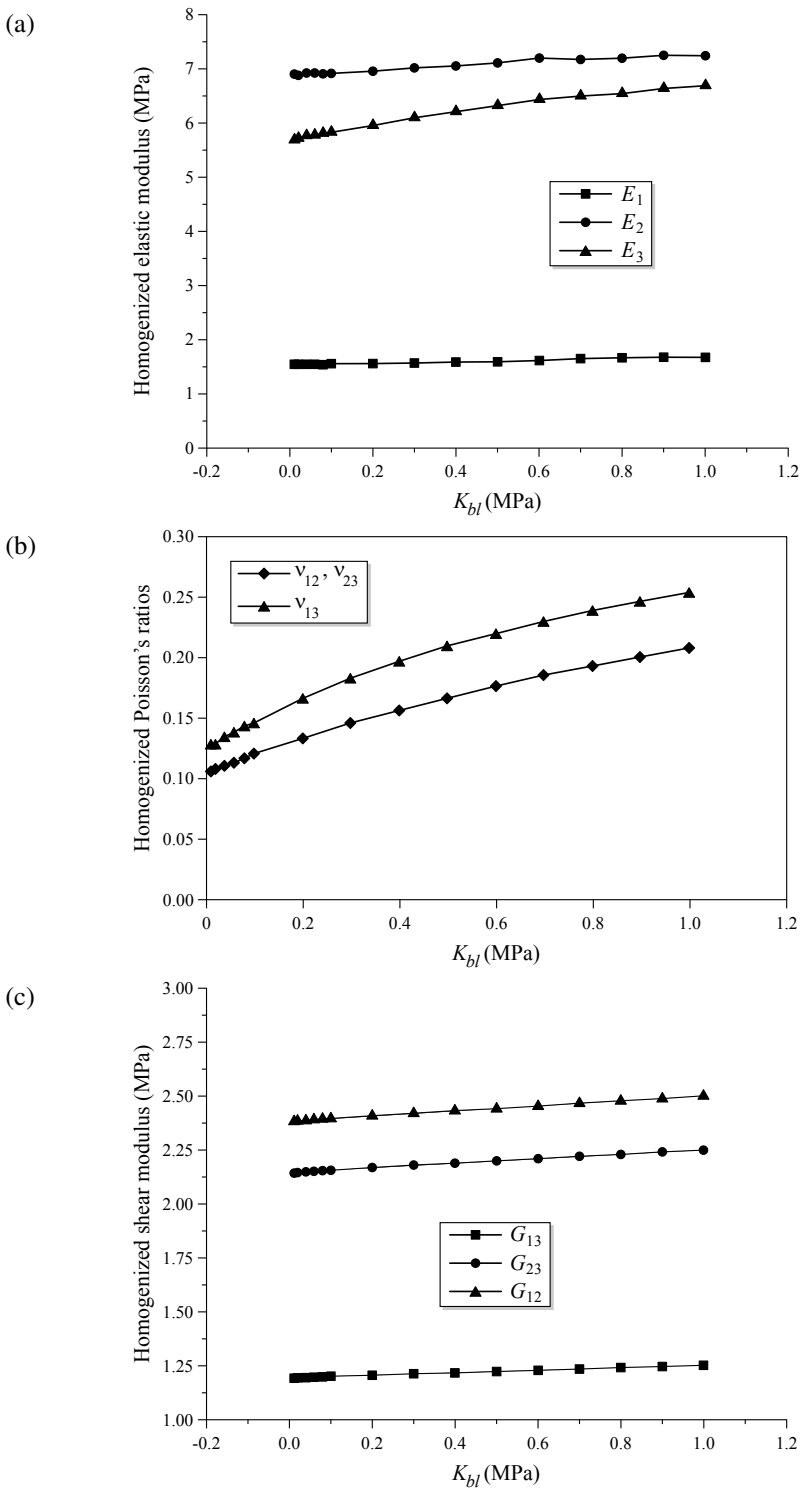

Figure 4. Variation of elastic properties with (K_{bl}). (a) Elastic modulus. (b) Poisson's ratio. (c) Shear modulus.

mechanical response. The homogenized RVE response will not be much influenced by the blood properties but instead mainly by the constituents' mechanical behavior. In addition, note that all mechanical characteristics are currently linear elastic. It is expected that using a more complex material response (nonlinear) may have an impact on the homogenized RVE properties as well as on the overall mechanical response.

5. Conclusion

The distribution of bridging veins (BVs) being almost periodic along the superior sagittal sinus (SSS) in the sagittal plane, we used the homogenization technique based on asymptotic expansion at the mesoscale. This enabled us to calculate the effective anisotropic elastic properties of the brain-skull interface region. The considered representative volume element (RVE) contains the sinus, the BVs, the blood, and the surrounding brain-skull interface region and tissues. The homogenized stiffness tensor was calculated and showed a high degree of anisotropy. In addition, the effect of the variation of the tissues' mechanical properties was also studied. The variation of the SSS elastic modulus had an important impact on the effective properties whereas the variability of the blood properties showed a limited effect. This investigation showed its interest in the predictability of the local mechanical response of the brain-skull interface region and the SSS-BV compound in particular when using modern computerized methods. The obtained results for the RVE properties can be implemented in a macroscopic model such as a FEM to study head injury problems.

Appendix

Here, we give the expressions of the calculated effective rigidity coefficients for the considered RVE as a function of the local constituents' properties. We recall that the case was presented earlier for the evaluation of the coefficient K^*_{44} in (29) using $r, s = (2, 3)$ and (24).

For solving the coefficients K^*_{55} and K^*_{66}, we used the same methodology as previously described and obtained the corresponding coefficients as:

(1) For $r, s = (1, 3)$ and (25):

$$W_2^*(M) = \left\{\sigma/\sigma_{11} = 0\big|_{0,L_1}; \sigma_{21} = \sigma_{23} = 0\big|_{0,L_2}; \sigma_{33} = 0\big|_{0,L_3}\right\},$$

we get:

$$K^*_{55} = 2G^*_{13} = \frac{1}{\frac{3}{8}K^{-1}_{55\text{BSIR}} + \frac{1}{14.4}K^{-1}_{55\text{BV}} + \frac{1}{2.9}K^{-1}_{55\text{bl}} + \frac{1}{4.7}K^{-1}_{55\text{SS}}}. \tag{A.1}$$

(2) For $r, s = (1, 2)$ and (26):

$$W_3^*(M) = \left\{\sigma/\sigma_{11} = 0\big|_{0,L_1}; \sigma_{22} = 0\big|_{0,L_2}; \sigma_{31} = \sigma_{32} = 0\big|_{0,L_3}\right\},$$

we get:

$$K^*_{66} = 2G^*_{12} = \frac{1}{\frac{3}{8}K^{-1}_{66\text{BSIR}} + \frac{1}{14.4}K^{-1}_{66\text{BV}} + \frac{1}{2.9}K^{-1}_{66\text{bl}} + \frac{1}{4.7}K^{-1}_{66\text{SS}}}. \tag{A.2}$$

We note the equations are identical $K^*_{44} = K^*_{55} = K^*_{66}$ but anisotropic behavior comes from the different material characteristics in the different directions.

In the cases of K^*_{11}, K^*_{12}, K^*_{13}, K^*_{22}, K^*_{23}, and K^*_{33}, the problem is more difficult to solve. We are presenting here the general methodology used in the case of $r, s = (1, 1)$ presented in (19) and obtaining the other coefficients follows the same resolution process. We recall that the RVE is subdivided into 64 subportions taking into account the 3D symmetries and each part of the different materials studied and present within the RVE. When replacing the mechanical characteristics of each constituent in (19) and isolating the terms associated with each ϵ^*_{11}, ϵ^*_{22}, and ϵ^*_{33} we obtained a set of three equations given by

$$\begin{aligned}
&\left(\tfrac{3}{8}K_{11\mathrm{BSIR}} + \tfrac{1}{14.4}K_{11\mathrm{BV}} + \tfrac{1}{2.9}K_{11\mathrm{bl}} + \tfrac{1}{4.7}K_{11\mathrm{SS}}\right)a \\
&\quad + \left(-\tfrac{1}{8}K_{12\mathrm{BSIR}} + \tfrac{1}{14.4}K_{12\mathrm{BV}} + \tfrac{1}{21.6}K_{12\mathrm{bl}} + \tfrac{1}{108}K_{12\mathrm{SS}}\right)b \\
&\quad + \left(\tfrac{1}{8}K_{13\mathrm{BSIR}} - \tfrac{1}{14.4}K_{13\mathrm{BV}} + \tfrac{1}{10.8}K_{13\mathrm{bl}} - \tfrac{1}{6.75}K_{13\mathrm{SS}}\right)c \\
&\quad + \left(-\tfrac{3}{8}K_{11\mathrm{BSIR}} - \tfrac{1}{14.4}K_{11\mathrm{BV}} + \tfrac{1}{4.32}K_{11\mathrm{bl}} + \tfrac{1}{4.7}K_{11\mathrm{SS}}\right) = 0, \quad \text{(A.3)}
\end{aligned}$$

$$\begin{aligned}
&\left(-\tfrac{1}{8}K_{12\mathrm{BSIR}} + \tfrac{1}{14.4}K_{12\mathrm{BV}} + \tfrac{1}{21.6}K_{12\mathrm{bl}} + \tfrac{1}{108}K_{12\mathrm{SS}}\right)a \\
&\quad + \left(\tfrac{3}{8}K_{22\mathrm{BSIR}} + \tfrac{1}{14.4}K_{22\mathrm{BV}} + \tfrac{1}{2.9}K_{22\mathrm{bl}} + \tfrac{1}{4.7}K_{22\mathrm{SS}}\right)b \\
&\quad + \left(\tfrac{1}{8}K_{23\mathrm{BSIR}} - \tfrac{1}{14.4}K_{23\mathrm{BV}} - \tfrac{1}{15.4}K_{23\mathrm{bl}} + \tfrac{1}{108}K_{23\mathrm{SS}}\right)c \\
&\quad + \left(\tfrac{1}{8}K_{12\mathrm{BSIR}} - \tfrac{1}{14.4}K_{12\mathrm{BV}} - \tfrac{1}{15.4}K_{12\mathrm{bl}} + \tfrac{1}{108}K_{12\mathrm{SS}}\right) = 0, \quad \text{(A.4)}
\end{aligned}$$

$$\begin{aligned}
&\left(\tfrac{1}{8}K_{13\mathrm{BSIR}} - \tfrac{1}{14.4}K_{13\mathrm{BV}} + \tfrac{1}{10.8}K_{13\mathrm{bl}} - \tfrac{1}{6.75}K_{13\mathrm{SS}}\right)a \\
&\quad + \left(\tfrac{1}{8}K_{23\mathrm{BSIR}} - \tfrac{1}{14.4}K_{23\mathrm{BV}} - \tfrac{1}{15.4}K_{23\mathrm{bl}} + \tfrac{1}{108}K_{23\mathrm{SS}}\right)b \\
&\quad + \left(\tfrac{3}{8}K_{33\mathrm{BSIR}} + \tfrac{1}{14.4}K_{33\mathrm{BV}} + \tfrac{1}{2.9}K_{33\mathrm{bl}} + \tfrac{1}{4.7}K_{33\mathrm{SS}}\right)c \\
&\quad + \left(-\tfrac{1}{8}K_{13\mathrm{BSIR}} + \tfrac{1}{14.4}K_{13\mathrm{BV}} + \tfrac{1}{4.9}K_{13\mathrm{bl}} - \tfrac{1}{6.75}K_{13\mathrm{SS}}\right) = 0, \quad \text{(A.5)}
\end{aligned}$$

where the subscripts BSIR, BV, bl, and SSS indicate the cerebrospinal fluid, bridging vein, blood, and superior sagittal sinus, respectively. The parameters a, b, and c are the given boundary conditions at the RVE's symmetries and each materials' subportions. They take the values ϵ_1, ϵ_2, and ϵ_3 depending on each subportion boundary condition of the RVE and the axis directions. The constants a, b, and c are evaluated when solving the system of three equations above as a function of the material parameters, and the effective stiffness coefficients can be obtained from (20), (21), and (22) so that

$$\begin{aligned}
K^*_{11} = &\left(-\tfrac{3}{8}K_{11\mathrm{BSIR}} - \tfrac{1}{14.4}K_{11\mathrm{BV}} + \tfrac{1}{4.32}K_{11\mathrm{bl}} + \tfrac{1}{4.7}K_{11\mathrm{SS}}\right)a \\
&+ \left(\tfrac{1}{8}K_{12\mathrm{BSIR}} - \tfrac{1}{14.4}K_{12\mathrm{BV}} - \tfrac{1}{15.4}K_{12\mathrm{bl}} + \tfrac{1}{108}K_{12\mathrm{SS}}\right)b \\
&+ \left(-\tfrac{1}{8}K_{13\mathrm{BSIR}} + \tfrac{1}{14.4}K_{13\mathrm{BV}} + \tfrac{1}{4.9}K_{13\mathrm{bl}} - \tfrac{1}{6.75}K_{13\mathrm{SS}}\right)c \\
&+ \left(\tfrac{3}{8}K_{11\mathrm{BSIR}} + \tfrac{1}{14.4}K_{11\mathrm{BV}} + \tfrac{1}{2.9}K_{11\mathrm{bl}} + \tfrac{1}{4.7}K_{11\mathrm{SS}}\right), \quad \text{(A.6)}
\end{aligned}$$

$$K_{21}^{*} = \left(-\tfrac{3}{8}K_{12\mathrm{BSIR}} - \tfrac{1}{14.4}K_{12\mathrm{BV}} + \tfrac{1}{4.32}K_{12\mathrm{bl}} + \tfrac{1}{4.7}K_{12\mathrm{SS}}\right)a + \left(\tfrac{1}{8}K_{22\mathrm{BSIR}} - \tfrac{1}{14.4}K_{22\mathrm{BV}} - \tfrac{1}{15.4}K_{22\mathrm{bl}} + \tfrac{1}{108}K_{22\mathrm{SS}}\right)b + \left(-\tfrac{1}{8}K_{23\mathrm{BSIR}} + \tfrac{1}{14.4}K_{23\mathrm{BV}} + \tfrac{1}{4.9}K_{23\mathrm{bl}} - \tfrac{1}{6.75}K_{23\mathrm{SS}}\right)c + \left(\tfrac{3}{8}K_{12\mathrm{BSIR}} + \tfrac{1}{14.4}K_{12\mathrm{BV}} + \tfrac{1}{2.9}K_{12\mathrm{bl}} + \tfrac{1}{4.7}K_{12\mathrm{SS}}\right), \quad \text{(A.7)}$$

$$K_{31}^{*} = \left(-\tfrac{3}{8}K_{13\mathrm{BSIR}} - \tfrac{1}{14.4}K_{13\mathrm{BV}} + \tfrac{1}{4.32}K_{13\mathrm{bl}} + \tfrac{1}{4.7}K_{13\mathrm{SS}}\right)a + \left(\tfrac{1}{8}K_{23\mathrm{BSIR}} - \tfrac{1}{14.4}K_{23\mathrm{BV}} - \tfrac{1}{15.4}K_{23\mathrm{bl}} + \tfrac{1}{108}K_{23\mathrm{SS}}\right)b + \left(-\tfrac{1}{8}K_{33\mathrm{BSIR}} + \tfrac{1}{14.4}K_{33\mathrm{BV}} + \tfrac{1}{4.9}K_{33\mathrm{bl}} - \tfrac{1}{6.75}K_{33\mathrm{SS}}\right)c + \left(\tfrac{3}{8}K_{13\mathrm{BSIR}} + \tfrac{1}{14.4}K_{13\mathrm{BV}} + \tfrac{1}{2.9}K_{13\mathrm{bl}} + \tfrac{1}{4.7}K_{13\mathrm{SS}}\right). \quad \text{(A.8)}$$

In a similar way, we solve the problem for $r, s = (2, 2)$ and $r, s = (3, 3)$. The general equations are given by

$$\sum_{i=1}^{8}\int_i \{(K_{11}\epsilon_{11} + K_{12}\epsilon_{22} + K_{13}\epsilon_{33})\epsilon_{11}^{*} + (K_{21}\epsilon_{11} + K_{22}\epsilon_{22} + K_{23}\epsilon_{33})\epsilon_{22}^{*} + (K_{31}\epsilon_{11} + K_{32}\epsilon_{22} + K_{33}\epsilon_{33})\epsilon_{33}^{*} + (K_{21}\epsilon_{11}^{*} + K_{22}\epsilon_{22}^{*} + K_{23}\epsilon_{33}^{*})\,dV_i\} = 0, \quad \forall\, \epsilon_{11}^{*}, \epsilon_{22}^{*}, \epsilon_{33}^{*} \in W_0(M), \quad \text{(A.9)}$$

$$\sum_{i=1}^{8}\int_i \{(K_{11}\epsilon_{11} + K_{12}\epsilon_{22} + K_{13}\epsilon_{33})\epsilon_{11}^{*} + (K_{21}\epsilon_{11} + K_{22}\epsilon_{22} + K_{23}\epsilon_{33})\epsilon_{22}^{*} + (K_{31}\epsilon_{11} + K_{32}\epsilon_{22} + K_{33}\epsilon_{33})\epsilon_{33}^{*} + (K_{31}\epsilon_{11}^{*} + K_{32}\epsilon_{22}^{*} + K_{33}\epsilon_{33}^{*})\,dV_i\} = 0, \quad \forall\, \epsilon_{11}^{*}, \epsilon_{22}^{*}, \epsilon_{33}^{*} \in W_0(M), \quad \text{(A.10)}$$

and we find the resulting equations with the relations $K_{11}^{*} = K_{22}^{*} = K_{33}^{*}$ and $K_{12}^{*} = K_{13}^{*} = K_{23}^{*}$. The anisotropic behavior is again given by the different material characteristics in different directions.

Lastly, the effective stiffness matrix is given for an orthotropic material with

$$K_{ijkl}^{*} = \begin{pmatrix} K_{11}^{*} & K_{12}^{*} & K_{13}^{*} & 0 & 0 & 0 \\ K_{12}^{*} & K_{22}^{*} & K_{23}^{*} & 0 & 0 & 0 \\ K_{13}^{*} & K_{23}^{*} & K_{33}^{*} & 0 & 0 & 0 \\ 0 & 0 & 0 & K_{44}^{*} & 0 & 0 \\ 0 & 0 & 0 & 0 & K_{55}^{*} & 0 \\ 0 & 0 & 0 & 0 & 0 & K_{66}^{*} \end{pmatrix}. \quad \text{(A.11)}$$

After calculating the effective stiffness coefficients using the local material characteristics and the matrix (A.11), we can obtain the results presented in Table 4.

References

[Bashkatov et al. 2003] A. N. Bashkatov, E. A. Genina, Y. P. Sinichkin, V. I. Kochubey, N. A. Lakodina, and V. V. Tuchin, "Glucose and mannitol diffusion in human dura mater", *Biophys. J.* **85** (2003), 3310–3318.

[Baumgartner and Willinger 2005] D. Baumgartner and R. Willinger, "Human head tolerance limits to specific injury mechanisms inferred from real world accident numerical reconstruction", *Rev. Eur. Élém. Finis* **14**:4-5 (2005), 421–444.

[Bayly et al. 2005] P. V. Bayly, T. S. Cohen, E. P. Leister, D. Ajo, E. C. Leuthardt, and G. M. Genin, "Deformation of the human brain induced by mild acceleration", *J. Neurotrauma* **22**:8 (2005), 845–856.

[Bertaud et al. 2010] J. Bertaud, Z. Qin, and M. J. Buehler, "Intermediate filament-deficient cells are mechanically softer at large deformation: a multiscale simulation study", *Acta Biomater.* **6** (2010), 2457–2466.

[Bloomfield et al. 1998] I. G. Bloomfield, I. H. Johnston, and L. E. Bilston, "Effects of proteins, blood cells and glucose on the viscosity of cerebrospinal fluid", *Pediatr. Neurosurg.* **28**:5 (1998), 246–251.

[Chatziprodromou et al. 2007] I. Chatziprodromou, A. Tricoli, D. Poulikakos, and Y. Ventikos, "Haemodynamics and wall remodeling of a growing cerebral aneurysm : a computational model", *J. Biomech.* **40**:2 (2007), 412–426.

[Delye et al. 2006] H. Delye, J. Goffin, P. Verschueren, J. V. Sloten, G. Van Der Perre, H. Alaerts, I. Verpoest, and D. Berckmans, "Biomechanical properties of the superior sagittal sinus-bridging vein complex", *Stapp Car Crash J.* **50** (2006), 625–636.

[Devries et al. 1989] F. Devries, H. Dumontet, G. Duvaut, and F. Léné, "Homogenization and damage for composite structures", *Int. J. Numer. Methods Eng.* **27**:2 (1989), 285–298.

[Dumont et al. 1987] J. P. Dumont, P. Ladeveze, M. Poss, and Y. Rémond, "Damage mechanics for 3-D composites", *Compos. Struct.* **8**:2 (1987), 119–141.

[Fenderson et al. 2007] B. A. Fenderson, R. Rubin, and E. Rubin, *Linppincott's review of pathology: illustrated interactive Q & A*, Lippincott Williams and Wilkins, Philadelphia, 2007.

[Gong et al. 2008] S. W. Gong, H. P. LEE, and C. Lu, "Computational simulation of the human head response to non-contact impact", *Comput. Struct.* **86** (2008), 758–770.

[Henrikson et al. 1997] R. C. Henrikson, G. I. Kaye, and J. E. Mazurkiewicz, *Histology*, National Medical Series for Independent Study, Lippincott Williams and Wilkins, Baltimore, 1997.

[Ho and Kleiven 2007] J. Ho and S. Kleiven, "Dynamic response of the brain with vasculature: a three-dimensional computational study", *J. Biomech.* **40**:13 (2007), 3006–3012.

[Horgan 2005] T. J. Horgan, *A finite element model of the human head for use in the study of pedestrian accident*, PhD thesis, National University of Ireland, Dublin, 2005.

[Huang et al. 1999] Y. Huang, M. C. Lee, W. T. Chiu, C. T. Chen, and S. Y. Lee, "Three-dimensional finite element analysis of subdural hematoma", *J. Trauma* **47** (1999), 538–544.

[Ji and Margulies 2007] S. Ji and S. S. Margulies, "In vivo pons motion within the skull", *J. Biomech.* **40** (2007), 92–99.

[Ji et al. 2004] S. Ji, Q. Zhu, L. Dougherty, and S. S. Margulies, "In vivo measurements of human brain displacement", *Stapp Car Crash J.* **48** (2004), 227–237.

[Karami et al. 2009] G. Karami, N. Grundman, N. Abolfathi, A. Naik, and M. Ziejewski, "A micromechanical hyperelastic modeling of brain white matter under large deformation", *J. Mech. Behav. Biomed. Mater.* **2** (2009), 243–254.

[Kleiven 2002] S. Kleiven, *Finite element modeling of the human head*, PhD thesis, Royal Institute of Technology, Stockholm, 2002.

[Kleiven and Hardy 2002] S. Kleiven and W. N. Hardy, "Correlation of a finite element model of human head with local brain motion: consequences for injury prediction", *Stapp Car Crash J.* **46** (2002), 123–144.

[Kumaresan and Radhakrishnan 1996] S. Kumaresan and S. Radhakrishnan, "Importance of partitioning membranes of the brain and the influence of the neck in head injury modeling", *Med. Biol. Eng. Comput.* **34**:1 (1996), 27–32.

[Ladeveze et al. 1985] P. Ladeveze, L. Proslier, and Y. Rémond, "Reconstruction of a 3-D composite behaviour from a local approach", pp. 1025–1037 in *Fifth International Conference on Composite Materials* (ICCM-V), vol. 5, edited by W. C. Harrigan et al., 1985.

[Lee and Haut 1989] M. C. Lee and R. C. Haut, "Insensitivity of tensile failure properties of human bridging veins to strain rate: implication in biomechanics of subdural hematoma", *J. Biomech.* **22**:6-7 (1989), 537–542.

[Li et al. 2007] M. X. Li, J. J. Beech-Brandt, L. R. John, P. R. Hoskins, and W. J. Easson, "Numerical analysis of pulsatile blood flow and vessel wall mechanics in different degrees of stenose", *J. Biomech.* **40**:16 (2007), 3715–3724.

[Mahmoud 2010] R. A. R. Mahmoud, *Towards the building of a local criteria of vascular lesion at the microscopical scale using homogenization*, Ph.D. thesis, Institut de Mécanique des Fluides et des Solides, Université de Strasbourg, 2010.

[Maxeiner and Wolff 2002] H. Maxeiner and M. Wolff, "Pure subdural hematomas: a postmortem analysis of their form and bleeding points", *Neurosurg.* **50**:3 (2002), 503–509.

[Melvin et al. 1970] J. W. Melvin, J. H. McElhaney, and V. L. Roberts, "Development of a mechanical model of the human head: determination of tissue properties and synthetic substitute materials", Technical report SAE Paper No. 700903, University of Michigan/Society of Automobile Engineers, 1970.

[Moghadam and Sadegh 2009] M. Z. Moghadam and A. M. Sadegh, "Global/local head models to analyze cerebral blood vessel rupture leading to ASDH and SAH", *Comput. Methods Biomech. Biomed. Engin.* **12**:1 (2009), 1–12.

[Monson et al. 2005] K. L. Monson, W. Goldsmith, N. M. Barbaro, and G. T. Manley, "Significant of source and size in the mechanical response of human cerebral blood vessels", *J. Biomech.* **38** (2005), 737–744.

[Mukherjee et al. 2006] S. Mukherjee, A. Chawla, and B. Karthikeyan, "A review of the mechanical properties of human body soft tissues in the head, neck and spine", *Inst. Eng. J.* **87** (2006), 10–24.

[Paka et al. 2011] P. Paka, G. Karami, and M. Ziejewski, "Examination of brain injury under impact with the ground of various stiffness", *Proc. Eng.* **13** (2011), 409–414.

[Park and Lakes 2007] J. B. Park and R. S. Lakes, *Biomaterials: an introduction*, 3rd ed., pp. 245–247, Springer, New York, 2007, Available at http://www.springerlink.com/content/978-0-387-37879-4.

[Pham and Sun 2010] T. Pham and W. Sun, "Characterization of the mechanical properties of the coronary sinus for percutaneous transvenous mitral annuloplasty", *Acta Biomater.* **6** (2010), 4336–4344.

[Prevost et al. 2011a] T. P. Prevost, A. Balakrishnan, S. Suresh, and S. Socrate, "Biomechanics of brain tissues", *Acta Biomater.* **7** (2011), 83–95.

[Prevost et al. 2011b] T. P. Prevost, G. Jin, M. A. de Moya, H. B. Alam, S. Suresh, and S. Socrate, "Dynamic mechanical response of brain tissue in indentation in vivo, in situ and in vitro", *Acta Biomater.* **7** (2011), 4090–4101.

[Rhoton 2002] A. L. Rhoton, Jr., "The cerebral veins", *Neurosurg.* **51**:Supplement 1 (2002), 159–205.

[Ruan and Prasad 1996] J. S. Ruan and P. Prasad, "Study of the biodynamic characteristics of the human head", pp. 63–74 in *1996 International Conference on the Biomechanics of Impacts* (Dublin, 1996), edited by D. Césari and A. Charpenne, IRCOBI, Bron, 1996.

[Ruan et al. 1991] J. S. Ruan, T. B. Khalil, and A. I. King, "Human head impact dynamic response to side impact by finite element modeling", *J. Biomech. Eng.* (*ASME*) **113** (1991), 276–283.

[Ruan et al. 1993] J. S. Ruan, T. B. Khalil, and A. I. King, "Finite element modeling of direct head impact", Technical report SAE Paper No. 933114, Wayne State University/Society of Automobile Engineers, 1993.

[Sabet et al. 2008] A. A. Sabet, E. Christoforou, B. Zatlin, G. M. Genin, and P. V. Bayly, "Deformation of the human brain induced by mild angular head acceleration", *J. Biomech.* **41** (2008), 307–315.

[Samet and Lelkes 1999] M. M. Samet and P. I. Lelkes, "The hemodynamic environment of endothelium in vivo and its simulation in vitro", pp. 8–9 in *Mechanical forces and the endothelium*, edited by P. L. Lelkes, Endothelial Cell Research Series **6**, Harwood, Amsterdam, 1999.

[Sanchez-Palencia 1974] E. Sanchez-Palencia, "Comportement local et macroscopique d'un type de milieux physiques hétérogènes", *Int. J. Eng. Sci.* **12**:4 (1974), 331–351.

[Sanz-Herrera et al. 2009] J. A. Sanz-Herrera, J. M. Garcia-Aznar, and M. Doblaré, "On scaffold designing for bone regeneration: a computational multiscale approach", *Acta Biomater.* **5**:1 (2009), 219–229.

[Sarkar et al. 2004] S. Sarkar, S. Majumder, and A. Roychowdhury, "Response of human head under static and dynamic load using finite element method", *Trend. Biomater. Artif. Organ.* **17**:2 (2004), 130–134.

[Soliman et al. 2010] S. Soliman, S. Pagliari, A. Rinaldi, G. Forte, R. Fiaccavento, F. Pagliari, O. Franzese, M. Minieri, P. Di Nardo, S. Liccocia, and E. Traversa, "Multiscale three-dimensional scaffolds for soft tissue engineering via multimodal electrospinning", *Acta Biomater.* **6** (2010), 1227–1237.

[Vignes et al. 2007] J.-R. Vignes, A. Dagain, D. Liguoro, and J. Guérin, "A hypothesis of cerebral venous system regulation based on a study of the junction between the cortical bridging veins and the superior sagittal sinus", *J. Neurosurg.* **107** (2007), 1205–1210.

[Willinger and Césari 1990] R. Willinger and D. Césari, "Determination of cerebral motion at impact through mechanical impedance methods", pp. 203–214 in *1990 International Conference on the Biomechanics of Impacts* (Bron-Lyon, 1990), edited by D. Césari and A. Charpenne, IRCOBI, Bron, 1990.

[Willinger et al. 1992] R. Willinger, C. M. Kopp, and D. Césari, "New concept of contrecoup lesion mechanism: modal analysis of a finite element head model", pp. 283–297 in *1992 International Conference on the Biomechanics of Impacts* (Verona, 1992), edited by D. Césari and A. Charpenne, IRCOBI, Bron, 1992.

[Willinger et al. 1995] R. Willinger, L. Taleb, and C. M. Kopp, "Modal and temporal analysis of head mathematical models", *J. Neurotrauma* **12**:4 (1995), 743–754.

[Willinger et al. 1999] R. Willinger, H. S. Kang, and B. M. Diaw, "Three dimensional human head finite element model validation against experimental impacts", *Ann. Biomed. Eng.* **27**:3 (1999), 403–410.

[Wittek and Omori 2003] A. Wittek and K. Omori, "Parametric study of effects of brain-skull boundary conditions and brain material properties on responses of simplified finite element brain model under angular acceleration impulse in sagittal plane", *Trans. Jpn. Soc. Mech. Eng. C* **46**:4 (2003), 1388–1399.

[Yamashima and Friede 1984] T. Yamashima and R. L. Friede, "Why do bridging veins rupture in the virtual subdural space?", *J. Neurol. Neurosurg. Psychiatry* **47** (1984), 121–127.

[Yao et al. 2008] J. Yao, J. Yang, and D. Otte, "Investigation of head injuries by reconstruction of real world vehicles-versus-adult-pedestrian accidents", *Saf. Sci.* **46**:7 (2008), 1103–1114.

[Yoon et al. 2002] Y. J. Yoon, G. Yang, and S. C. Cowin, "Estimation of the effective transversely isotropic elastic constants of a material from known values of the material's orthotropic elastic constants", *Biomech. Model. Mechanobiol.* **1** (2002), 83–93.

[Yu et al. 2008] X. Yu, L. Wang, S. Sun, and L. Tong, "Viscoelastic finite element analysis of human skull-dura mater system as intracranial pressure changing", *Afr. J. Biotechnol.* **7**:6 (2008), 689–695.

[Zhou et al. 1995] C. Zhou, T. B. Khalil, and A. I. King, "A new model comparing impact responses of the homogeneous and inhomogeneous human brain", Technical Report SAE Paper No. 952714, Wayne State University/Society of Automobile Engineers, 1995.

Received 11 May 2012. Revised 25 Jul 2012. Accepted 25 Jul 2012.

RANIA ABDEL RAHMAN: rania.elanwar@gmail.com
Faculty of Engineering, The French University of Egypt, BP 21 Chorouk city, Km 37, Highway Cairo-Ismailia, Egypt

DANIEL GEORGE: george@unistra.fr
Institute of Fluids and Solid Mechanics, University of Strasbourg / CNRS, 2 rue Boussingault, 67000 Strasbourg, France

DANIEL BAUMGARTNER: daniel.baumgartner@unistra.fr
Institute of Fluids and Solid Mechanics, University of Strasbourg/CNRS, 2 rue Boussingault, 67000 Strasbourg, France

MATHIEU NIERENBERGER: mathieu.nierenberger@etu.unistra.fr
Institute of Fluids and Solid Mechanics, University of Strasbourg/CNRS, 2 rue Boussingault, 67000 Strasbourg, France

YVES RÉMOND: remond@unistra.fr
Institute of Fluids and Solid Mechanics, University of Strasbourg/CNRS, 2 rue Boussingault, 67000 Strasbourg, France

SAÏD AHZI: ahzi@unistra.fr
Institute of Fluid and Solid Mechanics UMR, University of Strasbourg/CNRS, 2 Rue Boussingault, 67000 Strasbourg, France

SUBMISSION GUIDELINES

ORIGINALITY

Authors may submit manuscripts in PDF format online at the Submissions page. Submission of a manuscript acknowledges that the manuscript is original and has neither previously, nor simultaneously, in whole or in part, been submitted elsewhere. Information regarding the preparation of manuscripts is provided below. Correspondence by email is requested for convenience and speed. For further information, write to one of the Chief Editors:

Davide Bigoni	bigoni@ing.unitn.it
Iwona Jasiuk	ijasiuk@me.concordia.ca
Yasuhide Shindo	shindo@material.tohoku.ac.jp

LANGUAGE

Manuscripts must be in English. A brief abstract of about 150 words or less must be included. The abstract should be self-contained and not make any reference to the bibliography. Also required are keywords and subject classification for the article, and, for each author, postal address, affiliation (if appropriate), and email address if available. A home-page URL is optional.

FORMAT

Authors can use their preferred manuscript-preparation software, including for example Microsoft Word or any variant of TEX. The journal itself is produced in LATEX, so accepted articles prepared using other software will be converted to LATEX at production time. Authors wishing to prepare their document in LATEX can follow the example file at www.jomms.net (but the use of other class files is acceptable). At submission time only a PDF file is required. After acceptance, authors must submit all source material (see especially Figures below).

REFERENCES

Bibliographical references should be complete, including article titles and page ranges. All references in the bibliography should be cited in the text. The use of BibTEX is preferred but not required. Tags will be converted to the house format (see a current issue for examples); however, for submission you may use the format of your choice. Links will be provided to all literature with known web locations; authors can supply their own links in addition to those provided by the editorial process.

FIGURES

Figures must be of publication quality. After acceptance, you will need to submit the original source files in vector format for all diagrams and graphs in your manuscript: vector EPS or vector PDF files are the most useful. (EPS stands for Encapsulated PostScript.)

Most drawing and graphing packages—Mathematica, Adobe Illustrator, Corel Draw, MATLAB, etc.—allow the user to save files in one of these formats. Make sure that what you're saving is vector graphics and not a bitmap. If you need help, please write to graphics@msp.org with as many details as you can about how your graphics were generated.

Please also include the original data for any plots. This is particularly important if you are unable to save Excel-generated plots in vector format. Saving them as bitmaps is not useful; please send the Excel (.xls) spreadsheets instead. Bundle your figure files into a single archive (using zip, tar, rar or other format of your choice) and upload on the link you been given at acceptance time.

Each figure should be captioned and numbered so that it can float. Small figures occupying no more than three lines of vertical space can be kept in the text ("the curve looks like this:"). It is acceptable to submit a manuscript with all figures at the end, if their placement is specified in the text by means of comments such as "Place Figure 1 here". The same considerations apply to tables.

WHITE SPACE

Forced line breaks or page breaks should not be inserted in the document. There is no point in your trying to optimize line and page breaks in the original manuscript. The manuscript will be reformatted to use the journal's preferred fonts and layout.

PROOFS

Page proofs will be made available to authors (or to the designated corresponding author) at a Web site in PDF format. Failure to acknowledge the receipt of proofs or to return corrections within the requested deadline may cause publication to be postponed.

Journal of Mechanics of Materials and Structures
Volume 7, No. 6 June 2012